LEVERAGING MICROFLUIDICS AND ELECTROKINETICS TO IMPROVE SAMPLE PREPARATION AND BIOMARKER DETECTION

A Dissertation

by

JARAD WILKER YOST

Submitted to the Graduate and Professional School of
Texas A&M University
in partial fulfillment of the requirements for the degree of

DOCTOR OF PHILOSOPHY

Chair of Committee,	Zachary Gagnon
Committee Members,	Victor Ugaz
	Abhishek Jain
	Arum Han
Head of Department,	Victor Ugaz

May 2023

Major Subject: Chemical Engineering

ABSTRACT

With the advent of global pandemics, the world has developed a demonstrable need for rapid and low-cost testing platforms for diagnostics. Microfluidic diagnostics can meet this demand due to the versatility and scalability of microfluidic devices. However, two components of microfluidic diagnostics, sample preparation and biomarker detection, require further innovation for effective use within microfluidics. In this work, improvements to microfluidic sample preparation and biomarker detection are presented. To improve microfluidic sample preparation, the leading electrolyte (LE) in free-flow isotachophoresis (FFITP) was replaced with a conductive wall, limiting system complexity and analyte-electrolyte interactions. This new system, called free-flow teíchophoresis (FFTPE), was used to concentrate protein, separate multiple proteins, and concentrate nucleic acids. To improve microfluidic biomarker detection, a novel heating method called Electrokinetic Nucleic Acid Amplification (E-NAAMP) was developed. E-NAAMP replaces traditional boundary-driven heating techniques found in microfluidic nucleic acid amplification (NAA) by applying electric current directly to the reaction. E-NAAMP was used to drive NAA using both Loop-Mediated Isothermal Amplification (LAMP) and the Polymerase Chain Reaction (PCR). Finally, improvements were made to E-NAAMP by incorporating it into a novel paper microfluidic platform called Microfluidic Pressure-in-Paper (μPiP). Paper E-NAAMP was used to amplify nucleic acids with LAMP. It was also demonstrated that paper passivation via a carrier protein is necessary for paper E-NAAMP success. With these improvements, we envision an all-in-one chip where FFTPE is used to remove NAA

inhibitors from biological samples and E-NAAMP is subsequently used to amplify these inhibitor-free nucleic acid samples.

DEDICATION

To my Mom & Dad, my siblings Gillian, Rachel, and James,

and my grandmother, Mimi.

ACKNOWLEDGEMENTS

I would first like to acknowledge and thank my advisor and mentor, Dr. Zachary Gagnon. His support and advice throughout my time at Texas A&M University was key to the success of my research. He is one of the most caring and passionate mentors I have worked for. During the early days of the COVID-19 pandemic, Dr. Gagnon advocated for me when I had to make a quick decision to continue graduate school after completing my masters, so he worked closely with the department to quickly admit me. So, thanks to Dr. Gagnon, Ashley Henley, and the rest of the graduate office for ensuring my continued education at Texas A&M University.

I would also like to thank my lab mates Steven Doria and Md Nazibul Islam for their contributions to this work. Steven and I collaborated closely on work presented in Section 3, with Steven developing much of the baseline technology (TPE). That work would not have been possible without the groundwork he did. Nazibul invented the µPiP technology seen in Section 5, so I thank him for making the research presented in that section possible. A general thanks goes to all my lab mates for their support, wisdom, and advice.

My thanks also extend to my previous scientific mentors at Colorado State University and Boston Biochem, where my passion for engineering and biotechnology grew into what it is today. I would also like to thank my oldest and closest friend, Joshua Witty, for encouraging me and listening to me vent about work and life. Additional thanks go to the friends I have made through both Chemical Engineering and Club Swimming. Coming from out-of-state, they gave me a sense of community during

graduate school. Finally, I'd like to thank my family: Gillian, Rachel, James, Mom (Wendy), Dad (Dennis, '84), and Mimi (Pamela) for their support, laughter, and advice during my time at Texas A&M University. I could not have achieved what I did without them.

CONTRIBUTORS AND FUNDING SOURCES

Contributors

This work was supervised by a dissertation committee consisting of Professor Zachary Gagnon (advisor) and Professor Victor Ugaz of the Department of Chemical Engineering, Professor Abhishek Jain of the Department of Biomedical Engineering, and Professor Arum Han of the Department of Electrical Engineering.

Teíchophoresis (TPE) was developed by my lab mate, Steven Doria, which is used extensively in Section 3. Section 3 was also done in collaboration with Steven Doria, so he and the student are co-first authors on the publication published in Section 3. Microfluidic Pressure-in-Paper (µPiP) was developed by my lab mate, Md Nazibul Islam, which is used extensively in Section 5. All other work conducted for this dissertation was completed by the student independently, with occasional input and assistance from other lab members.

Funding Sources

Graduate study was supported by a start-up account for Professor Gagnon provided by the Department of Chemical Engineering (Account #28-225357-00000), a NASA grant titled “Rapid and Simple Sample Acquisition During Space Flight: Simultaneous Extraction of Proteins and Nucleic Acids from Bodily Fluids and Cabin Water Using Free-Flow Bi-directional Isotachophoresis” (80NSSC19K140), an NSF Innovation Corp Grant titled “Microfluidic Pressure-in-Paper (µPiP)” (2112224), and the 2022 Brunner Barnes Graduate Fellowship given by the Department of Chemical Engineering.

NOMENCLATURE

µPAD	Paper Microfluidic Device
µPiP	Microfluidic Pressure-In-Paper
µTAS	Micro Total Analysis System
AC	Alternating Current
AM142	Ahlstrom-Munksjö Grade 142
B3	Backward Outer Primer
BIP	Backward Inner Primer
BP	Base Pair
BSA	Bovine Serum Albumin
CB	Carbon Black
CF	Concentration Factor
CNT	Carbon Nanotubes
CZE	Capillary Zone Electrophoresis
DAQ	Data Acquisition
DC	Direct Current
DEP	Dielectrophoresis
DNA	Deoxyribonucleic Acid
dNTP	Deoxynucleotide Triphosphate
dsDNA	Double-Stranded Deoxyribonucleic Acid
ELISA	Enzyme-Linked Immunosorbent Assay
E-NAAMP	Electrokinetic Nucleic Acid Amplification

F3	Forward Outer Primer
FDA	Food and Drug Administration
FFE	Free-Flow Electrophoresis
FF-ICPF	Free-Flow Ion Concentration Polarization Focusing
FFITP	Free-Flow Isotachophoresis
FFTPE	Free-Flow Teíchophoresis
FIP	Forward Inner Primer
FITC	Fluorescein Isothiocyanate
HDA	Helicase-Dependent Amplification
HEPES	4-(2-hydroxyethyl)-1-piperazineethanesulfonic Acid
HTC	Heat Transfer Coefficient
IDT	Integrated DNA Technologies
IR	Infrared
ITP	Isotachophoresis
LAMP	Loop-Mediated Isothermal Amplification
LE	Leading Electrolyte
LFA	Lateral Flow Assay
LOC	Lab-On-A-Chip
LoopB	Backward Loop Primer
LoopF	Forward Loop Primer
NA	Nucleic Acid
NAA	Nucleic Acid Amplification
NTC	Negative Temperature Coefficient

OVB	Ovalbumin
PAGE	Polyacrylamide Gel Electrophoresis
PBS	Phosphate-Buffered Saline
PC	Polycarbonate
PCR	Polymerase Chain Reaction
PDC	Pulsed Direct Current
PDMS	Polydimethylsiloxane
PES	Polyethersulfone
PID	Proportional-Integral-Derivative
POC	Point-Of-Care
qPCR	Quantitative Polymerase Chain Reaction
RF	Radio Frequency
RNA	Ribonucleic Acid
RPA	Recombinase Polymerase Amplification
SPE	Solid Phase Extraction
ssDNA	Single-Stranded Deoxyribonucleic Acid
TAE	Tris-Acetate-EDTA
TE	Terminating Electrolyte
Tm	Melting Temperature
TPE	Teíchophoresis
TS1	Test Sequence 1
TS2	Test Sequence 2
W1	Whatman 1

TABLE OF CONTENTS

Page

Page

Page

LIST OF FIGURES

Page

Page

LIST OF TABLES

Page

1. INTRODUCTION

Since 2019, the SARS-CoV-2 pandemic has spread across the planet, infecting and killing millions of people. This pandemic demonstrated a need for small-scale and rapid diagnostic tests, particularly nucleic acid amplification (NAA) tests which is how many diseases are diagnosed including COVID-19. While other technologies exist to detect COVID-19, including lateral flow assays (LFA's), CT-Scans, and enzyme-linked immunosorbent assays (ELISA's), NAA remains the most accurate diagnostic method for COVID-19.[1] While COVID-19 has started to subside in the public view, there always remain questions of steps to take for the next pandemic.

One technology that can assist in the development of small-scale and point-of-care diagnostics is microfluidics, or lab-on-a-chip (LOC) devices. Lab-on-a-chip technology has been around for well over twenty-five years and has multiple interworking components such as sample preparation, channel design and fabrication, and detection, as shown in Figure 1.1.[2] Each of these components works in conjunction with one another to operate as a single diagnostic device, however, the areas of sample preparation and biomarker detection can be improved.

Sample preparation is one of the largest hurdles to overcome in biological diagnostics.[3,4] Most biomarker detection technology analyzes the proteome or genome found in whole blood, serum, urine, or saliva to identify biomarkers and diseases.[5] When screening for biomarkers, various sample components such as PCR inhibitors, DNase and RNase enzymes, and proteome degradation enzymes can prevent detection.[6–8] These challenges are also present in microfluidics, with technologies used for sample

preparation at macro-scale, such as cell lysis devices, centrifuges, and nucleic acid (NA) extraction columns, not as widely available for micro-scale use. Overcoming these microfluidic sample preparation challenges is a major goal of this research.

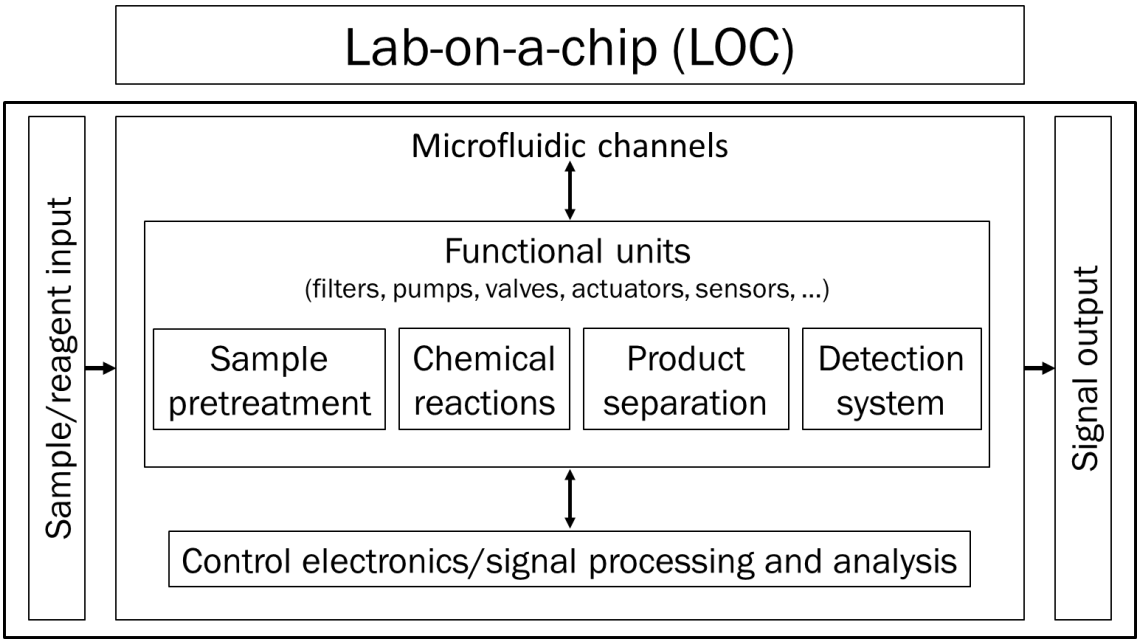

Figure 1.1 Diagram of various components of lab-on-a-chip operations.[2]*****

After the sample has been adequately prepared, biomarkers can be detected. A common detection method is NAA, such as the polymerase chain reaction (PCR) or loop-mediated isothermal amplification (LAMP). Traditionally done at lab scale using a benchtop thermal cycler, the past two decades have seen rapid miniaturization of NAA using microfluidics. While many devices are rapid and effective at amplifying nucleic acids, nearly all microfluidic NAA devices rely on boundary-driven heating, with bulky heaters attached to the device's underside. This generates an inherent thermal gradient

* – Reprinted with permission from Santos, H.; Liu, D.; Zhang, H. *Microfluidics for Pharmaceutical Applications - 1st Edition*, 1st ed.; Elsevier, 2018 Copyright 2018 Elsevier

within the amplification reaction and places constraints on device size and portability.[9] A volumetric heating method, such as the electrokinetic Joule heating, would both limit thermal gradients experienced by amplification reactions and would not require bulky heaters to be attached to microfluidic amplification devices.

There are two questions this research aims to answer. First, can sample preparation techniques be improved to where biomarker detection inhibitors can be removed? Secondly, can drawbacks of microfluidic NAA be rectified using a volumetric heating method, such as electrokinetic Joule heating? This dissertation will present the background, experiments, and results needed to sufficiently answer these questions. A detailed breakdown of this dissertation can be found in the next section, Section 1.1.

1.1. Dissertation Overview

This dissertation is broken into five subsequent sections. Section 2 discusses the background and theory behind the techniques and platforms used in this research including microfluidics, electrokinetics, teíchophoresis, Joule heating, nucleic acid amplification, and paper microfluidics.

Section 3 of this dissertation uses teíchophoresis (TPE) as a sample preparation technique to concentrate and separate biomarkers. Previous work has shown that isotachophoresis (ITP), another electrokinetic sample preparation technique that uses a two-electrolyte system – a leading electrolyte (LE) and terminating electrolyte (TE) – can be improved and simplified to a one electrolyte system by replacing the LE with a conductive wall. This leaves only the TE and the sample(s) as the only fluidic components during operation. This innovation was named teíchophoresis, with “teícho” being Greek for “wall”.[10] In this dissertation, TPE was used to both concentrate and

separate protein and used to concentrate nucleic acids by exploiting electrophoretic mobility differences. This work was published in Talanta in 2022.[11]

Section 4 of this dissertation uses Joule heating generated by high-frequency electric potential, rather than boundary-driven heating, to drive NAA for biomarker detection. Boundary-driven heating generates thermal gradients throughout an amplification reaction, so a volumetric method – Joule-heating – is used instead. This new heating method, called electrokinetic nucleic acid amplification (E-NAAMP), was used to amplify free deoxyribonucleic acid (DNA) sequences commonly found in *E. coli* by two methods: LAMP, an isothermal amplification method, and PCR, a thermal cycling method. E-NAAMP did not generate any gaseous byproducts, nor did it degrade enzyme activity during the amplification reaction. This work was published in Biomicrofluidics in 2022.[12]

Section 5 addresses E-NAAMP system drawbacks and improves upon those drawbacks by incorporating E-NAAMP into a paper microfluidic platform, Microfluidic Pressure-in-Paper (μPiP), developed in the Gagnon Lab. μPiP was developed to address shortcomings of traditional paper microfluidics by encapsulating paper channels within sheets of polydimethylsiloxane (PDMS) and using pressure to drive fluid flow. μPiP was used to successfully concentrate NAs and characterize red blood cells, demonstrating μPiP's versatility, making it a suitable platform for performing paper E-NAAMP.[13] Temperature-voltage relationships experienced by paper E-NAAMP were examined using experimental and numerical methods, with both methods showing good agreement. Additionally, paper interactions with DNA polymerase were explored, finding that passivation using bovine serum albumin (BSA) is necessary for successful

NAA using paper E-NAAMP. Finally, paper E-NAAMP was performed, showing that E-NAAMP is compatible with multiple paper types. This work was submitted to Biomicrofluidics in 2022 and is currently under revision.

Finally, in Section 6, general conclusions about this work are presented, in addition to placing this work in context of previous work. Additionally, future research using bi-directional TPE and improvements to paper-based E-NAAMP are discussed, including simultaneous separation of protein and DNA using TPE, further refinements and characterization of paper E-NAAMP, and the overall goal of using nucleic acid samples purified by paper-based bi-directional TPE within paper E-NAAMP, creating a continuous diagnostic workflow with μPiP.

2. BACKGROUND

2.1. Microfluidic Sample Preparation

Microfluidics involves scaling down traditional lab operations to the micro-scale and was first developed in the late 1990s. Since then, microfluidics has seen incredible growth in academia, as well as more recent commercial growth, with companies such as 10x Genomics and Illumina developing products that are widely used in modern research and diagnostics.[14–16] While early microfluidic devices were fabricated with PDMS using soft lithography techniques, the field has expanded to include other fabrication methods such as 3D printing, hot embossing, and machining.[17–19] These new fabrication methods are traditionally used for commercial microfluidic devices, with PDMS soft lithography still the method of choice for academia. Using these devices, many commonplace lab techniques have been scaled down and simplified, such as nucleic acid amplification, western blotting, and standard fluidic mixing.[20,21]

While many fluidic-based-on-a-chip unit operations (e.g., mixing, pumping, metering, etc.) are largely well-defined, most of these microfluidic processes are optimized for purified "clean" samples and can require bulky supporting infrastructures. Such constraints place limits on device portability and application, preventing use of microfluidics in real-world environments. The ability to prepare "dirty" samples for manipulation at the microfluidic scale would significantly improve the impact and robustness of existing lab-on-a-chip operations designed for "clean" samples. Sample purification, enrichment, and target analyte isolation are at the heart of sample preparative tasks. There are many sample preparation methods, including cell lysis,

filtration, biomolecule purification, target amplification, electrophoresis separation, and analyte centrifugation.[5,22–24] Electrokinetics can also be used in conjunction with microfluidics to prepare samples. Two primary electrokinetic techniques – electrophoresis and isotachophoresis (ITP) – utilize an electric field to drive charged particles and molecules to migrate and concentrate in well-defined positions within microfluidic architecture.[25–27]

Electrophoresis is one of the most widely used analytical techniques in molecular biology and has been incorporated extensively into microfluidics. Electrophoresis is commonly used to separate biological molecules for analysis purposes – proteins using polyacrylamide gels and nucleic acids using agarose gels. Since large nucleic acid strands and proteins migrate slower than smaller nucleic acid strands and proteins when exposed to an electric field in a gel medium, the result is a ladder of molecules separated by size.[27] The most common microfluidic electrophoresis method is capillary electrophoresis, where molecules migrate through a polymer-filled capillary tube under the influence of an electric field. The micro-scale of capillary electrophoresis has the advantage of dissipating heat more rapidly than traditional gel electrophoresis, producing shorter run times.[28,29] Since the advent of capillary electrophoresis, many labs have developed systems to improve the functionality and specificity of microfluidic electrophoresis, including the incorporation of other lab-on-a-chip scale techniques, such as lysis and nucleic acid amplification.[22,24]

For whole-cell lysates, another promising method for sample enrichment is the electrokinetic technique, isotachophoresis. ITP causes charged ions, proteins, or DNA strands to migrate through a medium under the influence of an externally applied

electric field based on their electrophoretic mobility. ITP traditionally serves to concentrate an analyte of interest between two other electrolytes – a leading electrolyte (LE) and a terminating electrolyte (TE). The LE has a greater electrophoretic mobility than the analyte, migrating faster than the analyte, while the TE has a lower electrophoretic mobility than the analyte, migrating slower than the analyte. When all three species are introduced in the system and exposed to an electric field, they migrate and stack in order of decreasing electrophoretic mobility, from which the analyte of interest can be isolated.[25,26] ITP will be further expanded upon in Section 2.2.1. Microfluidics, when used in conjunction with various electrokinetic techniques, is a powerful tool for many different applications. Some of these applications are expanded upon in the next section, Section 2.2.

2.2. Electrokinetics

Electrokinetics was defined as the study of particle movement under electric fields, but that definition has evolved to a more general definition: the study of charge movement through an external electric field. Charges can range from nanoparticles to enzymes and nucleic acids; anything that exhibits a charge. There are two types of electric fields – direct and alternating – leading to two types of electrokinetics: direct current (DC) electrokinetics and alternating current (AC) electrokinetics.[30]

DC electrokinetics is commonly used in most laboratory situations. The main use of DC electrokinetics is electrophoresis, which is the study of particles under the effect of a constant electric field. Due to the large voltages required and adverse heating effects that arise, DC electrokinetics usage in microfluidics is generally limited to electrophoresis and particle motion studies, with AC electrokinetics used in most other

microfluidic electrokinetic studies.[31,32] AC electrokinetics is the investigation of charge movement under the influence of AC electric fields and is widely used in microfluidics. While DC has a single polarity, AC's polarity alternates between positive and negative at a certain frequency. AC electrokinetics has the advantage of requiring lower voltages to conduct experiments because of the higher frequencies used, leading to fewer Faradaic byproducts. Many phenomena arise from using AC electrokinetics such as dielectrophoresis (DEP), electrokinetic flow, and electrothermal heating, or Joule heating.[33–35]

Dielectrophoresis, one of the most common applications of AC electrokinetics, occurs when a non-uniform AC field is applied to a particle, creating a frequency-dependent dipole on the particle's surface. The non-uniform field and dipole create a force on the particle, called the dielectrophoresis force, or F_{DEP}. This allows for manipulation and study of the particle's properties, though the particle may not have a native charge.[35] Electroosmosis, or electrokinetic flow, is a common side effect of electric field application to a microfluidic channel. It is a widely studied tool in microfluidics and is used to flow fluid between zones of interest. Multiple factors affect electrokinetic flow such as conductivity, zeta potential, diffusion, and liquid viscosity. Conductivity arguably plays the largest role due to the temperature-dependent nature of conductivity and can lead to an often-undesired side effect: Joule heating.[36]

Electrothermal heating, or Joule heating, occurs due to the conductive nature of fluid in a microfluidic channel and is usually an undesired side effect of AC electrokinetics. Joule heating is one of many considerations taken into account when designing microfluidic and electrical systems.[37] Most research attempts to avoid Joule

heating due to its ability to change temperature-dependent conductivity, inhibit biochemical reactions, and alter system fluid flow assumptions.[38,39] In this research however, Joule heating is harnessed to drive NAA. More details and theory about Joule heating are expanded upon in Section 2.2.3.

2.2.1. Isotachophoresis

Isotachophoresis is a common electrophoretic concentration technique that operates based on an analyte's electrophoretic mobility. A sample is injected between two electrolytes, called the leading electrolyte (LE) and the terminating electrolyte (TE). When subjected to an electric field in the direction of flow, analytes and electrolytes migrate and stack through the device according to their electrophoretic mobilities, with TE having the lowest mobility, followed by the analyte, followed by the LE ($\mu_{TE} < \mu_A < \mu_{LE}$).[25,26,40] ITP was typically performed for capillary electrophoresis applications but has become used often in microfluidics. This has led to two main categories of microfluidic ITP: plateau mode and peak mode. Both methods involve the concentration of samples between other species, however, the difference lies in the amount of analyte concentrated. In plateau mode, the amount of analyte is enough to significantly contribute to the electrical properties of the system such that during operation, a maximum concentration of concentrated sample is reached, as depicted in Figure 2.1. The sample migrates to a zone in between the LE and TE, with some overlap with the LE and TE zones. Peak mode, on the other hand, concentrates trace amounts of sample, where the sample amount does not majorly contribute to the electrical properties of the system. The sample concentrates to a high degree, creating a distinct zone with sharp

interfaces between the LE and TE. The distribution profile is typically Gaussian in shape for peak mode ITP.[41–43]

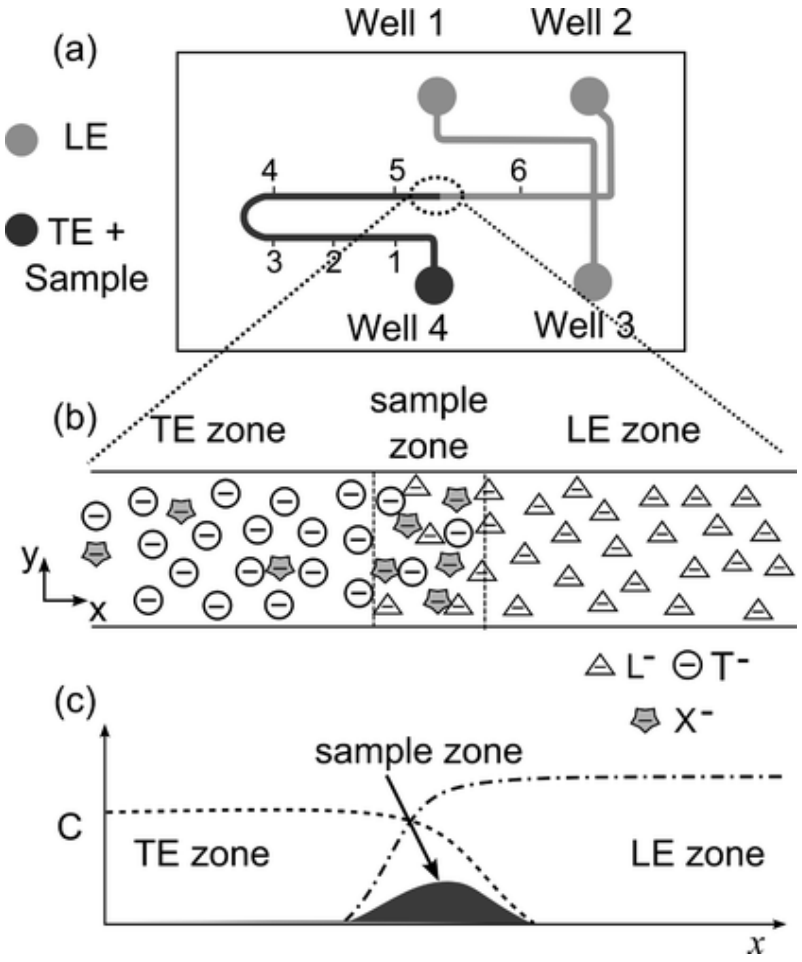

Figure 2.1 Schematic of isotachophoresis. The sample is mixed with the TE, flowed with the LE, then exposed to an electric field. The sample stacks between the LE and TE, creating a plateau zone, enabling extraction and analysis.[42]*

The ability to concentrate and stack samples to a high degree makes ITP an attractive tool for sample preparation, an important part of diagnostics. Dyes have been easily concentrated up to a million-fold using microfluidic ITP, so performing ITP on other biologically relevant molecules was the next logical step.[42,44] The main motivation

* – Reprinted with permission from Khurana, T. K.; Santiago, J. G. Sample Zone Dynamics in Peak Mode Isotachophoresis. *Anal. Chem.* **2008**, *80* (16), 6300–6307. Copyright 2008 American Chemical Society

for performing ITP on biological samples is to remove NAA inhibitors from solution, allowing for off-chip amplification of nucleic acids.[6] DNA ITP was first performed by Kondratova *et al.* and has since become a common target of microfluidic ITP, preparing samples for off-chip analysis methods such as gel electrophoresis or the quantitative polymerase chain reaction (qPCR). Juan Santiago's lab in particular has contributed extensively to the field of microfluidic ITP.[45–47] Other samples that have been concentrated include ribonucleic acid (RNA) and proteins, both from crude cell lysates.[48–51] Additionally, it has been shown that nucleic acids and proteins can be separated simultaneously, in opposite directions, using two sets of leading and terminating electrolytes, a technique called bi-directional isotachophoresis.[52,53] The largest drawback of the works described above is that those devices must be run in a batch manner with fixed volumes. This limits both the amount of sample that can be prepared and the ability of these devices to be integrated with other microfluidic devices. One technique that can overcome these limitations is free-flow isotachophoresis (FFITP). FFITP differs from batch ITP because, in FFITP, the electric field is applied perpendicularly to the direction of fluid flow, enabling continuous stacking and concentration of samples, as shown in Figure 2.2[41,54,55] One of the first works that used FFITP was that of Janasek *et al.* where fluorescein, eosin G, and acetylsalicylic acid were rapidly concentrated in under a minute using a FFITP device fabricated with PDMS soft lithography.[25] Other uses of FFITP include concentration of *E. herbicola* and direct integration of FFITP with electrospray ionization mass spectroscopy.[56,57]

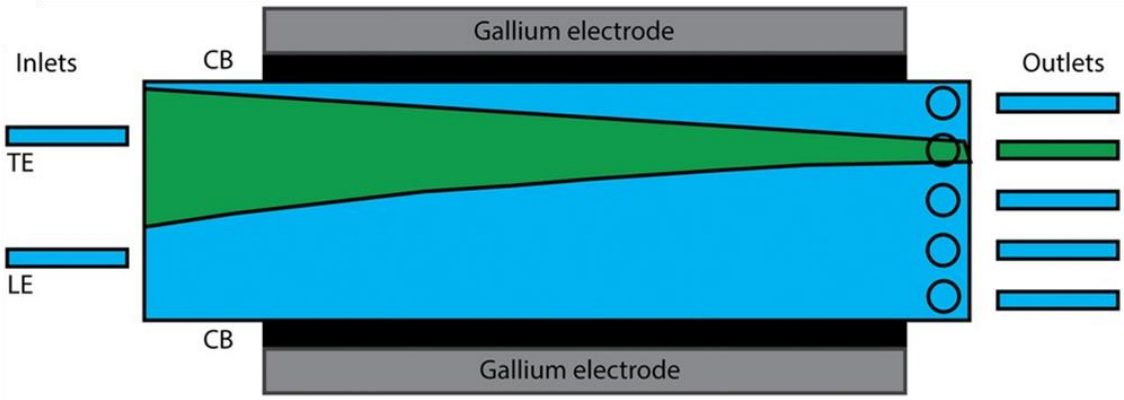

Figure 2.2 Schematic of free-flow isotachophoresis. Electric potential is applied at the gallium electrodes (top and bottom), perpendicular to the direction of flow (left to right). This enables continuous analyte stacking and the ability to process large sample volumes.[55]*

FFITP requires large voltages to produce stacking and concentration, so Fu *et al*. developed an improvement to FFITP where conductive walls made of carbon black mixed with PDMS were incorporated during fabrication. These conductive walls bridged the gap between the electrodes and the flow channel, lowering the voltages required for ITP and dramatically reducing Joule heating and bubble generation commonly seen during FFITP. Using this new device, they were able to concentrate and separate Rhodamine B and Fluorescein.[55]

2.2.2. Teíchophoresis

While isotachophoresis is an effective tool to concentrate and separate biomolecules, achieving concentrations factors up to two million-fold, ITP does present some limitations.[44] First, the presence of two buffers, LE and TE, place design constraints on the system because the LE and TE must be chosen with sample identity in mind. This limits the buffers that can be used in ITP. Second, having two buffers and the

* – Reprinted with permission from Fu, X.; Mavrogiannis, N.; Ibo, M.; Crivellari, F.; Gagnon, Z. R. Microfluidic Free-Flow Zone Electrophoresis and Isotachophoresis Using Carbon Black Nano-Composite PDMS Sidewall Membranes. *ELECTROPHORESIS* **2017**, *38* (2), 327–334. Copyright 2017 John Wiley & Sons

sample is experimentally inconvenient. In both batch and free-flow ITP, multiple fluidic inlets and fluidic plugs must be operated all at once, requiring complex fluidic control systems.

To alleviate these issues, Doria and Gagnon developed a novel electrokinetic concentration technique called teíchophoresis (TPE). TPE improved upon FFITP in two ways. First, the LE was replaced with a conductive wall made of PDMS doped with carbon nanotubes (CNT), as seen in Figure 2.3(a) and Figure 2.3(b). In ITP, the LE acts as a no-flux zone and the TE is an area of high flux. The sample, stacked between the LE and TE, cannot penetrate either zone. A conductive wall cannot physically move, so it can act as a "perfect" LE, being a no-flux zone while still allowing electric potential to flow across the device. This enables sample stacking against the conductive wall using only one electrolyte, the terminating electrolyte. Second, the traditional DC voltage used in ITP is replaced with an asymmetric pulsed square wave voltage, as seen in Figure 2.3(c). DC voltage leads to electrolysis and bubble generation within microchannels, interfering with device operation. A pulsed square wave voltage cyclically switches off at short timescales (milliseconds) prior to nucleation but is still capable of delivering an electric field across the channel. This advantage is demonstrated in Figures 2.3(d) and 2.3(e). Doria and Gagnon used TPE to concentrate and separate charged fluorescent dyes from one another, achieving a 60,000-fold concentration increase. They also showed that TE presence is not required for analyte-wall stacking, but the presence of a TE increases analyte concentration degree during TPE.[10] While TPE has shown to be effective in concentrating and separating dyes, it has yet to be explored with biologically-relevant molecules. However, given ITP's success at concentrating and

separating biomolecules and TPE's similarity to ITP, TPE is hypothesized to be compatible with biomolecules as well.

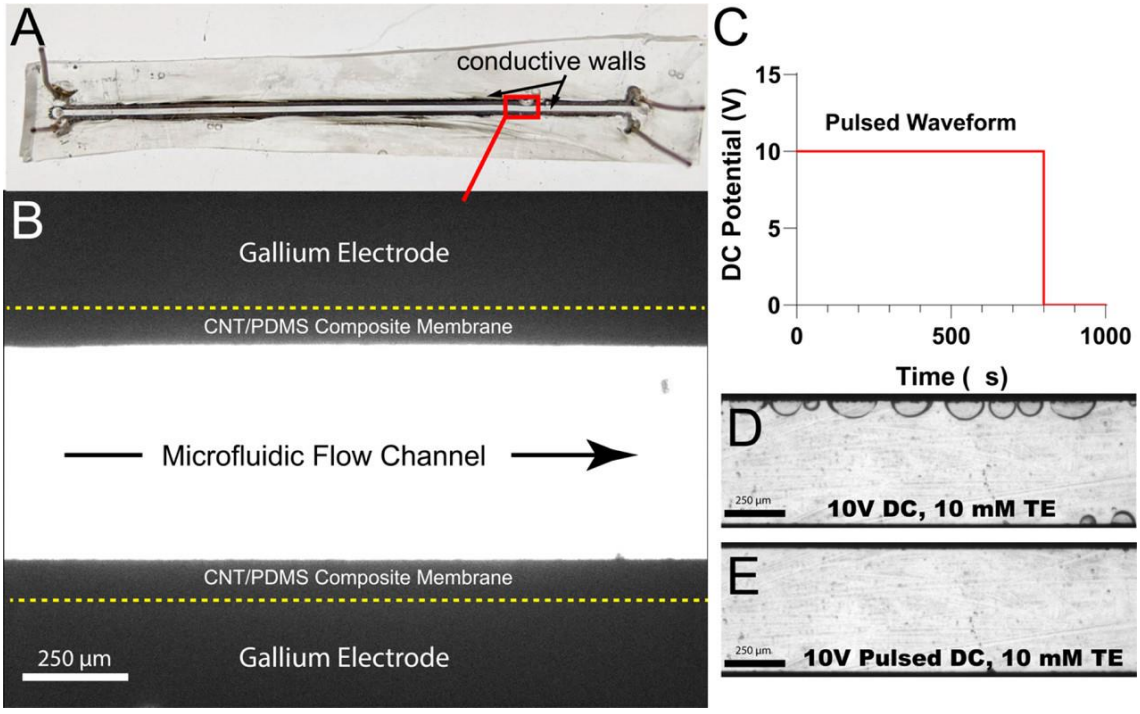

Figure 2.3 Teíchophoresis overview. (a) Single PDMS microchannel device with two conductive sidewall membranes. (b) Each conductive wall consists of a solid metal gallium electrode adjacent to a polymeric CNT/PDMS membrane. (c) Pulsed DC electric field is used to drive TPE in the microchannel. (d) Non-pulsed DC field leads to bubble generation at the electrodes in the microchannel. (e) Pulsed DC field eliminates bubble formation from electrolysis in the microchannel.[10]*

2.2.3. Joule Heating

Joule heating, or Ohmic heating, is a fundamental heating method used in electronics. First observed in the 1840s by James Prescott Joule, Joule heating occurs when an electric current is applied to a resistive element, generating heat.[58,59] This is due to internal energy generation of the resistor, which are typically electronic wires or

* – Reprinted with permission from Doria, S.; Gagnon, Z. Continuous Molecular Concentration and Separation Using Pulsed-Field Conductive-Wall Single-Buffer Teíchophoresis. *Anal. Chem.* **2022**, *94* (39), 13481–13488. Copyright 2022 American Chemical Society

conductive fluids. Many system properties go into determining the heating effect, such as element resistivity (or conductivity), amount of current applied, and other thermal, electrical, and physical properties.[60] While Joule heating in solids is encountered often in everyday life, Joule heating in liquids is not as widely encountered; it is more often used in laboratory settings. Unlike other electrical heating methods, such as microwave or inductive heating, the electrodes must be placed in direct contact with the resistive element to produce Joule heating.[59] Typical uses of Joule heating include light bulbs, space heaters, laboratory hot plates, and food pasteurization.[59,61,62]

The main governing equation of Joule heating is given by Eq. (2.1), where I is the current passed through the element, R is the element resistance, and Q is the heat or power generated per unit volume[63]

$$Q = I^2R. \quad (2.1)$$

The following equations, derivations, and conclusions come from the book AC Electrokinetics: colloids and nanoparticles, by Hywel Morgan and Nicolas G. Green.[39] Joule heating is influenced by frequency of the applied current, conductivity of the resistive element, and voltage applied to the system. In addition to the overall amount of heat generated, Joule heating causes gradients in both temperature and conductivity, leading to an overall electrothermal body force upon the fluid, f_e. Joule heating can be characterized by two main equations: the temperature balance equation and the electrothermal body force equation, both of which explain relationships between Joule heating and conductivity, temperature, voltage, and frequency. To start, the temperature balance equation (similar to the Navier-Stokes Equation) is simplified by neglecting the viscous dissipation term due to its small order of magnitude

$$\rho_m c_p \frac{\partial T}{\partial t} + \rho_m c_p \mathbf{u} \nabla T = k\nabla^2 T + \sigma|\mathbf{E}|^2, \quad (2.2)$$

where ρ_m is the mass density, c_p is the specific heat at constant pressure, k is the thermal conductivity, $\sigma|\mathbf{E}|^2$ is the Joule heating term (σ – electrical conductivity) ($\mathbf{E}$ – electric field), and $\mathbf{u}$ is the velocity vector.

At high frequencies, it is assumed that the heating system is at steady state, so the first term is canceled $\left(\frac{\partial T}{\partial t} = 0\right)$. In addition, due to the microscale of the system, the velocity component can be decoupled from the thermal and electrical components, meaning the momentum component of the equation can be ignored. Solving the resulting equation with a time average of Joule heating yields the following relationship between Joule heating and the temperature gradient

$$k\nabla^2 T + \langle \sigma|\mathbf{E}|^2 \rangle = 0. \quad (2.3)$$

Since the electric field, E, is a function of voltage and distance (E = V/d for a constant field, where d is the length over which the voltage is applied), Eq. (2.3) shows that temperature changes due to Joule heating scale linearly with both conductivity and square of applied voltage, or quadratically with applied voltage. This can be simplified to a one-dimensional relationship, where temperature is proportional to both conductivity and voltage squared

$$\Delta T \approx \frac{\sigma V^2}{k}. \quad (2.4)$$

The second equation, the electrothermal body force equation, shows how frequency influences Joule heating. The derivation starts with the equation for the electrical body force, Eq. (2.5). The first term on the right-hand side is the Coulomb

force, the second term is the dielectric force, and the third term is the electrostriction force, which can be ignored for incompressible fluids

$$\mathbf{f}_e = \rho\mathbf{E} - \frac{1}{2}|\mathbf{E}|^2\nabla\varepsilon + \frac{1}{2}\nabla\left(\rho_m\left(\frac{\partial\varepsilon}{\partial\rho_m}\right)_T|\mathbf{E}|^2\right), \quad (2.5)$$

where ρ is the charge density and ε is the permittivity. Rewriting Eq. (2.5) in terms of permittivity and conductivity gradients, while manipulating electric field terms and applying Gauss's Law (divergence of an electric field), yields Eq. (2.6), which is the time-average body force on a particle according to permittivity and conductivity gradients

$$\langle\mathbf{f}_e\rangle = \frac{1}{2}\mathrm{Re}\left[\left(\frac{\sigma\nabla\varepsilon - \varepsilon\nabla\sigma\cdot\mathbf{E}_o}{\sigma + i\omega\varepsilon}\right)\mathbf{E}_o^* - \frac{1}{2}|\mathbf{E}_o|^2\nabla\varepsilon\right], \quad (2.6)$$

where Re is Reynold's Number, ω is the frequency, and $\mathbf{E}_o^*$ is the complex conjugate of $\mathbf{E}_o$ (electric field). Rewriting Eq. (2.6) to be in terms of temperature gradients, rather than permittivity and conductivity, we arrive at Eq. (2.7), the electrothermal body force on a fluid

$$\langle\mathbf{f}_e\rangle = \frac{1}{2}\mathrm{Re}\left[\left(\frac{\sigma\varepsilon(\alpha - \beta)}{\sigma + i\omega\varepsilon}\right)(\nabla T\cdot\mathbf{E}_o)\mathbf{E}_o^* - \frac{1}{2}\varepsilon\alpha|\mathbf{E}_o|^2\nabla T\right], \quad (2.7)$$

where $\alpha = \left(\frac{1}{\varepsilon}\right)\left(\frac{\partial\varepsilon}{\partial T}\right)$ (the permittivity and temperature correlation) and $\beta = \left(\frac{1}{\sigma}\right)\left(\frac{\partial\sigma}{\partial T}\right)$ (conductivity and temperature correlation). As seen in Eq. (2.7), there is a frequency dependence in the force on a particle due to a temperature gradient, along with a conductivity and voltage dependence.

This knowledge of Joule heating can be taken a step further by considering electrode geometry. We start with the electric field equation for a coplanar two-electrode geometry in the $\hat{\theta}$ direction, like the one found in Figure 4.1(b)

$$\mathbf{E}(r,\theta) = \frac{2}{\pi}\frac{V_o}{r}\hat{\boldsymbol{\theta}}, \quad (2.8)$$

where r is the radius from center of the point of interest and V_o is the applied AC voltage. This electric field then heats conductive fluid, such that the time-average power density, $\langle W \rangle$, is

$$\langle W \rangle = \frac{1}{2}\left(\sigma \mathbf{E}\cdot\mathbf{E}^*\right) = \frac{2}{\pi^2}\frac{\sigma V_o^2}{r^2}. \quad (2.9)$$

Together with Eq. (2.3), Eq. (2.9) yields the temperature gradient for the given geometry

$$\nabla T = \frac{1}{\pi k}\frac{\sigma V_o^2}{r}\left(1 - \frac{2\theta}{\pi}\right)\hat{\boldsymbol{\theta}}. \quad (2.10)$$

Finally, substituting Eq. (2.10) into Eq. (2.7), we arrive at the electrothermal body force on the fluid for the given electrode geometry

$$\langle \mathbf{f}_e \rangle = \frac{2}{\pi^3 k}\frac{\varepsilon\delta V_o^4}{r^3}\Pi\left(1 - \frac{2\theta}{\pi}\right)\hat{\boldsymbol{\theta}}, \quad (2.11)$$

$$\Pi = \left[\frac{\alpha - \beta}{1 + (\omega\tau_q)^2} - \frac{\alpha}{2}\right], \quad (2.12)$$

where τ_q is the charge relaxation time (ε/σ).

Looking at Eqs. (2.3), (2.4), (2.7), (2.10), (2.11), and (2.12), we can see that the fluid force is influenced by current frequency and that the temperature change of the fluid due to Joule heating is proportional to electrical conductivity and square of the applied voltage.[39] If this temperature-voltage relationship is observed experimentally, the heating experienced by a system is likely Joule heating.

2.3. DNA Amplification

2.3.1. PCR Mechanisms

A way to enrich nucleic acids is to target and amplify their sequences using biochemical techniques such as the polymerase chain reaction (PCR), which works by

utilizing a thermostable DNA polymerase to construct DNA strands using free nucleotides. There are three major steps to PCR: denaturation, annealing, and extension. Denaturation, which breaks the hydrogen bonds between nucleotides in double-stranded DNA (dsDNA) to produce single-stranded DNA (ssDNA), occurs at 95 ºC – well above the melting temperature (T_m) of the template DNA. The reaction is then cooled to ~55 – 60 ºC to anneal custom-designed primers to their complementary sequences on the ssDNA. The annealing temperature is determined by the T_m of the primers, meaning that primer design is a fundamentally important aspect of PCR. If primers are not properly designed, they may bind non-specifically to DNA strands or each other resulting in undesired amplification or primer dimers.[64]

The final step is extension, where DNA polymerase binds to the primer-ssDNA complex at ~72 ºC and polymerizes a new, complementary DNA strand using free deoxynucleotide triphosphates (dNTPs) in the reaction mixture. Many modern PCR mixes have been designed to perform annealing and extension steps at the same temperature, usually 60 ºC. These temperatures are cycled at least thirty times to generate billions of DNA copies over the course of the reaction.[64]

One modification that can be made to PCR is to add a fluorescent and DNA-intercalating agent to the reaction (i.e., SYBR Green or Ethidium Bromide), which increases in fluorescence during the reaction as it intercalates new DNA being polymerized. This fluorescent addition to PCR is called quantitative PCR (qPCR). This fluorescence increase can be tracked using a fluorescence-measuring instrument, enabling real-time analysis of reaction progress and relative or absolute quantities of both starting template and amplified DNA.[65]

2.3.2. LAMP Mechanisms

Another amplification method that has been developed is loop-mediated isothermal amplification (LAMP). LAMP works similarly to PCR, utilizing primers and a thermostable DNA polymerase to amplify DNA, however, there are some key differences, such as the number of primers, amplification temperature, and lack of thermal cycling. Regions of the 5' -> 3' strand of the template are designated B3, B2, B1, F1c, F2c, and F3c. The complementary strand (3' -> 5') contains complementary sequences to the 5' -> 3' strand (B3c, B2c, B1c, F1, F2, and F3). LAMP utilizes four or six primers (FIP, BIP, F3, B3, LoopF, and LoopB) to create an amplification loop with a dumbbell structure, which is used to make ever-larger continuous DNA copies, as seen in Figure 2.4. The result is a ladder of DNA strands of multiple sizes, rather than multiple copies of a single size, as with PCR.[66,67]

The process starts with displacement of the dsDNA template by the FIP Primer (containing sequences F2 and F1c), which generates a complementary strand, except for the F1c section of the FIP primer. F3 then displaces the newly amplified strand by binding to F3c and is amplified as a complement to the original dsDNA strand. The resulting strand then has a one-sided "dumbbell" structure, due to the self-hybridization of the complementary sequences of F1 and F1c. On this new strand, the BIP primer (containing sequences B1c and B2) binds and is amplified with the rest of the strand. The B3 primer then displaces the strand formed by BIP, resulting in the critical Loop Strand, which has a "dumbbell" structure due to the self-hybridization of the B1-B1c and F1-F1c complementary sequences. This loop strand has two amplification sites – the 3' end and the F2c sequence – where the FIP primer binds. From there, ever longer

strands of dsDNA are amplified using this loop structure, leading to long, cauliflower-like concatemers. After the LAMP process was developed using four primers, Nagamine et al. accelerated the reaction with the addition of two primers, LoopF and LoopB. This brought amplification time down from an hour to 30 minutes. The result of LAMP is a mixture of DNA strands of various sizes, created from the critical Loop Strand.[66,67] Unlike PCR, LAMP takes place at one temperature, 65-73 ºC, rather than at multiple temperatures.[66,67] Due to the specific nature of the reaction, LAMP can generate large amounts of DNA in a short amount of time, making it an attractive alternative to PCR. While LAMP's temperature requirements make it easier to incorporate into microfluidics, designing multiple primers makes LAMP difficult to accomplish from a biological perspective.

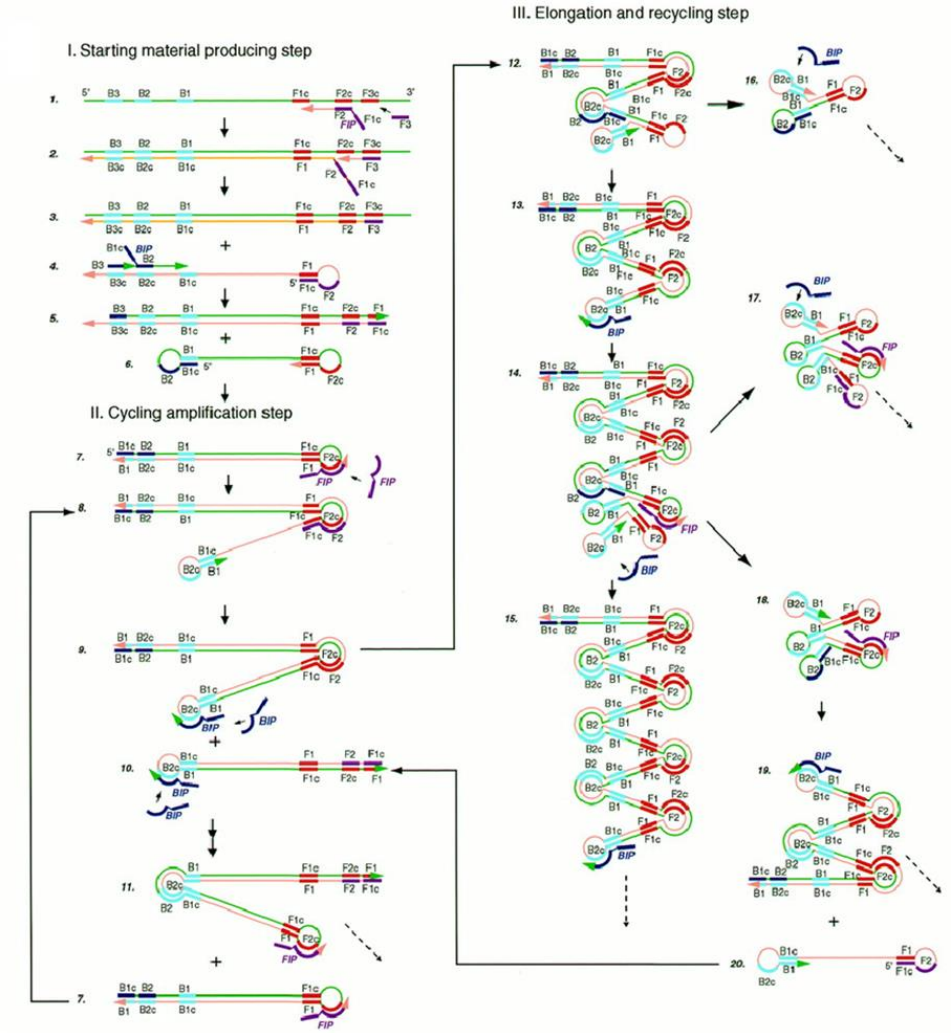

Figure 2.4 Diagram of the LAMP reaction. A Loop Strand is generated during the Starting material producing step, which is then used to create multiple DNA strands of varying sizes during the Cycling amplification step and the Elongation and recycling step.[66]*

2.3.3. Microfluidic DNA Amplification

Given the power and popularity of PCR, microfluidic integration of this technique has undergone significant effort and technical development over the last two decades. The main technical methods for microfluidic PCR include: (1) pumping fluid cyclically between two thermally controlled fluidic channel zones with PCR-specific

* – Reprinted with permission from Nagamine, K.; Hase, T.; Notomi, T. Accelerated Reaction by Loop-Mediated Isothermal Amplification Using Loop Primers. *Mol. Cell. Probes* **2002**, *16* (3), 223–229. Copyright 2022 Elsevier

denaturing and annealing temperatures, (2) driving fluid in a single direction through a series of thermal serpentine turns, where the number of channel serpentines equates to the number of PCR cycles, and (3) fluidic devices that employ boundary-driven resistive heating elements, some of which can even output qPCR curves on a built-in display.[68–70]

In PCR, temperature control and regulation form the essential constraint for engineering design and operation. In general, most microfluidic PCR devices regulate temperature within either stationary reaction chambers or continuous flow channels. The stationary reaction chamber setup is similar to a traditional thermal cycler system: the sample is contained in a fixed microscale volume and heated via a resistive heater fixed underneath the reaction chamber and thermally cycled between the PCR annealing and denaturing temperatures. Alternatively, continuous flow systems typically flow sample between heated zones required by the PCR temperature conditions. While both of these thermal methods have shown to be effective, they do present inherent technical drawbacks, such as the use of bulky resistive heaters fabricated outside of the microfluidic devices, fixed cycle numbers for continuous flow systems due to a fixed fluidic architecture, and thermal gradients present in boundary-driven heating.[9]

In addition to how liquid control is handled, the actual heating methods used in microfluidic PCR form an important design constraint and can limit device performance. In the previously described devices, heating methods were largely resistor arrays with thermocouples and thermostated copper blocks. Both methods required macroscale heating elements fabricated outside a microscale reaction chamber limiting portability, production cost, and device complexity.[68–70]

One alternative PCR heating method used an electric current to resistively heat the reaction chamber via a proportional-integral-derivative (PID)-controlled Joule heating element. Such an approach utilized the conductive nature of PCR to generate resistive heat. In that setup, the PCR mixture was heated by DC Joule heating. However, the DC voltage generated fluid flow down the channel, so the polarity of the voltage was flipped every 5 seconds, essentially creating low-frequency AC voltage. This low frequency led to water electrolysis, which required atmosphere venting of the generated gases. While the chip amplified DNA, the setup has room for improvement, particularly in the areas of chip thermal response, minimization of fluid flow, and gas generation. In addition, the electrodes were not in direct contact with the fluid, rather, the system had insert pins that acted as leads for the electrodes.[71] A similar method used a low frequency (60 Hz) current applied across a conductive solution to induce Joule heating and drive PCR. While both reported Joule heating methods were able to use electric current to amplify DNA, both methods required separation and venting of electrochemical reaction byproducts due to electrolysis at the anode and cathode electrodes that were used to apply the Joule heating current. These works suggest that an electrical current can be used to drive biochemical reactions in samples.

2.4. Paper Microfluidics

Paper microfluidics was first developed in 2007 by George Whitesides' group at Harvard University. They patterned paper using photolithography to create barrier zones to control flow and embedded colorimetric sensors for detecting glucose and protein.[72] Prior to this, paper microfluidic devices, or μPADs, had primarily existed in the form of lateral flow assays (LFAs) for applications such as immunoassays or pregnancy tests.[73]

Since then, μPADs have evolved to have many uses such as transport, filtration, storage, concentration, valving, and sample preparation (lysis, purification, nucleic acid extraction), among others.[74] This has been accomplished through newer methods of patterning μPADs, such as wax printing and inkjet printing, with wax printing being the most common metho.[75] Recently, LFA technology has helped ease the burden of the COVID-19 pandemic by enabling rapid and point-of-care testing for COVID antigens, with varying degrees of accuracy.[76] The recent success of μPADs has shown that it can become a viable alternative to traditional microfluidic technologies.

Paper microfluidics traditionally relies upon wicking to drive fluid flow, where fluid flows through a porous paper channel via capillary action. Many paper and fluid properties affect capillary action through paper including paper type, fluid type, channel dimensions, evaporation rate, temperature, and humidity. Liu *et al.* analyzed mathematical models that were developed for fluid flow via wicking, both without and with evaporation. To model fluid flow without evaporation, the Lucas-Washburn equation was developed

$$h_0 = \sqrt{\frac{4\sigma\cos(\theta)}{\mu} \cdot \frac{K}{\varepsilon R}} \cdot t^{1/2}, \quad (2.13)$$

where h_0, ε, σ, μ ,θ, K, R, and t are the theoretical wicking front height, effective porosity, interfacial tension, viscosity, contact angle, permeability, effective pore radius, and time, respectively.[77,78] The theoretical liquid speed, S_0, was then defined as the change in wicking height with respect to time

$$S_0 = \frac{dh_0}{dt} = \sqrt{\frac{\sigma\cos(\theta)}{\mu} \cdot \frac{K}{\varepsilon R}} \cdot t^{-1/2}. \quad (2.14)$$

Furthermore, the theoretical wicking fluid mass, m_0 was defined as

$$m_0 = \rho\varepsilon\omega\delta h_0 = \rho\omega\delta\sqrt{\frac{4\sigma\cos(\theta)}{\mu}\cdot\frac{K}{R}\varepsilon}\cdot t^{1/2}, \quad (2.15)$$

where ρ, ω, and δ are the density, strip width, and strip thickness, respectively. Eqs. (2.13), (2.14), and (2.15), describe wicking without evaporation and only consider viscous resistance and capillary forces, while ignoring inertial forces and gravity.[79]

To describe capillary action with evaporation, Liu *et al.* detailed steps to incorporate evaporation into the wicking fluid flow model. The wicking height considering evaporation, h_{ev} was given as[80]

$$h_{ev} = 2N\cdot e^{-Mt}\int_0^{\sqrt{t}} e^{Mt^2}dt, \quad (2.16)$$

where $M = \frac{2m_{ev}^*}{\rho\varepsilon\delta}$, $N = \sqrt{\frac{\sigma\cos(\theta)}{\mu}\cdot\frac{K}{\varepsilon R}}$, and $m_{ev}^* = \left(p_w - p_v\right)\times\frac{(0.089 + 0.0782V_a)}{\gamma}$. γ, p_w, p_y, and V_a are latent heat of vaporization of water, water saturated pressure, partial pressure of vapor in air, and air flow rate, respectively. This gave the predicted wicking mass as

$$m_e = \rho\varepsilon\omega\delta h_{ev}. \quad (2.17)$$

Finally, the predicted wicking speed, S_{ev} was

$$S_{ev} = \frac{dh_{ev}}{dt} = N\cdot t^{-1/2} - 2M\cdot N\cdot e^{-Mt}\int_0^{\sqrt{t}} e^{Mt^2}dt. \quad (2.18)$$

Eqs. (2.16), (2.17), (2.18), when compared graphically with Eqs. (2.13), (2.14), and (2.15), yielded Figure 2.5 (from Liu *et al.*).[78] Figure 2.5(a) depicts fluid wicking height (h) versus time, both with and without evaporation, showing that experimental data and data modeled without evaporation do not agree. Fig. 2.5(b) depicts liquid wicking liquid speed (S) versus time both with and without evaporation, showing that regardless of evaporation, wicking speed decreases dramatically after just a few minutes of flow. Finally, Figure 2.5(c) depicts fluid wicking mass versus time, both with and without

evaporation, showing that once again, experimental data and data modeled without evaporation do not agree. From analyzing these plots, evaporation plays a large factor in the performance of µPADs at large time scales. Thus, when developing paper microfluidic devices, evaporation and flow rates are necessary considerations.

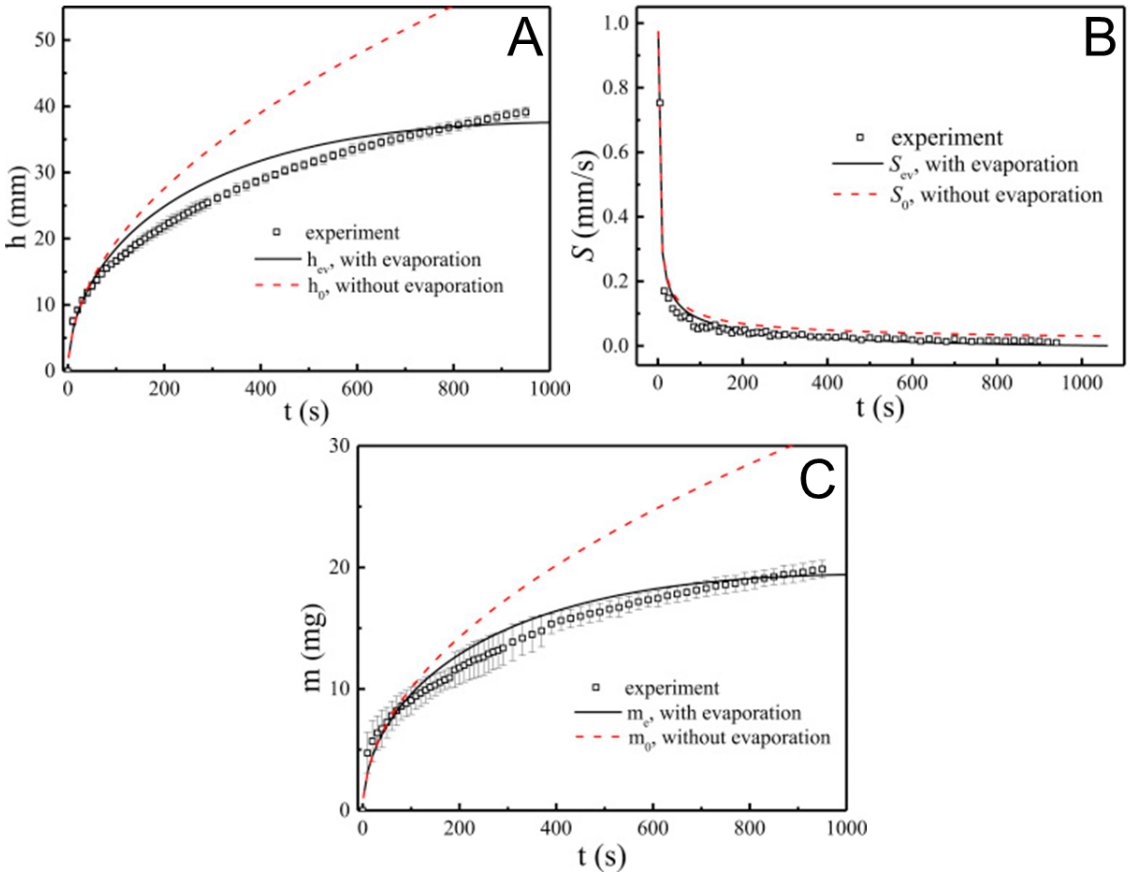

Figure 2.5 Quantification of fluid flow through paper via capillary action. Wicking height (a), wicking speed (b), and wicking mass (c) were modeled both with and without evaporation and compared to experimental data.[78]*

* – Reprinted with permission from Liu, Z.; Hu, J.; Zhao, Y.; Qu, Z.; Xu, F. Experimental and Numerical Studies on Liquid Wicking into Filter Papers for Paper-Based Diagnostics. *Appl. Therm. Eng.* **2015**, *88*, 280–287. Copyright 2015 Elsevier

2.4.1. Paper Microfluidic Nucleic Acid Amplification

NAA has been well studied using traditional microfluidics, but NAA using paper microfluidics is a recent innovation in the microfluidics field. The most common amplification method, PCR, has yet to be achieved properly on a paper microfluidic platform, though PCR has been achieved in the presence of paper.[74,81] Other amplification methods, such as recombinase polymerase amplification (RPA) and helicase-dependent amplification (HDA), have been achieved on paper as well. RPA and HDA are both isothermal amplification techniques (37 – 42 ºC for RPA and 65 ºC for HDA), making them ideal candidates for paper microfluidics due to their lack of thermal cycling.[74,82–84] LAMP has also been achieved on paper, first occurring in 2011 using FTA cards.[85] In addition to FTA cards, LAMP has been achieved on glass fibers, chromatography paper, polyethersulfone (PES), and polycarbonate (PC).[86,87] The methods described above for NAA relied on pre-drying amplification reagents on paper then rehydrating the paper with sample prior to amplification and relied on hot plates or incubators to heat their reactions. A method that does not involve pre-preparation of amplification reagents and does not rely on bulky heating equipment would be advantageous. All that would be required would be an upstream sample preparation step, such as teíchophoresis, which is discussed in the next section, Section 3.

3. FREE-FLOW BIOMOLECULAR CONCENTRATION AND SEPARATION OF PROTEINS AND NUCLEIC ACIDS USING TEÍCHOPHORESIS*

3.1. Overview

The ability to preconcentrate, separate, and purify biomolecules, such as proteins and nucleic acids, is an important requirement for the next generation of portable diagnostic tools for environmental monitoring and disease detection. Traditionally, such pretreatment has been accomplished using large, centralized liquid- or solid-phase extraction equipment, which can be time-consuming and requires many processing steps. Here, we present a newly developed electrokinetic concentration technique, teíchophoresis (TPE), to concentrate and separate proteins, and to concentrate nucleic acids. In TPE, a free-flowing sample is exposed to a perpendicular electric field in the vicinity of a mass-impermeable conductive wall and a conductive terminating electrolyte (TE), which creates a high electric field strength zone between the lower mobility sample and the no-flux barrier. Unlike a similar electrokinetic concentration method, isotachophoresis (ITP), TPE does not require a leading electrolyte (LE), yet still enables a continuous field-driven electrophoretic ion migration across the channel and a free-flowing biomolecular concentration at the conductive wall. Here, we demonstrate the use of free-flow TPE (FFTPE) to manipulate biomolecular samples containing proteins or nucleic acids. We first use TPE to drive a 6.6-fold concentration increase of avidin-FITC, and also demonstrate protein separation and stacking between ovalbumin-

* – Adapted with modifications from Doria, S.; Yost, J.; Gagnon, Z. Free-Flow Biomolecular Concentration and Separation of Proteins and Nucleic Acids Using Teíchophoresis. *Talanta* **2023**, *255*, 124198. Copyright 2023 Elsevier

fluorescein and BSA-AlexaFluor 555, both without the use of a conventional LE. Further, we utilize TPE to perform a 21-fold concentration increase of nucleic acids. Our results show that TPE is biocompatible with both proteins and nucleic acids, requires only 10 V DC, produces no significant sample pH changes during operation, and demonstrates that this method can be used as an effective sample pretreatment to prepare biological samples for downstream analysis in a continuous free-flowing microfluidic channel.

3.2. Introduction

Micro total analysis systems (μTAS) are miniaturized liquid handling systems, or platforms that are capable of process unit operations, including analyte detection and fluidic routing, within a single device or integrated system. Relative to their benchtop counterparts, μTAS platforms are ideally portable, lightweight, low-cost, require low sample volume, and feature rapid analysis times. Furthermore, μTAS platforms can be engineered to handle a broad range of biomolecules, including small molecules, proteins, and nucleic acids for applications in point-of-care (POC) diagnostics, environmental monitoring, metabolic profiling, and single-cell analysis.[88–91] While significant advancements in μTAS device microfabrication, target analyte sensing, and optical integration have been made, on-chip preparation of raw or "dirty" liquid samples remains relatively underdeveloped and prevents many μTAS platforms from making a larger impact and preventing use in fully automated and portable diagnostic problems.[92] Specifically, target analyte preconcentration for detection of dilute analytes and separation of inhibitors from analytical matrices, entirely on μTAS devices, remains challenging. Downstream biomolecular analytical methods such as the polymerase chain

reaction (PCR) and protein immunoassays have been successfully miniaturized, but can still rely on off-chip processes to remove inhibitors to enable replication or rely on preconcentration techniques to improve sensitivity.[93–97] Such off-chip processes create an operational bottleneck which minimizes the usefulness and impact of these μTAS tools.

The current state-of-the-art method for purification of nucleic acids and proteins is solid phase extraction (SPE) in which molecular targets are purified by adsorption on a solid silica membrane or specialized adsorption beads.[98] Unfortunately, SPE can be tedious, time-consuming, and is often a multi-step batch process requiring specialized materials, including chaotropic agents and organic solvents. Several electrokinetic methods including capillary zone electrophoresis (CZE), free flow electrophoresis (FFE), isotachophoresis (ITP), free flow ion concentration polarization focusing (FF-ICPF), and dielectrophoresis (DEP), have been suggested as solutions to on-chip sample processing problems.[99–104] These methods leverage the electrophoretic mobilities of charged species to both preconcentrate biomarkers and achieve high-resolution separations of analytes. There is, however, a research gap in analyzing how particles, including proteins and nucleic acids, interact with device boundaries during aforementioned sample processing techniques.[105]

ITP has been shown to be compatible with several biomarkers, including small molecules, proteins, and nucleic acids.[46,51,89,106] Furthermore, ITP is a powerful concentration and separation technique, capable of resolving chiral molecules in separation experiments, and achieving high concentration factors (up to 2 million-fold) in enrichment experiments.[44,107,108] Additionally, ITP has been applied to DNA samples

to induce rapid, on-chip hybridization and achieve concentration factors of up to 60-fold.[109,110] Although these electrokinetic methods have proven to be effective, they rely on batch systems, which feature low throughput and require highly skilled operators. Furthermore, ITP specifically relies on a multi-electrolyte system, which can make experimental design and fluidic control tedious. In 2017 Fu et al. developed microfluidic free-flow isotachophoresis (FFITP), a high throughput, free-flow alternative to ITP. Although FFITP improved upon the throughput of conventional batch ITP, the fluidic device required one to simultaneously handle the flow control of four fluidic inlets.[55] In an effort to eliminate the need for the leading and trailing buffer system, in 2022 Doria et al. presented a new electrophoretic concentration and separation technique, teíchophoresis (TPE), which can serve as a new free-flow, electrophoretic process for concentrating and separating analytes based on their differing electrophoretic mobilities. Deriving from the Greek word teícho, meaning wall, TPE combines a charged sample species of interest mixed with a low mobility terminating electrolyte (TE), which exhibits a lower electrophoretic mobility relative to the charged target sample analytes. The mixture comprised of TE and sample are then driven continuously down a microfluidic channel that has been fabricated to include a pair of electrically conductive, yet mass-impermeable side-wall polymeric electrode membranes. The microfluidic flow field is then exposed to a perpendicular external electric field in order to drive the electromigration of the TE and sample mixture analytes into the no-flux boundary defined by the channel conductive side wall. Similar to ITP, the relatively higher mobility sample species of interest stacks against the wall and forms a sample enrichment zone that expands as the sample flows axially downstream while

simultaneously, the lower mobility TE ion trails behind and stacks against the sample enrichment zone. Such stacking creates an enhanced electric field zone and a corresponding sharpening within the sample enrichment zone in a concentration mechanism similar to that of isotachophoresis (ITP); however, the use of an LE is not required due to the presence of the conductive wall. TPE features high separation resolutions and preconcentration factors as large as 60,000-fold. Furthermore, TPE is a continuous, free-flow process, requires a low 10 VDC potential, and improves upon the throughput and scalability of electrokinetic sample preparation systems.[10]

While TPE shows promise as an effective concentration and separation method, thus far it has only been formally demonstrated for concentrating and separating charged molecular fluorescent dyes (Alexa 594, Alexa 488, and fluorescein). Before TPE can be effectively applied to POC diagnostic problems, its compatibility with biomolecules, such as nucleic acids and proteins, must be explored. Specifically, problems may arise when performing TPE with proteins, such as precipitation due to increased concentration when approaching protein solubility limits, protein-protein interactions during electric field exposure, and pH changes that could arise from water electrolysis, all of which can influence protein stability.[111–113] Therefore, in this work, we investigate the use of TPE with aqueous solutions of biomolecules by performing TPE concentration and separation experiments using solutions of both proteins and nucleic acids. We first investigate the concentration of a model fluorescently tagged protein, avidin-FITC. We then directly compare the effectiveness of TPE on a protein sample both in the presence and absence of the high electric field zone induced by the presence of a TE. We next characterize the TPE protein concentration factor and the width of the TPE protein concentration

depletion zone as a function of applied voltage and microchannel flow rate to demonstrate the linear electrophoretic nature of the observed TPE method.[10] We then conclude our TPE protein investigation by demonstrating its use to separate a known mixture of the fluorescently tagged proteins, bovine serum albumin tagged to AlexaFluor 555 (BSA-AlexaFluor 555) and ovalbumin tagged to fluorescein (ovalbumin-fluorescein). Finally, we present our TPE concentration results using nucleic acid two DNA samples containing different base pair lengths and demonstrate the ability to concentrate nucleic acids using a TE with TPE.

3.3. Materials and Methods

All chemicals used in this work were purchased from Millipore-Sigma unless otherwise stated. Fluorescein isothiocyanate (FITC) conjugated to avidin, fluorescein conjugated to ovalbumin, and AlexaFluor 555 conjugated to bovine serum albumin (BSA) were purchased from Thermo-Fisher Scientific. Two DNA sequences of two different base pair (bp) lengths, Test Sequence 1 (TS1), 90-bp & Test Sequence 2 (TS2), 45-bp were randomly generated and ordered from Integrated DNA Technologies. Nucleic acid sequence information can be found in Table 3.1. Each nucleic acid sequence was imaged using the intercalating dye, SYBR Green I, which was ordered from Invitrogen. Multiwalled 20–30 μm length carbon nanotubes were purchased from Cheap Tubes (030104). Polydimethylsiloxane (PDMS) and PDMS crosslinking agent were purchased from Momentive (RTV 615A). Due to its low electrophoretic mobility relative to other species in solution, 4-(2-hydroxyethyl)-1-piperazineethanesulfonic acid (HEPES) was chosen as the TE for these experiments.

Table 3.1 Randomly generated DNA sequence information. Reprinted with permission from Doria et al. *Talanta* **2023**, *255*, 124198. Copyright 2023 Elsevier.[11]

Sequence Name	Forward Sequence (5' -> 3')	Reverse Sequence (5' -> 3')	Length	GC Content
Test Sequence #1	GTAGCTCTTCGTTCCGTCAAGGCC CGACTTTCATCGCGGCCCATTCCA TGCGCGGACCATACCGTCCTAATT CTTCGGTTATGTTTCCGA	TCGGAAACATAACCGAAGAATTAG GACGGTATGGTCCGCGCATGGAATG GGCCGCGATGAAAGTCGGGCCTTG ACGGAACGAAGAGCTAC	90 bp	54%
Test Sequence #2	ATGATAGGAATTTGCGTATAGAGC GTGTCATTGAGGGCTTATACA	TGTATAAGCCCTCAATGACACGCTC TATACGCAAATTCCTATCAT	45 bp	40%

3.3.1. Device Fabrication

FFTPE devices were constructed from polydimethylsiloxane (PDMS) and consisted of a main flow channel with a pair of conductive sidewall polymeric membrane electrodes. Each sidewall electrode served as both the source of the electric field and a no-flux conductive barrier for TPE concentration and separation. The membranes themselves were patterned and fabricated using a multi-step soft lithography technique that we have reported previously.[10,55] Briefly, we fabricated a thick film microchannel mold using a negative SU-8 3050 photoresist (Kayaku Advanced Materials). The mold consisted of a main microfluidic flow channel and two side channels situated in parallel, each separated by a 100 μm gap. Each gap was then filled with a 5 wt% mixture of multiwalled 20–30 nm OD, 20–30 μm length carbon nanotubes (CNTs) mixed with PDMS elastomer without curing agent. The mold was then immediately covered with a 10:1 mixture of PDMS elastomer and curing agent and baked at 85 °C for 2 h. The fully cured PDMS slab was gently peeled off the mold, which released the now cured conductive PDMS/CNT composite within the microchannel and created a main flow channel with two conductive sidewall membranes. Inlet and outlet ports were punched into the PDMS slab using a 0.75 mm biopsy punch (Ted Pella, Inc). Finally, each device was exposed to oxygen plasma

(Jetlight, Model 42A) for 2 min, and then immediately bonded to a 1 mm-thick glass coverslip (75 mm × 25 mm × 1 mm, VWR 16004–422). Each resulting device consisted of a main flow channel, 4 mm in length, 500 μm in width, and 50 μm in height with one inlet and three outlets (Figure 3.1(a)). The red dotted region of interest highlighted in Figure 3.1 represents the approximate fluorescent analysis zone presented in Figures 3.2, 3.4, and 3.5. Each sidewall membrane was 100 μm in thickness, and separated the main flow channel from a pair of solid gallium metal leads (Sigma, 77631) as shown in Figure 3.1(b). Each gallium lead was injection molded against the backside of each sidewall membrane through an adjacent pair of microchannels situated in parallel to the main flow channel. The polymer membrane-lead separation helped to prevent Faradaic electrolysis reactions that can more readily occur between the direct contact between a conductive buffer and a solid metal electrode. After device fabrication and gallium injection, 21-gauge solid copper wire posts (diameter = 0.75 mm, length = 2.5 cm, Arcor Electronics) were then inserted into gallium injection holes, which served as lead connection points to an external power source. Gallium was chosen for its low melting point, as it could be readily melted and injected against each sidewall membrane. To fabricate gallium leads, the PDMS device was placed on a 40 °C hotplate and gallium metal was melted and injected as a liquid metal into the two parallel side channels. After cooling, these solid metal-filled channels served as both electrical connections and structural supports for the conductive PDMS/CNT nanocomposite sidewall membranes.

3.3.2. Device Operation

Fluid flow was driven continuously down the main flow channel at a constant flow rate using a syringe pump (Cole-Parmer 78–8200C). During each flow experiment,

an electric field was driven across the flow channel using a 10 V pulsed DC (PDC) potential applied perpendicular to flow direction using the two conductive sidewall membrane electrodes. This positive-pulsed waveform was delivered using a function generator (Rigol DG1022Z) and served to significantly reduce Faradaic reactions and water electrolysis in the main flow channel, while still providing a potential difference across the channel to drive electromigration. Unlike similar microchannel-based electrophoresis methods, such as ITP, which typically uses a constant high voltage (>600 V DC) potential and vents the resulting gaseous electrolysis byproducts from the device via the microchannel inlets and outlets, a PDC-driven electric field can be integrated directly within a main flow channel without requiring inlet/outlet gaseous venting. The PDC waveform consisted of a pulsed positive square wave, originating from 0 V, and stepping up to a fixed value of up to 10 V at 1 kHz frequency with a duty cycle of 80%. For protein separation experiments, however, we utilized a PDC frequency of 21 kHz as this was observed to minimize protein aggregation. As we have reported previously, the on-off pulsation periods of the PDC electric field serve to prevent electrolysis products from nucleating, while still providing field conditions for electrophoresis because the electric field switches on and off at a time scale shorter than what is required to drive observable nucleation. Using this PDC field we do not observe any bubble generation or measurable pH change when working with fluorescent dyes.[10,55] In this work, only a minor ~3% deviation in sample pH was observed with protein solutions, which we will present in a later section of this work. Without this pulsed field, electrolysis products are observed to nucleate at the sidewalls of the device

in the form of gaseous bubbles, which can influence the sample pH and biomolecular electrophoretic mobility, clog microchannels, and impede device performance.

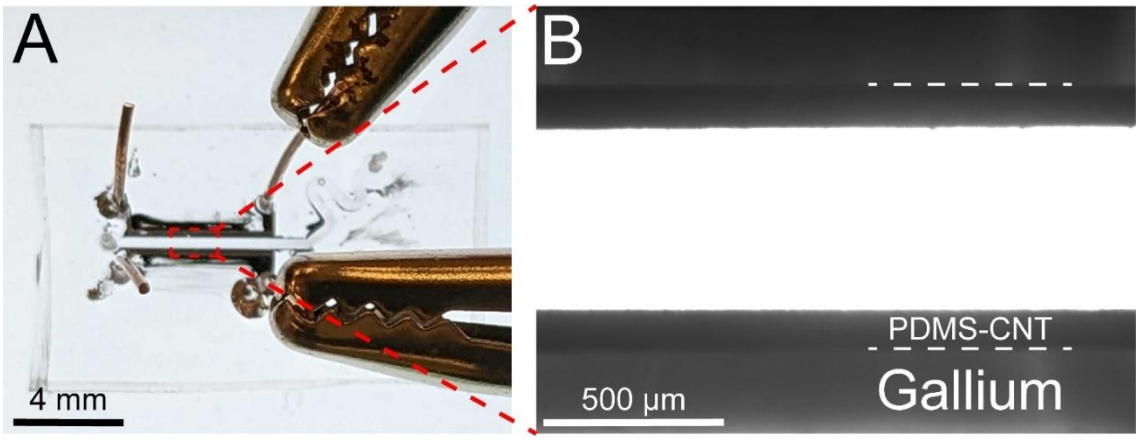

Figure 3.1 Teíchophoresis device overview. (a) A PDMS microchannel device with conductive wall sidewall membranes. (b) Close view of the microchannel, with sidewalls made from a conductive PDMS-CNT membrane and a solid gallium electrode. Reprinted with permission from Doria et al. *Talanta* **2023**, *255*, 124198. Copyright 2023 Elsevier.[11]

TPE was performed on solutions containing both proteins and nucleic acids. For protein-based TPE it was necessary to first passivate the microchannel in order to prevent unwanted protein sample adsorption on the microchannel surfaces. Therefore, prior to protein TPE experiments an aqueous solution of 3% w/v BSA was flowed into the device, incubated for 10 min, and then subsequently rinsed with deionized water to prevent non-specific binding to the glass and PDMS channel surfaces. To re-use devices for multiple experiments and to prevent sample cross-contamination, devices were cleaned by flowing a solution of 5 N NaOH through the main flow channel, followed by a rinse with deionized water, and then re-blocked with a 3% w/v BSA prior to any further protein experiments. No BSA blocking of the device was necessary for the nucleic acid-based TPE experiments. To drive the TPE electric field, experiments were

performed at either a constant 10 V PDC potential or over a range of PDC voltage, varying between 0 and 10 V PDC in order to characterize the TPE biomolecule concentration behavior as a function of voltage.

This work focused solely on investigating biomolecular concentration and separation using plateau mode TPE. Similar to that of plateau mode ITP, in plateau mode TPE the initial sample concentrations do not differ significantly in orders of magnitude to that of the TE concentration. The single-species protein TPE experiments were performed with a 500 nM concentration of avidin-FITC mixed with 40 μM of the TE, HEPES. For the case where no TE was present, a 500 nM solution of avidin-FITC in deionized water was used for single-species protein experiments. For multi-species protein experiments, we combined 1 μM of ovalbumin-fluorescein with 1 μM of BSA-AlexaFluor 555 with 100 nM of HEPES. Finally, for plateau mode DNA-based TPE experiments in presence of a TE, a 500 nM concentration of TS1 was mixed with 40 μM of HEPES and 1x SYBR Green I. Separate mixtures of 500 nM TS2 were also combined with 40 μM of HEPES and 1x SYBR Green I. DNA experiments without a TE replaced HEPES with deionized water but retained 1x SYBR Green I. Conductivity & pH information for TPE samples mixtures can be found in Table 3.2.

Table 3.2 Conductivity and pH information for TPE mixes. Reprinted with permission from Doria et al. *Talanta* **2023**, *255*, 124198. Copyright 2023 Elsevier.[11]

Mix	Figure	Conductivity (μS/cm)	pH
500 nM Avidin-FITC	Figure 3.2(a), 3.2(b)	100.0 ± 2.9	6.43 ± 0.05
500 nM Avidin-FITC, 40 μM HEPES	Figure 3.2(c), Figure 3.3	126.7 ± 0.5	6.37 ± 0.05
1 μM BSA-AlexaFluor 555, 1 μM Ovalbumin-fluorescein, 100 nM HEPES	Figure 3.4	1.0 ± 0.0	5.57 ± 0.21
500 nM DNA, 1x SYBR Green I	Figure 3.5(a), Figure 3.5(b)	24.3 ± 0.5	5.80 ± 0.08
500 nM DNA, 40 μM HEPES, 1x SYBR Green I	Figure 3.5(c), Figure 3.6	21.3 ± 0.5	5.80 ± 0.08

To quantify both protein and DNA concentration, the fluorescent intensity of known protein concentration standards and DNA concentration standards were determined and calibrated under swept-field confocal microscopy. Calibration curves for avidin-FITC, TS1, and TS2 were generated in a similar manner as reported previously and can be found in Appendix A.[10] Fluorescent intensities and fluorescent images were taken using an inverted swept field confocal microscope (Nikon Eclipse Ti, 70 μm confocal slit, Nikon/Prairie Technologies), an Andor iXon 897 EMCCD camera, a 50-mW solid state laser for excitation, and a 4× objective.

3.4. Results and Discussion

3.4.1. Protein Concentration

We first investigated the ability to concentrate protein solutions by TPE both in the presence and absence of a TE. Specifically, a 500 nM solution of avidin-FITC with TE was driven down the main flow channel at a flow rate of 5 μL/min (Figure 3.2(a)). We induced electrophoretic migration perpendicular to the direction of flow of avidin-FITC by applying a 10 V PDC potential with an 80% duty across the main flow channel

at a pulse frequency of 1 kHz. In the presence of this pulsed field, we observed that the net positively charged protein electromigrated across the channel and towards the negative electrode and accumulated at the conductive wall as shown in the micrograph and corresponding fluorescent intensity profile (Figure 3.2(b)). Next, we repeated this experiment with a 40 μM concentration of TE. Once again, we observed that the pulsed field induced the protein to electromigrate to the negative electrode, however, in the presence of the TE (HEPES), we observed a sharper, more intense sample enrichment zone (Figure 3.2(c)). Experiments in this work shared a concentration saturation time scale on the order of 5 s (Figures 3.2, 3.4, and 3.5).

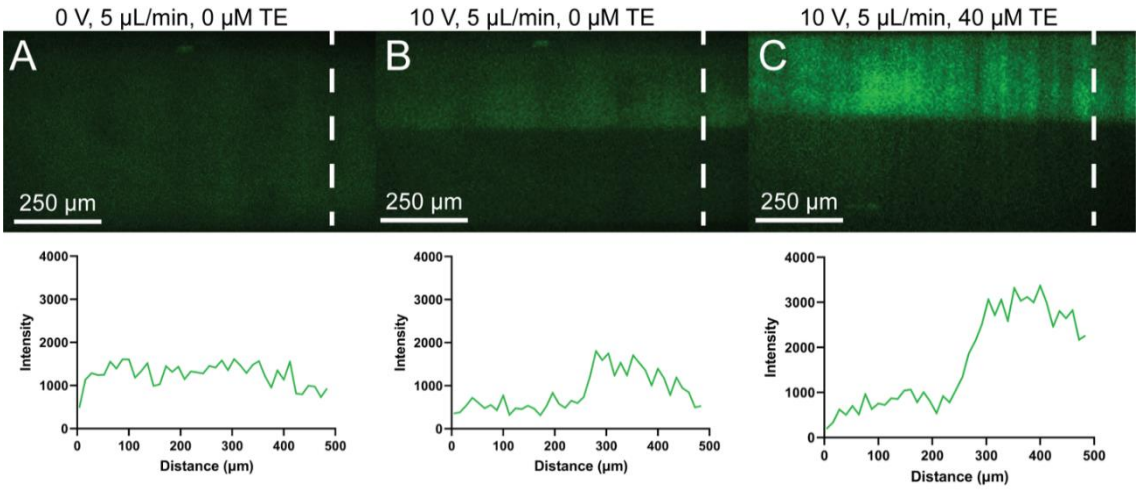

Figure 3.2 Plateau mode FFTPE of avidin-FITC. (a) Avidin-FITC flowing in a uniform concentration through the main flow channel; no electric field. (b) A 10V PDC electric field is applied across the channel in the absence of TE initiates protein concentration towards the positive electrode near the wall in the absence of TE. (c) Concentration at the conductive wall in the presence of TE. There is a clear amplification in protein concentration in the presence of TE. All fluorescent intensity plots were generated using fluorescent intensities measured along the dashed line (a, b, and c). Reprinted with permission from Doria et al. *Talanta* **2023**, *255*, 124198. Copyright 2023 Elsevier.[11]

In order to quantify the degree of avidin-FITC concentration, we correlated the peak measured fluorescent intensity to known protein concentration standards and

developed an avidin-FITC concentration calibration curve (Figure A1). Using this curve, we computed the TPE-driven concentration factor, $CF = \frac{[\text{Avidin}]_{\text{final}}}{[\text{Avidin}]_{\text{initial}}}$, by comparing the initial known concentration to the measured concentration/intensity relationship. For the avidin-FITC, we observed a CF of 1.4 in the absence of TE, and a CF of 6.6 in the presence of TE. Therefore, the presence of 40 μM HEPES enhanced avidin-FITC concentration by a factor of 4.7 relative to the concentration factor observed in the absence of TE.

3.4.2. Linearity of TPE Protein Concentration and Depletion

In order to investigate the electrophoretic linearity of protein TPE with respect to both flow rate and applied voltage, we investigated the influence of PDC voltage and flow rate on the resulting TPE concentration of avidin-FITC. Such an experiment is important part of this analysis as it could elucidate any changes in electrophoretic mobility during the device operation due to potential pH changes associated with the embedded electrodes. In order to investigate this experimentally, we measured the concentration factor of 500 nM avidin-FITC with 40 μM HEPES as a function of PDC voltage (0–10 V) and flow rate (5–20 μL/min). We then plotted the resulting concentration factor versus the voltage (V) scaled by the applied flow rate (Q). As we have previously reported, we observe a consistent screening potential of 2.4 V PDC in our TPE devices, below which no electromigration is observed.[10] Therefore, we scaled the effective voltage as follows: $V_{eff} = V - V_{screen}$, where V_{eff} is the effective electric potential, V is the applied electric potential, and V_{screen} is the measured device screening potential. As expected, for a linear free-flow electrophoretic phenomenon with constant electrophoretic mobility we observe a linear dependence between the concentration

factor and ratio of voltage-to-flowrate (V/Q) (Figure 3.3(a)). Furthermore, we also characterized the concentration rate by measuring the width of the protein-depleted zone within the channel over the same variation in voltage and flowrate to further investigate the linearity in the observed TPE-driven protein electromigration flux across the channel. To determine the width of this zone we captured fluorescent micrographs over a range of experimental voltages (0 – 10 V) and flow rates (5 – 20 μL/min), generating an experimental matrix of effective voltage-to-flowrate ratios. Additionally, we quantified the fluorescent intensity profile of avidin-FITC across the width of the microchannel. Fig. 3.2 and Figure 3.3 were each generated using a freshly fabricated device, so variations in the fabrication process between devices likely led to a difference between the concentration factors reported in these figures. We then determined the position across the channel width where the concentration zone intensity dropped below the average fluorescent intensity of the concentration profile. The width of the protein-depleted zone was then computed as the distance between the opposing electrode wall and this location. We present this distance as the fraction of the channel, referred to as the protein-depleted zone, as a function of the voltage-to-flowrate ratio (Figure 3.3(b)), and again observe that the width of the protein-depleted zone scales linearly with the applied voltage-to-flowrate ratio (V/Q), further demonstrating that protein mobility is observed to remain constant over the free-flow experimental domain.

Overall, in terms of TPE-driven protein concentration, we observe a concentration increase of 6x the initial protein concentration under a 10 V PDC electric field in the presence of a TE, demonstrating the potential that preconcentration by TPE in a pulsed electric field is biocompatible with proteins. We also observe a maximum

protein-depleted zone at 10 V PDC comprising of 58% the microchannel width. Furthermore, the linear response in both concentration and depletion zone with the applied voltage demonstrates that pH remains largely unchanged during pulsed-field TPE, as any systemic change in pH during TPE would alter the effective mobility of the protein, leading to a non-linear response in the concentration and depletion zones with applied voltage.

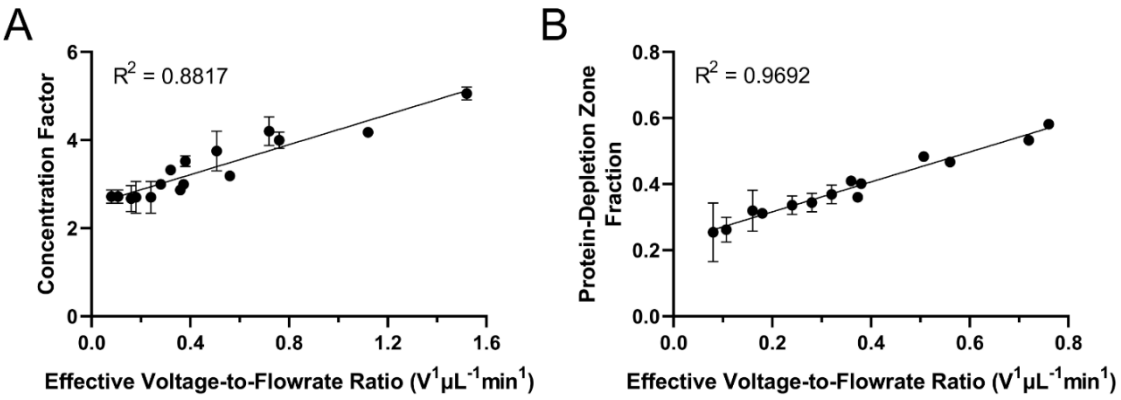

Figure 3.3 FFTPE Linearity of avidin-FITC. (a) Concentration factor as a function of the voltage-to-flowrate ratio in FFTPE. We observe that the concentration factor increases linearly with voltage-to-flowrate ratio (R^2 = 0.8817). (b) Width of the protein-depleted zone as a function of the voltage-to-flowrate ratio in FFTPE. We observe that the width of this depleted protein zone increases linearly with voltage-to-flowrate ratio (R^2 = 0.9692). Reprinted with permission from Doria et al. *Talanta* **2023**, *255*, 124198. Copyright 2023 Elsevier.[11]

3.4.3. Protein Separation

Finally, we investigated TPE's ability to perform on-chip, free-flow, protein separation. A solution of 1 μM of ovalbumin-fluorescein (OVB), 1 μM of BSA-AlexaFluor 555, and 100 nM HEPES (TE) was flowed continuously through the microchannel at a flow rate of 2 μL/min (Figure 3.4(a)). It is important to note that protein separation performance was much more sensitive to the TE concentration than compared to our previously published work with fluorescent dye.[10] For protein

separation, we selected a reduced flow rate to increase the residence time of the protein within the device to improve separation resolution. In the presence of 40 μM HEPES TPE concentration was too intense and we observed that both BSA and OVB concentrated into the same enrichment zone, inducing protein aggregation, preventing separation. However, as expected in the absence of TE no concentration was observed. Therefore, we used a low TE concentration of 100 nM HEPES in our separation experiments in order to reduce protein aggregation. TPE separation was initiated by dropping a 21 kHz, 10 V PDC potential with an 80% duty cycle across the microchannel. During application of the electric field the ovalbumin and BSA were observed to electrophoretically stack against the conductive wall and then separate in decreasing order according to their relative electrophoretic mobilities. The resulting fluorescent intensity profile depicts a clear separation and increased concentration of the two proteins (Figure 3.4(b)). It is worth noting that previously published work by Zhao et al. observed that disulfide bonds between cysteine residues can develop between BSA and ovalbumin, leading to aggregation when subjected to a pulsed electric field.[111] This phenomenon could lead to the observed banding of BSA-AlexaFluor 555 (in Red), seen in Figure 4B. Protein aggregation due to a pulsed electric field was not observed in our single species experiments with avidin-FITC (Figure 3.2) further suggesting that banding is unique to the OVB/BSA pairing. Nonetheless, Figure 3.4(b) clearly demonstrates separation of BSA and ovalbumin. Further, no protein separation was observed in the absence of a TE. This binary protein species separation demonstrates that TPE has the potential to serve as an upstream sample preparation technique compatible with multi-protein systems.

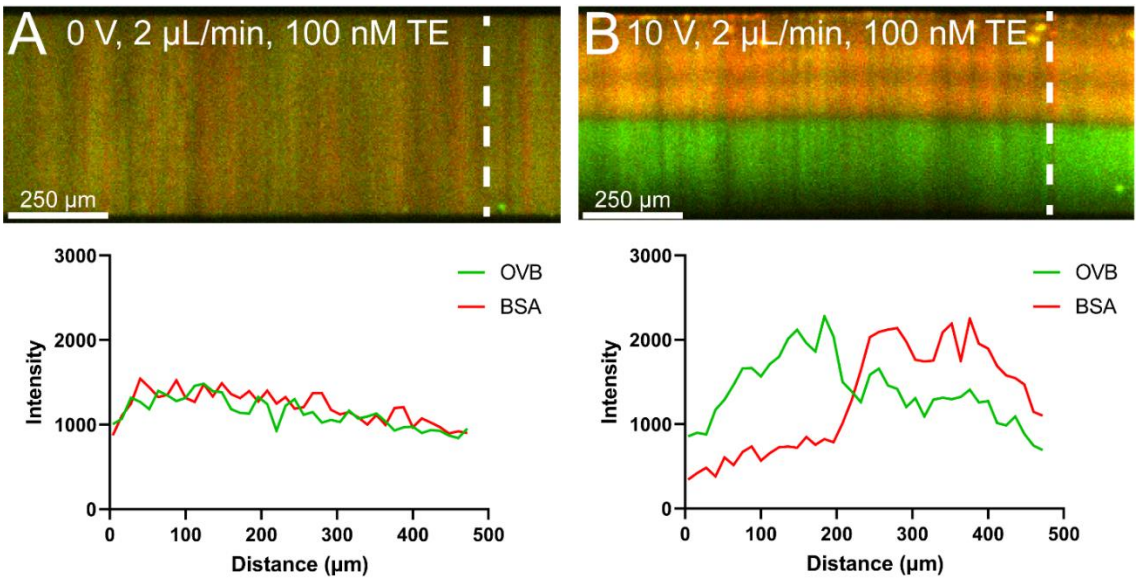

Figure 3.4 FFTPE separation of BSA and Ovalbumin. (a) Confocal microscopy image of BSA-AlexaFluor 555 & ovalbumin-fluorescein mixture in the absence of an electric field. (b) Confocal microscopy image of BSA & ovalbumin separation using TPE. All fluorescent intensity plots were generated using fluorescent intensities measured along the dashed line (a and b). Reprinted with permission from Doria et al. *Talanta* **2023**, *255*, 124198. Copyright 2023 Elsevier.[11]

3.4.4. DNA Concentration

In this work we also sought to investigate the compatibility of TPE with nucleic acids, as we hypothesized that TPE can also leverage the same no-flux boundary paired with a low mobility terminating electrolyte to concentrate DNA. In DNA-based TPE, we flowed two different nucleic acid test sequences of differing lengths (Table 3.1) mixed with a TE through our main flow channel. We investigated the ability to concentrate DNA by TPE both in the presence and absence of a TE. Specifically, a 500 nM solution of 90-bp DNA (TS1) intercalated with 1x SYBR Green I was driven down the channel at 5 µL/min (Figure 3.5(a)). We induced electrophoretic motion without a TE by applying a 1 kHz, 6 V pulsed-DC potential with an 80% duty across the main flow channel. In the presence of this pulsed field, we observed that the negatively charged DNA electromigrated to the positive polarized electrode and measured the fluorescent

intensity of the SYBR-intercalated DNA across the length of the flow channel (Figure 3.5(b)). Next, we mixed 500 nM of TS1 with 40 µM HEPES and drove this solution down the main flow channel at 5 µL/min, and applied a 1 kHz, 6 V PDC potential. Once again, we observed that the pulsed field induced electromigration of the SYBR-intercalated DNA, but in presence of the TE, we observe a sharper, more intense sample enrichment zone (Figure 3.5(c)).

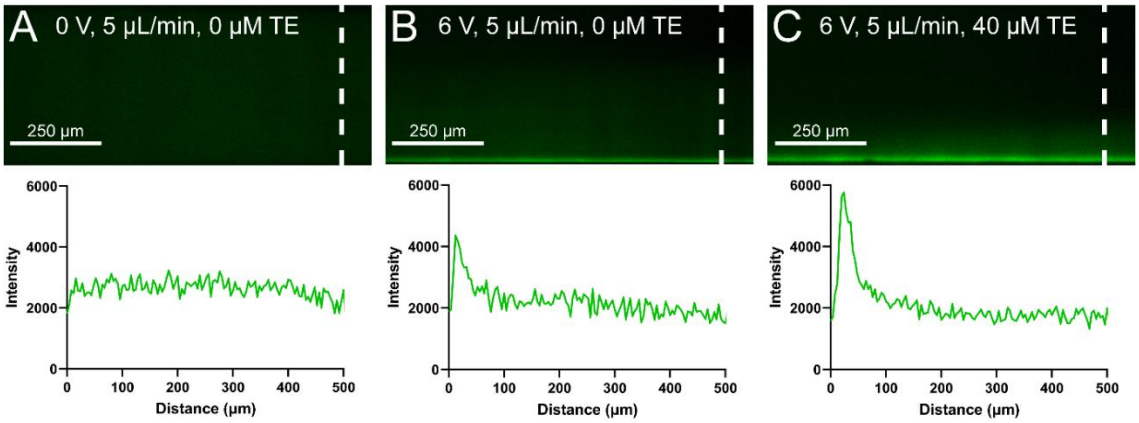

Figure 3.5 Plateau mode FFTPE of SYBR-intercalated DNA (TS1). (a) DNA flowing in a uniform concentration through the main flow channel. (b) A 6V pulsed field is applied across the channel, initiating electromigration of the DNA, in the absence of TE, towards the positive electrode. (c) Concentration at the conductive wall in the presence of TE. Comparing the micrographs of b and c shows a clear concentration increase in the presence of TE. All fluorescent intensity plots were generated using fluorescent intensities measured along the dashed line (a, b, and c). Reprinted with permission from Doria et al. *Talanta* **2023**, *255*, 124198. Copyright 2023 Elsevier.[11]

We developed an intensity-to-concentration calibration curve, analogous to our protein intensity-to-concentration calibration curve, for TS1 & TS2 (Figure A2 and Figure A3, respectively) and characterized the TPE-driven concentration factors, as shown in Figure 3.5(b) and Figure 3.5(c) for the TS1 sample. We observed CF of 5.9 in the absence of TE, and a CF of 9.0 in the presence of TE at 6V PDC (Figure 3.5).

Therefore, the presence of 40 μM HEPES enhanced DNA concentration by a factor of 1.5.

3.4.5. DNA Concentration Factor with Voltage, Flowrate, and Sequence Length

Finally, we investigated voltage and sequence length dynamics on concentration of DNA. Specifically, we measured the concentration factor of 500 nM DNA mixed with 40 μM HEPES as a function of voltage (0–10 V) and sequence length (TS1 – 90-bp, TS2 – 45-bp). Final concentrations were measured using the previously mentioned intensity-to-concentration calibration curves. Similar to the concentration dynamics of protein in TPE, we observed an approximately linear dependence of concentration factor on voltage (Figure 3.6(a)). Such linearity is expected due to the nature of the field-driven electrophoresis across the channel. Furthermore, we observed an inverse relationship between DNA sequence length and concentration factor; we normalized the applied voltage with respect to the DNA sequence length and found that both sets of data collapsed to a singular, linear relationship (Figure 3.6(b)). This is expected as diffusivity of DNA scales inversely with sequence length, which according to Einstein's relationship between electrophoretic mobility and diffusivity, implies that electrophoretic mobility scales inversely with sequence length.[114,115] Here we observe that we achieve a maximum concentration of 21 times the initial concentration of DNA under a 10 V pulsed electric field, confirming that TPE is biocompatible with DNA. Furthermore, the inverse dependence of concentration factor to sequence length implies that TPE could be used to estimate lengths of unknown DNA sequences. This 21-fold concentration factor was accomplished continuously using only 10 V PDC, compared to previous batch ITP work performed by Wang et al. which achieved a 60-fold DNA

concentration factor using a significantly higher 450 V DC potential.[109] Furthermore, the buffers employed in this work were on the order of 20 mM, which are significantly higher than the concentrations required for TPE.

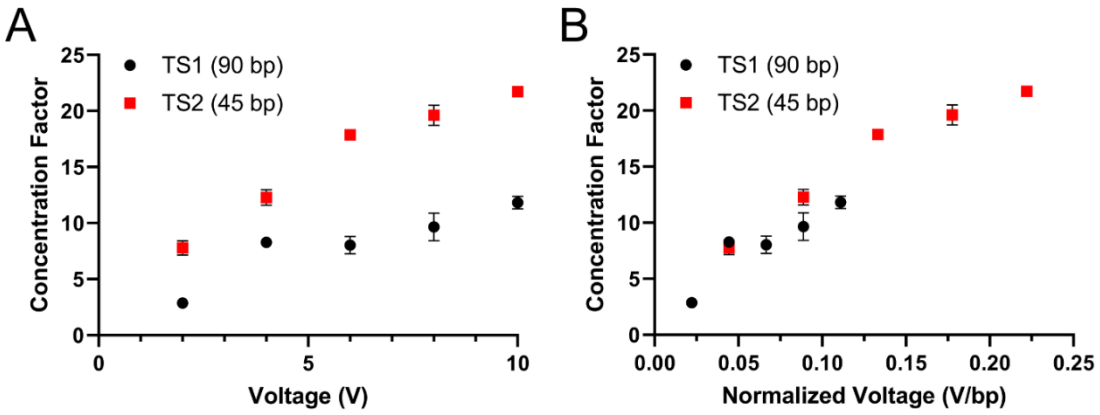

Figure 3.6 FFTPE Linearity of DNA (TS1 and TS2). (a) Concentration factor as a function of voltage in FFTPE for two different DNA sequence lengths. We observe that the concentration factor increases linearly with voltage and inversely with sequence length (R^2 (TS1) = 0.8512, R^2 (TS2) = 0.9493). (b) Concentration factor as a function of normalized voltage. Voltage was normalized with respect to DNA strand length by dividing voltage by number of base pairs. We observed that both sets of data can be expressed by a single curve when voltage is normalized to DNA strand length. Reprinted with permission from Doria et al. *Talanta* **2023**, *255*, 124198. Copyright 2023 Elsevier.[11]

3.5. Conclusions

In this work, we have demonstrated the molecular biocompatibility of TPE, an electrophoretic technique capable of sample preconcentration, separation, and purification, with both proteins and nucleic acids. Previous attempts at characterizing TPE have been limited to robust samples, such as the AlexaFluor series of dyes, which unlike many biomolecules, benefit from relatively high solubility limits and an insensitivity to pH changes.[116] Using a pulsed DC electric field, we performed TPE continuously within a microchannel on both solutions of proteins and DNA across a diverse set of experimental voltages and flow rates. We observed that employing a

pulsed electric field mitigates pH changes associated with Faradaic reactions, which in turn likely contribute to the ability to utilize TPE for biomolecular concentration and separation. We investigated the ability to concentrate the protein, avidin-FITC, and showed that, in the presence of a 10 V PDC field, avidin-FITC concentration increased by a factor of 1.4 times in the absence of TE, and increased 6.6-fold in the presence of TE. Therefore, the presence of 40 μM HEPES was observed to amplify the concentration factor by 4.7-fold. We then investigated the influence of the device flowrate and voltage on the resulting protein concentration factors in the TPE enrichment zone, and on the width of the protein depletion zone. Our results showed that both the concentration factor and the width of the protein-depleted zone responded linearly to the voltage-to-flowrate ratio (V/Q). These findings can be used to tune overall throughput and relative location of sample-enriched and sample-depleted zones in future experiments, and further suggest that protein electrophoretic mobility is not influenced by any potential pH changes associated with electrode-driven Faradaic reactions. Next, we demonstrated the ability to use TPE to separate proteins using a binary mixture of BSA and ovalbumin. Finally, we investigated the ability to concentrate DNA using TPE and observed a 21-fold increase in DNA concentration using only 10 V PDC. Furthermore, we investigated the concentration dependence with applied voltage for two different DNA base pair lengths (45 bp and 90 bp) and observed that the resulting concentration/voltage dependence scales inversely with DNA base pair length. Overall, we have demonstrated the ability to use TPE to concentrate and separate biomolecules in a manner similar to that of ITP, but using only a TE and a conductive wall. In conclusion, this work demonstrates that TPE has the potential to be utilized as a rapid

and continuous upstream sample preparation method for solutions containing both proteins and DNA due to its simplified electrolyte and fluidic requirements, increased sample throughput, scalability, and reduced electric potential requirements.

Section 3 presented a novel way to prepare samples for diagnostics by enabling continuous NAA inhibitor removal from biological samples, TPE. Additionally, TPE also concentrated nucleic acids, potentially allowing for faster amplification times and decreasing time-to-result for diagnostics. The next step in the microfluidic diagnostic process is to detect nucleic acid biomarkers in our now-prepared samples. This is typically done using a nucleic acid amplification technique, the most common ones being PCR and LAMP. However, there are some inherent challenges to microfluidic NAA such as thermal gradients within the reaction and requiring bulky heaters to be attached to microfluidic NAA devices. Section 4 expands upon these drawbacks and proposes a novel heating method, Electrokinetic Nucleic Acid Amplification (E-NAAMP) to overcome these drawbacks by utilizing a high-frequency voltage to generate Joule heating directly within the reaction.

4. FARADAIC-FREE ELECTROKINETIC NUCLEIC ACID AMPLIFICATION (E-NAAMP) USING LOCALIZED ON-CHIP HIGH FREQUENCY JOULE HEATING*

4.1. Overview

We present a novel Faradaic reaction-free nucleic acid amplification (NAA) method for use with microscale liquid samples. Unlike previous Joule heating methods where the electrodes produce electrolysis gaseous by-products and require both the electrodes be isolated from a sample and the venting of produced electrolysis gas, our electrokinetic Nucleic Acid Amplification (E-NAAMP) method alleviates these issues using a radio frequency (RF) alternating current electric field. In this approach, a pair of microscale thin film gold electrodes are placed directly in contact with a nucleic acid reaction mixture. A high frequency (10 – 40 MHz) RF potential is then applied across the electrode pair to induce a local Ohmic current within the sample and drive the sample temperature to increase by Joule heating. The temperature increase is sustainable in that it can be generated for several hours of constant use without generating any pH change to the buffer or any microscopically observable gaseous electrolysis by-products. Using this RF Joule heating approach, we demonstrate successful direct thermal amplification using two popular NAA biochemical reactions: loop-mediated isothermal amplification and polymerase chain reaction. Our results demonstrate that a simple microscale electrode structure can be used for thermal regulation for NAA reactions without observable electrolytic reactions, minimal enzyme activity loss and sustained

* – Adapted with modifications from Yost, J.; Gagnon, Z. Faradaic-Free Electrokinetic Nucleic Acid Amplification (E-NAAMP) Using Localized on-Chip High Frequency Joule Heating. *Biomicrofluidics* 2022, *16* (1), 014101, with the permission of AIP Publishing

(>50 h use per device) continuous operations without electrode delamination. As such, E-NAAMP offers substantial miniaturization of the heating elements for use in microfluidic or miniaturized NAA reaction systems.

4.2. Introduction

With an increase in demand for on-site decentralized nucleic acid testing of infectious disease, significant efforts have been made to develop novel and low-cost miniaturized systems to detect target nucleic acid (NA) biomarkers in complex samples, including whole blood, serum, urine, and saliva using molecular amplification.[5,117] One way to amplify target NA sequences is to use polymerase chain reaction (PCR). Invented in 1983 by Kary Mullis, PCR has been used for amplifying and detecting specific sequences from a variety of pathogenic targets, including Escherichia coli, Salmonella, Staphylococcus aureus, and viruses such as influenza and SARS-CoV-2.[64,118–121] With the onset of world pandemic-level infections, there is a significantly increased need and demand for technologies capable of enabling decentralized "at-home" nucleic acid amplification (NAA) tests. Conventional NAA approaches that utilize expensive laboratory-scale thermal cyclers with large thermal blocks are limited in their ability to be miniaturized and manufactured at scales large enough for global individual use.[9] At the time of this publication, a significant number of NAA tests have been authorized for emergency use by the Food and Drug Administration (FDA) under an Emergency Use Authorization.[122–124] The majority, however, still require the transport of the sample to a centralized facility for NAA and analysis. Several tests by Lucira or Abbot offer the ability to perform NAA on-site without sample transport; however, they still rely on the use of bulky external heating elements, which increases

the testing footprint, price per assay, and the large amount of electronic waste (E-waste) associated with these single-use tests.[125,126] While the pace of development and deployment of such tests has been significant, the ability to screen a global population rapidly and without the use of centralized facilities has yet to be perfected.

One such way to miniaturize NAA is to use microfluidics. Unlike the laboratory thermal cycler with a large thermal mass, microfluidic-based thermal cycling is based on heating microscale reaction volumes in either a batch or continuous operation. In continuous flow, a microfluidic sample is driven continuously through different temperature regulated thermal zones through a series of thermal serpentine turns, where the number of channel serpentines equates to the number of PCR cycles. PCR temperature cycling can then be achieved by pumping fluid cyclically between each thermally controlled fluidic zone with PCR-specific denaturing, annealing, and extension temperatures.[70]

An alternative microfluidic NAA approach utilizes batch operated fluid-filled microscale chambers with time-varying boundary-laden resistive heating elements. The stationary reaction designs are similar to a traditional thermal cycler system: a NA sample is contained in a fixed microscale well and heated with an external resistive heater fixed underneath the reaction chamber and thermally cycled between the PCR denaturing, annealing, and extension temperatures.[64,118]

While microfluidic PCR methods are effective, they typically use bulky external heating elements located outside the reaction chamber which places physical constraints on NAA test portability, production cost, and E-waste generation.[68–70] One alternative method for NAA thermal cycling is to utilize Joule heating as a substitute for an external

heating element. In this approach, the conductive nature of a NA sample can be used to generate resistive heat when this liquid is exposed to an external electric current via a pair of polarized electrodes. Using the conductive buffer itself eliminates the need for bulky, external heaters attached to microfluidic NAA devices. Conductive PCR mixtures have been thermally cycled using both direct current (DC) Joule heating and low frequency (60 Hz) alternating current (AC) sources. Successful Joule heating amplification have been demonstrated, but the device electrodes were not in direct contact with the reaction volume because they required venting of electrochemical reaction by-products due to the electrolysis that occurred at the anode and cathode electrodes. While previous Joule heating work suggests that an electrical current can be used to drive biochemical reactions in conductive liquid samples,[71,127] the electrolytic by-products severely restrict the use of these methods in closed microfluidic systems and miniaturized NAA tests.

In this work, we present a novel radio frequency (RF) electrokinetic Joule heating method for direct heating and thermal cycling of NA samples without electrode isolation and electrochemical venting within a microscale fluid sample volume. We utilize a high (10 – 40 MHz) RF voltage to drive a high RF Joule heating current directly to the conductive NA sample. The current is delivered using an AC (10 – 30 V_{pp}) potential dropped across a pair of thin film co-planar microelectrodes fabricated directly on a thin 130 μm-thick glass substrate adhered to a polymeric-enclosed microscale NA reaction well (Figure 4.1).

Both loop-mediated isothermal amplification (LAMP) and PCR reaction mixtures contain pH-stabilizing buffers, which are electrically conductive and can be

Joule heated using an externally applied electric current. The sample temperature can, therefore, be precisely controlled by regulating the voltage drop applied across the thin film electrodes. As such, this RF-based electrokinetic technique allows for nucleic acid amplification without the need for external heating elements or cyclical pumping between heating zones. Further, because the applied RF frequency is significantly greater than the Faradaic reaction timescale at the electrode surfaces, the resulting electric current does not produce any observable electrochemical Faradaic reaction by-products or electrode delamination. The electrodes, therefore, do not require physical isolation from the nucleic acid sample and can be placed in direct contact with the reaction. A single electrode pair can be used to deliver current directly to conductive electrolytes for >50 h without observable performance degradation. Most importantly, the direct application of the RF electric current to the sample successfully amplifies target nucleic acids by both PCR and LAMP with minimally observed enzymatic degradation and presents a new method for performing microfluidic NAA without external resistive heating elements.

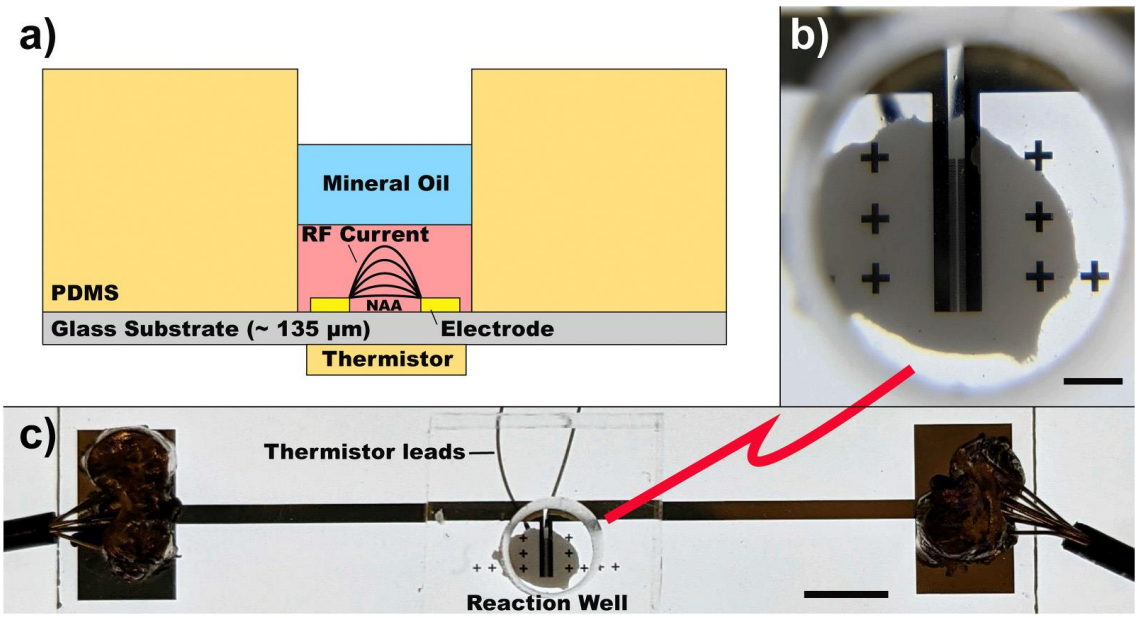

Figure 4.1 E-NAAMP joule heating device. (a) Schematic of E-NAAMP setup. (b) Top-down view of E-NAAMP sample well with co-planer electrodes. Scale bar 1 mm. (c) Fully assembled device with PDMS reaction well, surface epoxied thermistor with wire leads, and soldered wire leads. Scale bar 5 mm. Reprinted with permission from Yost & Gagnon. *Biomicrofluidics* 2022, *16* (1), 014101, Copyright 2022 AIP Publishing.[12]

Previous Joule heating approaches used either DC or low-frequency AC electric fields, which produced Faradaic reactions and necessitated the venting of the reactive products to atmosphere. Additionally, other methods utilized large reservoirs of conductive buffer as an isolated source of Joule heating.[71,127] Such isolation limitations and drawbacks are corrected in the electrokinetic Nucleic Acid Amplification (E-NAAMP) system, which yields no Faradaic by-products and requires no external buffer sources; and the only buffer source is the amplification mixture itself. E-NAAMP is a significant contribution to NAA technologies because it directly integrates a heating element into the NAA chip itself, significantly minimizing the device size, cost, e-waste, and design complexity.

4.3. Theory

This study investigates the influence of localized RF Joule heating on NAA. As shown in Figure 4.1(a), the electrokinetic experimental domain consists of a pair of thin film gold electrodes fabricated atop a thin ~130 μm-thick glass substrate. The electrodes are centered within a cylindrical polymeric well that contains a 25 μL NA reaction sample. An RF current is generated by a voltage difference applied across the electrodes. Joule heating, also known as Ohmic heating, occurs when the resulting electric current is passed within the liquid sample in order to produce heat.[58,128] The generated Joule heat and thermal profile conducts across the thin glass slide and is measured locally at the glass surface using a small temperature sensitive resister (e.g., thermistor) affixed to the underside of the glass substrate, as described in Materials and Methods.

The resulting experimental dependence of the voltage on the Joule heating temperature is influenced by a number of physical properties including the liquid conductivity, the ionic strength of the liquid, the pH of the liquid, and the applied voltage drop across the electrodes.[60,129–131] When an electric current is applied within a conductive buffer solution, the heat generated is transferred by thermal diffusion and liquid convection through the liquid, and then dissipated to the surroundings, including across the thickness of the thin glass substrate. The differential energy balance in the liquid domain is given as

$$\rho c_p \frac{\partial T}{\partial t} + \rho c_p \mathbf{v}\cdot\nabla T = k\nabla^2 T + \sigma E^2, \quad (4.1)$$

where within the liquid domain, ρ is the corresponding density, c_p is the specific heat, k is the thermal conductivity, σ is the electrical conductivity, T is the temperature, E is the magnitude of the externally applied electric field, and $\mathbf{v}$ the velocity vector of the

convective fluid flow. In this work, the fluid temperature is experimentally measured at the glass surface directly underneath the Joule heating electrodes. We assume thermal steady state within the thin glass substrate and a no-slip flow condition at the glass surface within the fluid sample well. Under these conditions, Eq. (4.1) can be simplified to

$$k\nabla^2 T + \sigma E^2 = 0, \quad (4.2)$$

where electric field, E, is dependent on the negative gradient of the voltage as $E = -\nabla V$. Neglecting the influence of temperature on the solution's electrical and thermal conductivity, the approximated Joule heated temperature rise, ΔT due to an applied potential, V, thus, scales as[35,39]

$$\Delta T \approx \frac{\sigma V^2}{k}. \quad (4.3)$$

Therefore, the resulting Joule temperature rise is predicted to scale as the square of the applied voltage dropped across the electrode pair, V^2.

4.4. Materials and Methods

4.4.1. Fabrication of E-NAAMP Devices

Our experimental system consisted of a cylindrical polymeric NA sample vessel affixed to a thin glass substrate. Centered within the sample vessel on the glass surface was a pair of thin metal film gold–chrome electrodes. To fabricate the electrodes for the E-NAAMP chips, metal deposition and standard photolithography techniques were used. 50 × 35mm^2 glass slides (12-545-GP; Fisherbrand) were cleaned in acetone and isopropanol and rinsed with de-ionized water. The glass surface was coated with a thin 20 and 30 nm film of chrome and gold, respectively, using e-beam evaporation. The gold film was then patterned using contact lithography. Each glass coverslip was spin-

coated and lithographically patterned using S1813 photoresist and subsequently wet etched using gold and chromium etchant (Transene Company, Inc.). After lithographic electrode patterning, a 0.5 cm-thick slab of polydimethylsiloxane (PDMS) was hole-punched with a 5mm biopsy punch (15111-50; Ted Pella, Inc.). The slab and the electrode slide were exposed to oxygen plasma (Jetlight, Model 42A), after which the punched-PDMS hole was then aligned and irreversibly bonded to the glass surface. The resulting device was incubated overnight at 80 °C to strengthen the PDMS-glass bond. The final device consisted of a hole-punched NAA reaction well with a pair of centered and aligned microelectrodes at the bottom well surface (Figure 4.1(b)). The electrode geometry consisted of a pair of co-planer parallel electrodes 12mm in length situated along the central region of the sample well. An evenly spaced 9mm long comb-line array of sharp pointed electrode teeth were fabricated along the edge of each electrode to spatially distribute the RF current within the electrode surface area in the center of the sample well. Each electrode was lead-terminated to a large thin film metal pad. Electrical connections to each pad were made using 6-cm long 20-gauge electrical hookup wire soldered to each electrode pad using a low melting point indium solder (Figure 4.1(c)). A conductive NAA sample was then loaded into the reaction well and served as the resistive load for the microelectrode pair on the glass surface. When a voltage was dropped across the electrodes, an RF current was driven through the liquid sample and was observed to heat by Joule heating. Fig. 4.2(a) illustrates the observed Joule heating in the sample well using an infrared (IR) thermal camera (FLIR TG130). While the IR camera could be used to monitor and subsequently control the reaction

temperature, a more precise and local surface temperature measurement was instead acquired using a surface-affixed thermistor.

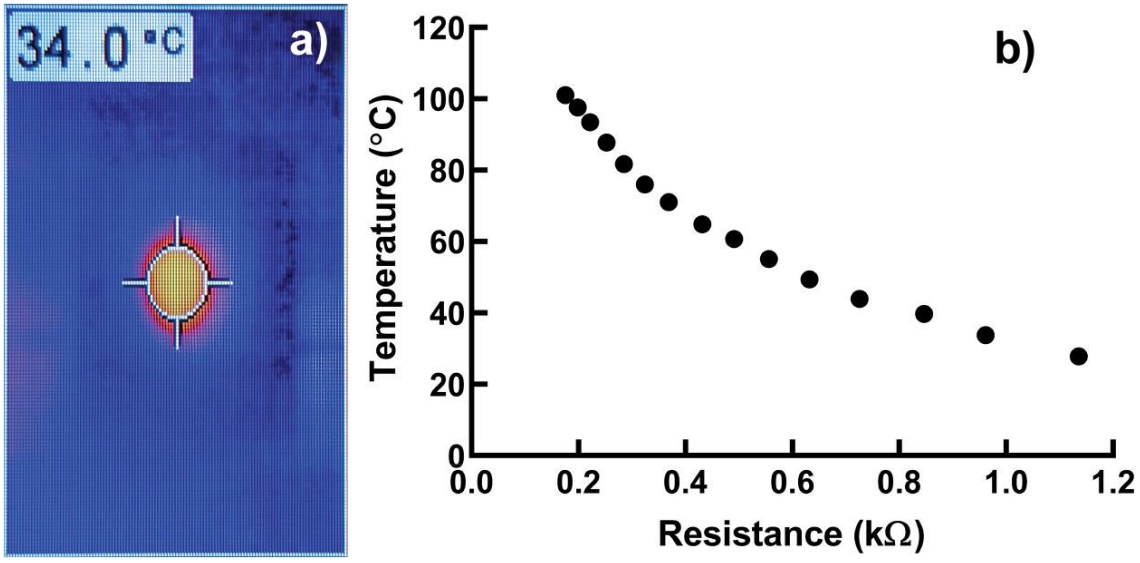

Figure 4.2 Joule heating thermistor calibration. (a) NA sample well temperature profile during RF Joule heating (40 MHz; 5 V_{pp}) of the E-NAAMP chip. Sample well temperature profile imaged using a FLIR TG130 IR thermometer. (b) Thermal calibration curve of surface mounted thermistor. Reprinted with permission from Yost & Gagnon. Biomicrofluidics 2022, 16 (1), 014101, Copyright 2022 AIP Publishing.[12]

4.4.2. Thermistor Calibration

To facilitate the temperature monitoring and thermal cycle control, we utilized a commercial negative temperature coefficient (NTC) thermistor (GA1K2A1; Mouser) epoxied to the underside of the glass side directly beneath the microelectrodes. To calibrate the thermistor, it was affixed directly over the center of a programmable hot plate (HS40; Torrey Pines Scientific) using a layer of thermally conductive silver grease (CW7100; Chemtronics) to ensure uniform heat transfer. A data acquisition (DAQ) device (LabJack Corporation, Model T4) was used to deliver a fixed voltage signal via an analog output (DAC0) to a 4–20 milliamp (mA) voltage-to-current converter (8B39-

01, Mouser) which converted this voltage to a known current. The resulting voltage generated across the thermistor was simultaneously measured using the DAQ's analog input, AIN0. The hot plate temperature was increased in 5 °C increments from 25 to 100 °C and at each temperature the system was allowed to reach a steady-state temperature. The voltage drop across the resister was recorded, the temperature dependent thermistor resistance, R was calculated using Ohm's law, R = V/I (Figure 4.2(b)). As expected, the NTC thermistor resistance decreased logarithmically with increasing temperature, T, and was fit to a logarithmic polynomial as

$$T = -39.98 \times \ln(R) + 31.97, \quad (4.4)$$

where R is the Ohmic resistance in kΩ and T is the temperature in °C.

4.4.3. E-NAAMP Chip Assembly and Operation

Once the thermistor was calibrated, it was permanently mounted to the underside of the glass side directly underneath the microelectrodes for use as the thermal sensor during NAA thermal cycling experiments. The thermistor was affixed to the glass coverslip using a thermally conductive aluminum epoxy adhesive (Arctic Alumina Thermal Adhesive; Arctic Silver). A function generator (Rigol DG4102) connected to a 40-dB gain RF amplifier (Mini-Circuits, ZHL-5W−1+) was used to deliver a RF voltage to the pair of microelectrodes on the glass surface. To measure the reaction well temperature, the voltage drop across the thermistor was converted to a resistance value using Ohm's law and subsequently converted to a temperature using the previously calibrated thermistor equation (Eq. (4.4)).

4.4.4. LAMP Procedures

The thermistor-calibrated RF Joule heating device was then used for two different NAA reactions: LAMP and PCR. In LAMP, the Joule heated temperature was held at a constant 65 °C using a fixed voltage drop across the microelectrodes. In terms of the LAMP chemistry, λ DNA (Sigma-Aldrich) served as our model proof-of-concept template. The λ DNA primer sequences (Integrated DNA Technologies, IDT) were adopted from the LAMP work of Nagamine et al.[66] (Table 4.1). LAMP reactions utilized a reaction mix containing 1.0× Warmstart® Colorimetric LAMP 2X Master Mix (NEB), 1.0×10^5 copies of λ DNA template, 0.2 μM of F3 and B3 primers, 0.4 μM of Loop-F and Loop-B primers, and 0.8 μM of FIP and BIP primers.[66] Control LAMP reactions were performed using a conventional benchtop thermal cycler (T100 Thermal Cycler, Bio-Rad) with reaction volumes of 10 μL for 60 min. Every 10 min, a LAMP reaction was removed from the thermal cycler, thermally quenched on ice, and imaged to develop a time course comparison with E-NAAMP. For the E-NAAMP LAMP reaction, the volume was 25 μL, 1 μL of which was the DNA template. The DNA template itself therefore has minimal influence on the final reaction volume electrical conductivity. To prevent sample evaporation during amplification, 25 μL of mineral oil was pipetted on top on the reaction volume. A $93mV_{pp}$ (pre-signal voltage; 18 V_{pp} amplified voltage) was supplied to the electrodes at 40 MHz to produce a constant temperature of 65 °C for 60 min, with pictures taken of the well every 10 min to monitor reaction progress. Both E-NAAMP and thermal cycler reactions were run for 60 min to ensure reaction completion, allowing for an even end point comparison between both heating methods.

Table 4.1 λ DNA LAMP primers.[66] Reprinted with permission from Yost & Gagnon. Biomicrofluidics 2022, 16 (1), 014101, Copyright 2022 AIP Publishing.[12]

Primer	Sequence (5' -> 3')	Length (nt)
F3	GGCTTGGCTCTGCTAACACGTT	22
B3	GGACGTTTGTAATGTCCGCTCC	22
FIP	CAGCCAGCCGCAGCACGTTCGCTCATAGGAGATATGGTAGAGCCGC	46
BIP	GAGAGAATTTGTACCACCTCCCACCGGGCACATAGCAGTCCTAGGGACAGT	51
LoopF	CTGCATACGACGTGTCT	17
LoopB	ACCATCTATGACTGTACGCC	20

4.4.5. PCR Procedures

Joule heating was also used to perform NAA via PCR. The model DNA template used in this PCR amplification work was an E. coli gene that codes for a strand of non-coding RNA, rnpB (377 nt).[132] The forward PCR primer for rnpB was 5'-GTAAACTCCACCCGGAGCAA-3' (20 nt) and the reverse PCR primer was 5'-ATAAGCCGGGTTCTGTCGTG-3' (20 nt). The resulting amplicon generated by PCR is 133 nt long. The primers and rnpB template were ordered from IDT.

The qPCR Master Mix (Bio-Rad) was diluted from a 2.0× concentrated stock. The PCR amplification reactions contained a 1.0× qPCR master mix, 250 nM forward primer, 250 nM reverse primer, and 1.8×10^7 copies of rnpB template per 25 μL of reaction volume. Similar to the LAMP reaction, the comparative positive thermal cycler PCR controls had a volume of 25 μL, and the E-NAAMP PCR volumes were 25 μL, with 25 μL of mineral oil atop in order to prevent sample evaporation. Thermal cycler amplifications were cycled between 95 °C for 5 s and 60 °C for 30 s, for 40 cycles. To cycle the E-NAAMP PCR reaction, the voltage–temperature cycle relationship was determined using the temperature–voltage dependence plot (Figure 4.4(a)). The pre-amplified voltage of 146 mV_{pp} from the function generator (28 V_{pp} amplified)

corresponded to 95 °C and 97 mV_{pp} (19 V_{pp} amplified voltage) corresponded to 60 °C. To perform PCR, the reactions were Joule heated under constant voltage to 95 °C for 30 s, and the voltage was then removed to allow the chip to cool using ambient air for 30 s. The Joule heated temperature of 60 °C was then applied for 50 s. The heating and cooling process was then repeated and cycled 40 times. Two cycles of this process, as measured with the surface thermistor are illustrated in Figure 4.3. Using the resistance–temperature calibration equation, the relevant temperatures for LAMP and PCR, 65, 95, and 60 °C, corresponded to thermistor resistance values of 0.44, 0.21, and 0.50 kΩ, respectively.

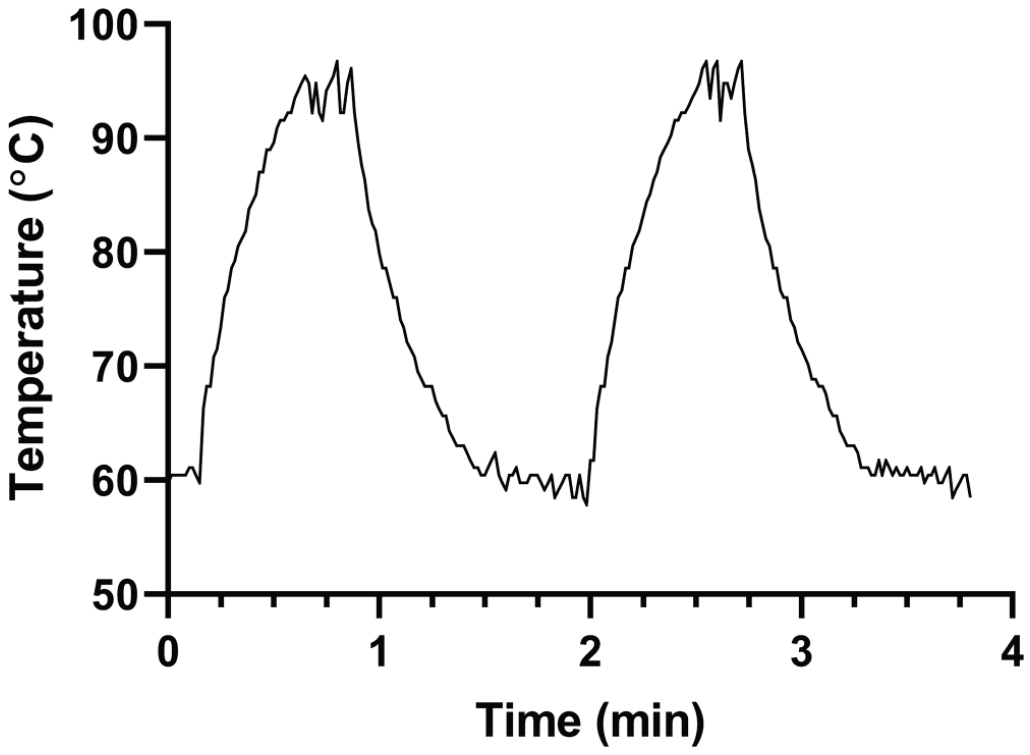

Figure 4.3 PCR thermal cycling by RF Joule heating. Surface thermistor temperature profile illustrating E-NAAMP PCR thermal cycling. A 40 MHz, 28 V_{pp} signal was applied to the electrodes for 30 s (95 °C), the voltage was removed, and switched to 19 V_{pp} (60 °C) for 50 s. PCR is subsequently driven via voltage cycling. Reprinted with permission from Yost & Gagnon. Biomicrofluidics 2022, 16 (1), 014101, Copyright 2022 AIP Publishing.[12]

To analyze the E-NAAMP PCR reaction products, the reactions were quenched with 5.0× Nucleic Acid Sample Buffer (Bio-Rad) to a concentration of 1.0× sample buffer. 5 μL of the mixture was loaded onto a 2% agarose gel (Sigma-Aldrich) infused with SYBR Green I (Lonza), along with 5 μL of a 100 bp ladder (Bio-Rad) and subjected to gel electrophoresis at 75 V for 100 min in 1.0× TAE buffer. The gel was then imaged in a ChemiDoc MP (Bio-Rad) and analyzed using Bio-Rad ImageLab software.

4.4.6. LAMP Colorimetric Analysis

Colorimetric LAMP measurements were performed using a rotated hue analysis. Based on previous colorimetric LAMP work, hue analysis has shown to produce the largest difference in pixel intensity values in color LAMP reaction images. As such, hue analysis has shown to be an optimal tool to analyze a colorimetric LAMP reaction time course.[133] Obtained LAMP images were color shifted using ImageJ in order to rotate the hue scale into a color range where red and yellow pixel values represented the upper and lower bounds of the hue scale, respectively.[134] For each image, the blue channel was shifted to an intensity range spanning 0–190 and the yellow channel was shifted to the pixel value of 255. Five different pixel values were acquired for each experimental image and averaged. The time course E-NAAMP and thermal cycler pixel values were then normalized such that 0 and the 60 min data points represented the initial (value = 1) and endpoint (value = 0) of the reaction, respectively. Pixel values were then plotted against time to generate a quantitative comparative plot of colorimetric LAMP reaction progress over time for both thermal cycler and E-NAAMP.

4.5. Results and Discussion

We first investigated the temperature–voltage dependence of the amplification buffers using the 1× qPCR mix diluted from a 2× qPCR Master Mix. The 1.0× qPCR mix conductivity was measured using a conductivity meter (Laquatwin EC-11) and found to be 11.61 ± 0.05 mS/cm. The 1× PCR mix was loaded into the sample chamber and subjected to an applied voltage varying from 0 to 30 V_{pp} and RF frequencies ranging from 10 to 50 MHz. A temperature–voltage curve was then obtained to determine how the induced temperature scales with the applied voltage. As depicted in Figure 4.4(a), the temperature exhibits a quadratic dependence on the applied voltage. This is further illustrated through plotting the temperature against square of the input voltage (T vs V^2) as shown in Figure 4.4(b), where the resulting temperature plot is linearized. Given the squared dependence of the voltage with temperature, the data strongly suggests the sample heating is indeed driven by Joule heating.

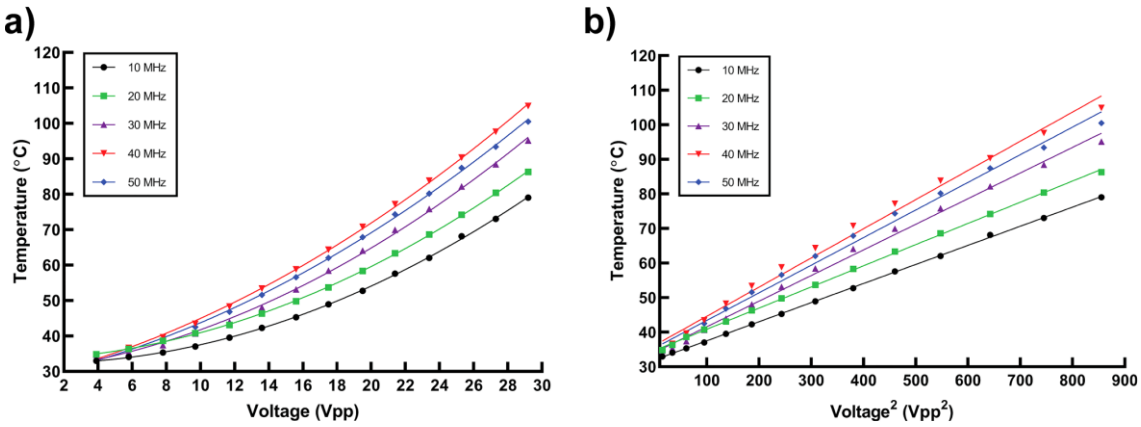

Figure 4.4 Thermistor temperature vs voltage for Joule heated 1.0× qPCR mix. (a) Temperature scales quadratically with voltage. (b) Temperature scales linearly with the square of voltage. Reprinted with permission from Yost & Gagnon. Biomicrofluidics 2022, 16 (1), 014101, Copyright 2022 AIP Publishing.[12]

The influence of voltage frequency on temperature was also investigated. As shown in Figure 4.4, the temperature increased with the applied frequency up to 40 MHz and subsequently decreased as the frequency increased to 50 MHz. This is likely due to gain losses during signal amplification as we near the bandwidth limitations of the RF amplifier.[135] Based on the maximum achieved temperature of 100 °C at 40 MHz, compared to that of 78 °C at 10 MHz, a 40 MHz operating frequency was deemed to be the optimal Joule heating operating frequency for the E-NAAMP experiments in this work. Finally, both the LAMP and PCR master mix pH was measured using a colorimetric pH indicator after exposure to a 40 MHz RF field frequency. No change in the sample pH via colorimetric shift in response to a prolonged (60 min) exposure to the RF voltage was observed (Figure 4.6(c)).

4.5.1. COMSOL Simulation of E-NAAMP

To better understand the heating effects and spatial temperature profile during E-NAAMP, we utilized COMSOL Multiphysics to compute the Joule heating temperature profile under LAMP conditions within the reaction well. This was accomplished by numerically solving the differential energy balance (Eq. (4.1)) coupled with the Navier–Stokes equation along a cross section of the amplification well. Fig. 4.5 shows the spatially dependent temperature profile. With a thermal Grashof number of ∼2400, a laminar buoyancy-driven flow serves to circulate the reaction fluid within the well.[136] An inherent thermal gradient exists in the well, as expected, with the active thermistor area represented by a black bar at the bottom of the well (∼65 °C). The temperature in the well varies from approximately ∼64–69 °C, above the 65 °C required to drive LAMP. The temperature differential between the well bottom and the well bulk fluid is

likely due to rapid heat transfer across the thin glass slide on the well bottom. Additionally, the velocity streamlines show a high degree of mixing within the well, leading to the temperature uniformity. This numerical simulation further demonstrates the utility of E-NAAMP in that a combination of volumetric Joule heating and buoyancy-driven flow produce a temperature profile with a minimal temperature gradient.

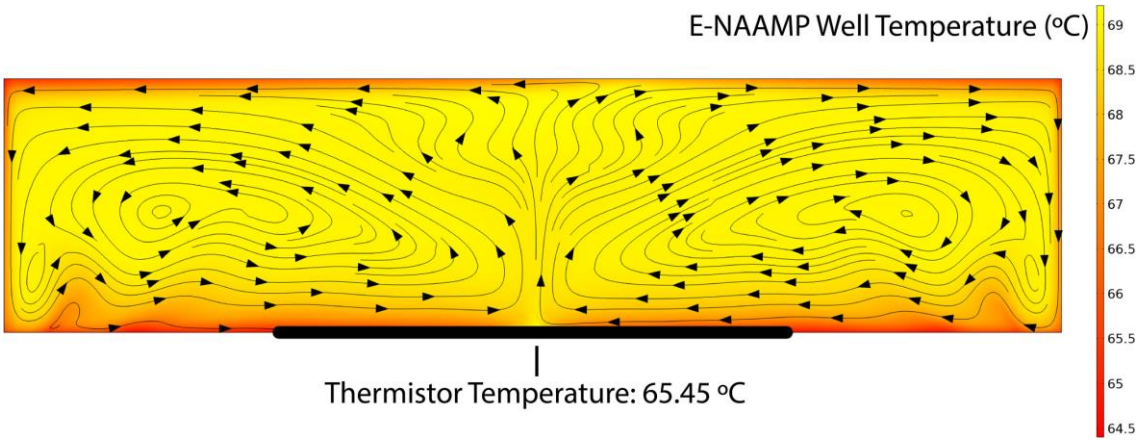

Figure 4.5 Numerical simulation of the E-NAAMP system. Numerical simulation of the temperature profile produced via Joule heating under temperature conditions for the LAMP reaction (65 °C). A combination of volumetric Joule heating and buoyancy-driven flow produce a relatively consistent temperature profile with minimal thermal gradient. The black bar at the base of the well denotes the region in which the thermistor is affixed to the device and is used to measure the E-NAAMP well temperature. Reprinted with permission from Yost & Gagnon. Biomicrofluidics 2022, 16 (1), 014101, Copyright 2022 AIP Publishing.[12]

4.5.2. E-NAAMP (LAMP) of λ DNA

LAMP is an isothermal alternative to traditional amplification methods, such as PCR. It has the advantage of requiring no thermal cycling and can, therefore, be performed on a hot plate, water bath, or heat block.[67] Additionally, a recent LAMP innovation has been the use of pH indicators with LAMP master mixes. Because the pH of the LAMP reaction volume decreases over the course of the isothermal reaction,

NAA progress can be colorimetrically detected by the pH indicator color change. Using the Warmstart® Colorimetric LAMP 2X Master Mix, which contains the pH indicator phenol red, a color change from magenta to yellow over the course of a reaction indicates a positive LAMP reaction, whereas no change from the initial magenta color indicates a negative LAMP reaction. This allows for simple visual analysis of LAMP reactions without the need for gel-based analysis.[133,137,138]

Figure 4.6(a) shows a time course of a colorimetric LAMP reaction in a traditional thermal cycler using λ DNA as the template. The reaction volume color is initially magenta (time, t = 0 min) and subsequently transitions to a color of yellow (t = 60 min) over the course of the reaction, indicating positive amplification of λ DNA. This reaction serves a positive control and basis of comparison for E-NAAMP. Fig. 4.6(b) shows the same reaction setup and time course, but instead driven by E-NAAMP. Like the thermal cycler control, the reaction initially exhibits a magenta color (t = 0 min) and progresses to yellow after 60 min, demonstrating no major enzyme activity loss during Joule heating. In the absence of template (negative control), no color change is observed in either the thermal cycler or E-NAAMP reactions, as seen in Figure 4.6(c). This lack of a color change in the absence of template indicates that no pH change took place and, therefore, no Faradaic reactions occurred during E-NAAMP due to Joule heating. The colorimetric change from magenta to yellow is indicative of a LAMP-driven pH change, which corresponds to a positive amplification of λ DNA using E-NAAMP. Finally, Figure 4.6(c) provides a dynamic comparative analysis of the colorimetric change as shown in Figures 4.6(a) and 4.6(b). As shown in Figure 4.6(c), E-NAAMP is observed to transition from magenta to yellow more rapidly than the thermal cycler control. This

could perhaps be due to the aforementioned thermal advantages of E-NAAMP since the Joule heating within the reaction well is volumetric in nature as opposed to traditional boundary driven thermal amplification heaters. To our knowledge, this result represents the first reported DNA sequence that has been successfully amplified by LAMP using AC electrokinetic Joule heating.

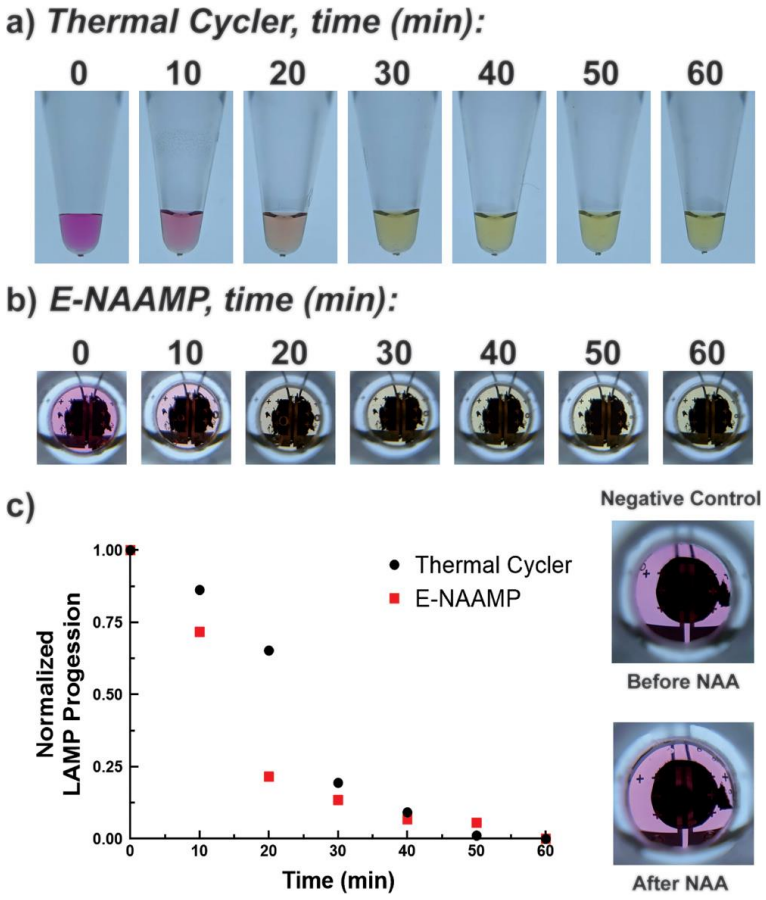

Figure 4.6 Joule heating amplification by LAMP. (a) Time course of colorimetric LAMP in a thermal cycler. (b) Time course of colorimetric LAMP using E-NAAMP. (c) E-NAAMP vs thermal cycler reaction progress analyzed via rotated hue analysis. No color change is observed after nucleic acid amplification (NAA) in the absence of template as indicated by the negative control. Reprinted with permission from Yost & Gagnon. Biomicrofluidics 2022, 16 (1), 014101, Copyright 2022 AIP Publishing.[12]

4.5.3. E-NAAMP (PCR) of rnpB DNA

While LAMP is an effective tool to develop E-NAAMP technology due to its isothermal nature, running E-NAAMP with PCR is a more attractive goal due to PCR's widespread use in laboratory settings. Using the E. coli sequence, rnpB, E-NAAMP was used to amplify a 133 nt segment of rnpB, alongside control amplifications performed in a thermal cycler and hot plate.[132] As seen in Figure 4.7, E-NAAMP successfully amplified rnpB (lane 6) with band densitometry showing an amplicon level over 90% that of the thermal cycler's amplicon level (lane 4). The two negative controls — lane 2; no PCR reaction and lane 3; no template, did not amplify as expected. While PCR has been achieved using Joule heating in previous work, this represents the first time PCR has been achieved using direct Joule heating at radio frequencies with minimal effect on enzyme activity.[71,127]

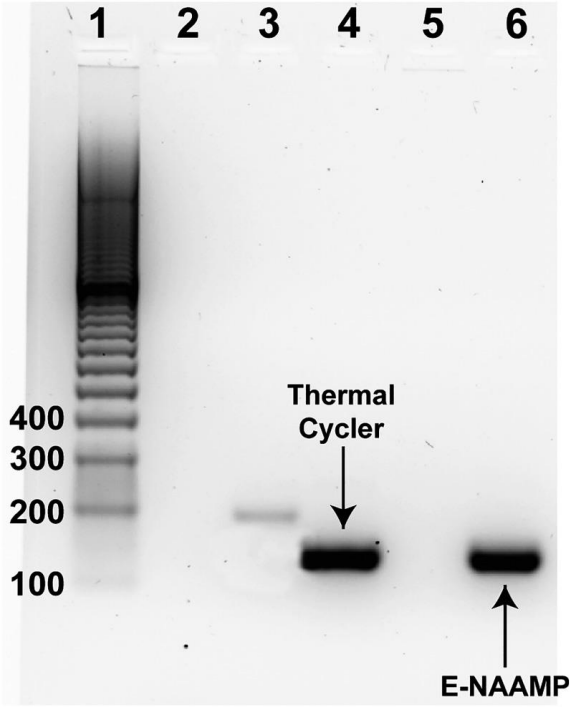

Figure 4.7 Joule heating amplification by PCR. Amplification of rnpB E. coli DNA using E-NAAMP (PCR). Lane 1 – 100 bp marker. Lane 2 – no reaction control. Lane 3 – no template control. Lane 4 – thermal cycler control. Lane 5 – hot plate control. Lane 6 – E-NAAMP. Reprinted with permission from Yost & Gagnon. Biomicrofluidics 2022, 16 (1), 014101, Copyright 2022 AIP Publishing.[12]

4.6. Conclusions

In the present work, we introduced a novel NAA amplification method using radio frequency Joule heating. Unlike previous NAA methods using Joule heating, the high frequency nature of this approach enables the application of an RF current directly to the sample without producing gaseous electrolysis by-products or pH changes and with minimal observed influence on the NAA product. The device construction consisted of a single cylindrical reaction chamber in contact with a pair of surface fabricated microelectrodes. A conductive DNA sample was loaded into the chamber and directly exposed to a high frequency (10 – 50 MHz) applied potential (0 – 30 V_{pp}). We observed the temperature within the reaction sample to rise as the square of the applied

voltage (V^2), which is consistent with that of predicted Joule heating scaling. The RF AC electrokinetic heating method was utilized to amplify DNA by isothermal LAMP and in a thermal cycling method for PCR. We showed that this RF regime produces a minimal observed impact on enzymatic activity as compared to our thermal cycler control reactions with PCR amplicon levels being comparable to those generated using the benchtop cycler. This new heating method offers a way to volumetrically heat samples at the microfluidic scale without major enzyme damage and the need for bulky external heaters. With future improvements in temperature control and measurement, the PCR time scales can be reduced and allow for the development of a next-generation of miniaturized low cost and rapid NAA tools for use in DNA-based diagnostics.

Section 4 introduced a novel heating method to drive nucleic acid amplification, E-NAAMP, which operates on the principle of high-frequency Joule heating. While this system was successful in amplifying DNA using multiple amplification methods, there are some inherent issues with the E-NAAMP chip itself. First, the chip requires fabrication in a clean room, utilizing expensive and time-consuming procedures such as electron beam evaporation and photolithography. Secondly, it utilizes expensive materials, chrome and gold, for the electrodes which drive up device fabrication costs. Finally, the E-NAAMP chip is fabricated upon thin glass slides which can break during fabrication and operation. These drawbacks prevent E-NAAMP from being a truly viable alternative to other microfluidic NAA methods. Section 5 attempts to address these drawbacks by adapting E-NAAMP onto a novel paper microfluidic platform called Microfluidic Pressure-in-Paper (µPiP).

5. ELECTROKINETIC NUCLEIC ACID AMPLIFICATION (E-NAAMP) USING PAPER-PDMS MICROFLUIDICS AND HIGH-FREQUENCY JOULE HEATING

5.1. Overview

We present a novel paper-based nucleic acid amplification (NAA) technique using electrokinetic nucleic acid amplification (E-NAAMP). In E-NAAMP, a high radio frequency (RF) potential is applied across a conductive aqueous sample to induce an Ohmic current and drive the sample temperature to increase by Joule heating. Using this RF approach, we investigate the ability to induce E-NAAMP in pressured paper-based microfluidic channels. We use the Microfluidic Pressure-in-Paper (μPiP) method to encapsulate synthetic and natural fiber-based paper channels between thin sheets of polydimethylsiloxane (PDMS) with two strips of conductive PDMS that have been infused with carbon black (PDMS-CB) to act as electrodes in contact with the paper channels. A high-frequency (38 MHz) voltage is applied across a conductive NAA sample via the PDMS-CB electrodes to generate Joule heating within the paper structure. Here, we show that μPiP -based E-NAAMP can amplify nucleic acids using the loop-mediated isothermal amplification (LAMP) reaction. We first investigate the pore-scale temperature profile numerically by solving the relevant energy transport equations within digitized paper fiber domains obtained using microCT scans. We compare these temperature-voltage predictions to those measured experimentally and demonstrate good agreement, suggesting that RF Joule heating is a viable method for electrokinetically heating paper-based microfluidic platforms. We next examine the effect of a porous substrate on NAA and demonstrate that the carrier protein, bovine

serum albumin (BSA), is required for paper-based NAA reactions by preventing polymerase adsorption within the paper structure. Finally, we show successful NAA in paper using E-NAAMP with multiple paper fiber types (cellulose and glass), while also further demonstrating BSA's necessity for paper E-NAAMP success. Our results demonstrate that paper-based microfluidic NAA using Joule heating is a viable alternative to traditional microfluidic NAA devices by offering substantial heating element miniaturization and decreased fabrication complexity when compared to both traditional and Joule-heated microfluidic NAA devices.

5.2. Introduction

Nucleic acid amplification (NAA) is an essential technique for disease diagnostics due to its ability to detect nucleic acid (NA) biomarkers at low concentrations in complex samples, including human blood, saliva, and serum.[139–141] With the rise of worldwide pandemics, there has been an increased need for rapid and small-scale disease NAA diagnostic tools. In many cases, human samples collected in the field can often require time consuming transport to a centralized lab for analysis, which limits the use of NAA in low-resource settings. While effective, eliminating the need of a centralized lab is challenging because conventional NAA is performed using an expensive and bulky thermal cycler, hindering the ability to be miniaturize and decentralize this method. Due to these drawbacks, microfluidics-driven NAA has developed as an attractive alternative due the small-scale, rapid time-to-result, and potential use in low-resource settings.[9] Microfluidic NAA is normally performed in devices with thermally cycling serpentine channels in order to geometrically control the number of polymerase chain reaction (PCR) thermal cycles, or in stationary microscale

reaction chambers that can be either rapidly heated and cooled for reactions like PCR or maintained at constant temperatures for reactions like loop-mediated isothermal amplification (LAMP). While these devices are effective at NAA, they rely upon bulky resistive heating elements fixed to the underside of the devices which can limit device portability and size.[69,70] Microfluidic LAMP devices do require thermal cycling; however, these devices are often placed upon bulky hot plates, placed in incubators, use traditional microfluidic integrated heaters, rely on chemical heat, or use an external heating gun. These devices use creative ways to apply heat to a device, requiring complex fabrication or a reliance on traditional, large-scale lab equipment.[142–146]

Recently, Yost et al. introduced a novel NAA method called electrokinetic nucleic acid amplification (E-NAAMP). In E-NAAMP, the NAA sample itself forms the resistive heating element, which significantly reduces the device complexity. E-NAAMP improved on both traditional and Joule-heated microfluidic-based NAA devices by using a radio frequency (RF) voltage (>40 MHz) applied directly to the NAA reaction mixture using a pair of co-planar metal film gold electrodes microfabricated directly onto the surface of the reaction chamber. The resulting RF current induced sustainable Faradaic reaction-free Joule heating within the conductive nucleic acid sample and was used to amplify NA's via both LAMP and PCR, did not generate electrolysis gas byproducts or pH changes, and did not require bulky heaters attached to the underside of the device. Despite these advantages, this method has some drawbacks in that these E-NAAMP devices required expensive microfabrication materials for the electrodes, these fabrication procedures necessitated the use of a clean room, and the resulting devices were fabricated on thin glass slides which can break during use.[12]

One way to improve E-NAAMP is to use the paper-based microfluidics fabrication method known as microfluidic pressure-in-paper (μPiP). In μPiP, paper-based microfluidic channels are tightly laminated between two thin polydimethylsiloxane (PDMS) membranes. Paper lamination serves to both prevent fluid evaporation from the paper channels and to enable the ability to drive flows within the device using an external pressure gradient rather than capillary action or wicking, which allows for faster, more tunable and continuous flow rates though the paper channels. Finally, μPiP devices can be fabricated without use of a clean room, significantly reducing the equipment costs and fabrication time required for device fabrication. Additionally, μPiP fabrication allows for rapid prototyping of paper microfluidic devices. μPiP has been used to fabricate devices to study red blood cell deformability and electrokinetically concentrate DNA.[13] μPiP's innovations address some drawbacks experienced by traditional paper microfluidic devices, namely fluid evaporation during operation & slow flow rates.[78] Heating open paper microfluidic channels to NAA temperatures result in evaporation, leading to limited or no NAA. Traditional paper microfluidic NAA devices typically overcomes evaporation issues by sealing the device in plastic and placing the device in an incubator or atop of an external heater to run the NAA reaction.[82,142,143] μPiP overcomes these evaporation issues by encapsulating both the heating element (electrodes) and the amplification zone (paper microfluidic channel) within chemically bonded PDMS sheets, thus preventing evaporation and eliminating the need for boundary-driven heating. Additionally, μPiP does not require expensive and costly fabrication materials and machinery, and devices produced are more robust than traditional glass-based E-NAAMP devices. These

advantages present µPiP-fabricated devices as viable alternatives for E-NAAMP to traditional glass-based devices.

In this work, we investigate the feasibility of using µPiP-fabricated paper devices to perform E-NAAMP. We first demonstrate that Joule heating is a viable heating mechanism for paper channels within µPiP by quantifying the temperature and voltage relationship for two different types of paper: Whatman 1 (W1), a natural & cellulose-based paper, and Ahlstrom-Munksjö Grade 142 (AM142), a synthetic and glass-based paper. We then compare this relationship to a finite-element computational model generated by COMSOL Multiphysics, using a digitized domain captured from 3D microCT scans. Next, we investigate the inhibitor effect that paper has on NAA reactions and investigate the influence that bovine serum albumin (BSA) has on LAMP reactions. Finally, we demonstrate E-NAAMP's versatility as a heating platform by amplifying a simple DNA template using LAMP on paper driven by Joule heating and show this Joule heating method is compatible with multiple paper types, but requires BSA passivation for successful paper-based Joule heating NAA.

5.3. Materials and Methods

5.3.1. Paper E-NAAMP Device Fabrication and Imaging

Paper-based E-NAAMP devices were fabricated using the µPiP method previously reported.[13] Briefly, microfluidic paper channel geometries were cut from sheets of Whatman 1 (cellulose fiber, 11 µm pore size, 180 µm thickness) or Ahlstrom Munksjö Grade 142 (glass fiber, 10 µm pore size, 850 µm thickness), using a CO2 laser cutter (LS-2440, Boss Laser). Paper channel geometries consisted of a 5 mm^2 square-shaped NAA chamber with a long rectangular paper-fluidic loading channel, 7.5 mm x 2.5 mm long. The CO_2-cut paper geometries were then soaked in varying weight-to-

volume ratio solutions of BSA (or water for devices not treated with BSA) and were subsequently dried on a hot plate at 55 °C. The dried paper was then laminated between two 0.5-mm thick PDMS membranes. Prior to lamination, a pair of commercially available conductive carbon black PDMS membranes (PDMS-CB, MyTech Ltd.) 5 mm in width and 12 mm in length were positioned across the width of the paper reaction chamber. The PDMS-CB strips served as electrodes in order to apply the necessary Joule heating RF voltage across the paper channel. The PDMS sheets were hole-punched using a 3-mm radius hole punch (Ted Pella) to allow for fluidic channel inlets and PDMS-CB electrode connection points and were then oxidized using a handheld tesla coil (Electro-Technic Products, Model BD-20AC). The conductive PDMS-CB electrodes were oxidized using oxygen plasma (Jetlight, Model 42A) due to observed damage the tesla coil causes to the conductive PDMS-CB electrodes. The paper channels and PDMS-CB strips were then aligned and laminated between the PDMS membranes such that the electrodes were in direct contact with either side of the paper amplification zone. The device was then placed in a benchtop heat press (Dulytek DHP5) at 55 °C for 10 minutes to fully laminate and bond the electrodes and the paper channel within the PDMS membranes. After lamination, the µPiP devices were incubated at 80 °C for 1 hour to further facilitate the oxygen plasma induced bonding between the PDMS sheets and the PDMS-CB electrodes. To deliver a voltage across the PDMS-CB electrodes, a pair of 21-gauge solid copper wire posts (diameter = 0.75 mm, length = 2.5 cm, Arcor Electronics) were pierced and inserted into the PDMS-CB regions and secured using electrically conductive ink (Techspray). Finally, a negative temperature coefficient (NTC) thermistor (GA1K2A1, Mouser) was affixed to the

bottom-side of the device reaction chamber using a thermally conductive epoxy adhesive (Arctic Alumina Thermal Adhesive; Arctic Silver). The thermistor measured the temperature of the paper E-NAAMP reaction on the underside of the PDMS membrane by converting an electrical resistance to a temperature. The thermistor was calibrated using previously reported methods prior to being affixed to the paper E-NAAMP device.[12] The resulting fabrication workflow describing this device fabrication process is depicted in Figure 5.1(a).

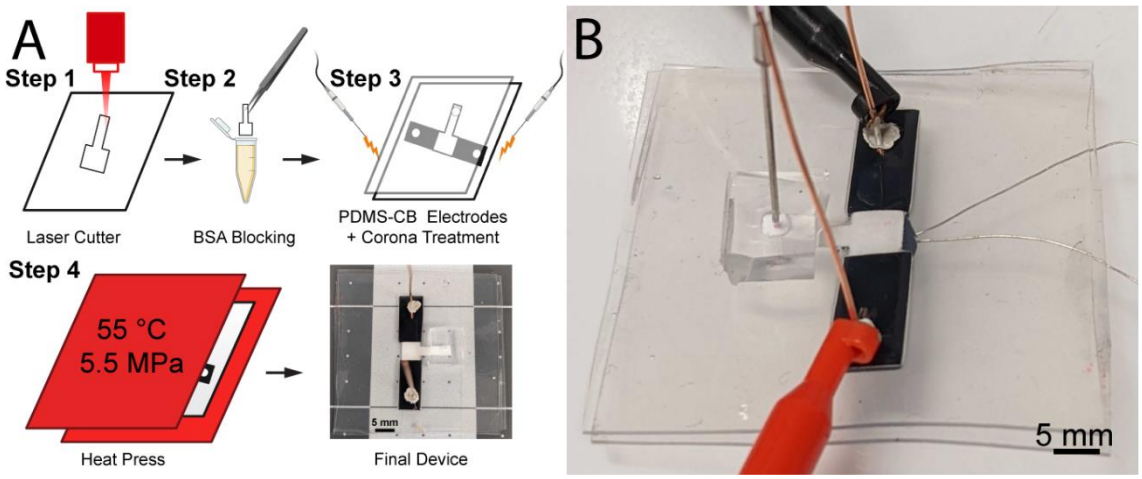

Figure 5.1 Paper E-NAAMP device. (a) Device fabrication workflow for paper E-NAAMP devices created using µPiP. Created with Biorender.com (b) Paper E-NAAMP device with bottom-side thermistor attached and copper posts inserted to allow voltage delivery.

5.3.2. E-NAAMP Device Operation and Temperature Analysis

In this work, NAA was performed isothermally using LAMP. During LAMP, the reaction zone temperature was held at a constant 65 °C using a fixed RF voltage applied across the PDMS-CB electrodes (Figure 5.1(b)). λ DNA (Sigma-Aldrich) was used as a proof-of-concept template, using LAMP primers (Integrated DNA Technologies) and λ DNA template concentrations adopted from the work of Nagamine et al.[66] LAMP

reactions used to generate Figure 5.5 contained 1.0x Warmstart® LAMP Kit Mix (New England Biolabs, NEB), 4.0×103 copies/µL of λ DNA template, 0.2 µM of F3 and B3 primers, 0.4 µM of Loop-F and Loop-B primers, and 0.8 µM of FIP and BIP primers. LAMP reactions used to produce Figure 5.4 necessitated use of a component kit, with the reactions containing 1x Isothermal Amplification Buffer (NEB), 10 mM MgSO4 (NEB), 1.4 mM of each dNTP (NEB), 8 units/25 µL of Bst 2.0 Polymerase (NEB), 4.0×10^3 copies/µL of λ DNA template, 0.2 µM of F3 and B3 primers, 0.4 µM of Loop-F and Loop-B primers, and 0.8 µM of FIP and BIP primers.

A syringe pump (Cole-Parmer 78-8200C) was used to drive LAMP reaction mix down the paper channel. Once the paper channel was filled, flow was stopped. The liquid volume of the paper amplification zone was 3.4 ± 0.9 µL for W1 and 24.0 ± 2.7 µL for AM142. The conductive NAA sample within the paper channel reaction zone then served as the resistive load for the PDMS-CB electrodes. The paper E-NAAMP device was then powered and operated as reported previously. In short, a function generator (Rigol DG4102) connected to a 40-dB gain RF amplifier (Mini-Circuits, ZHL-5W-1+) delivered a 38 MHz sinusoidal peak-to-peak voltage (Vpp) to the conductive PDMS-CB E-NAAMP electrodes. These electrodes were in direct contact with both the paper channel and the conductive amplification mixture. The conductive nature of the reaction allowed for heating to occur when subjected to a high-frequency voltage. The paper reaction well temperature was then measured using the bottom-side thermistor.[12] To control the temperature, the applied voltage was increased until the reaction well reached 65 °C (~30 seconds to reach 65 °C) and was then regulated manually to account for minor (<10%) drift over the amplification period (40 minutes). Temperature drift and

variation between devices can be attributed to inherent fabrication differences between devices. These devices are currently fabricated by hand, but upon expansion of fabrication to a larger scale utilizing accurate machinery, we hypothesize temperature drift to be negligible for machine-created devices.

After amplification, the laminated paper devices were cut open and the amplification zone of the paper channel was removed and dried at room temperature. Amplified DNA was eluted from paper using 25 µL of H2O, 10 µL of which was mixed with 2.5 µL of 5x Nucleic Acid Sample Buffer (Bio-Rad) to a final concentration of 1x sample buffer. 10 µL of the mixture was loaded onto a 2% agarose gel infused with 1.0x SYBR Green I (Invitrogen) and subjected to gel electrophoresis at 75 V for 100 minutes using 1.0x Tris-Acetate-EDTA (TAE) buffer. The gel was subsequently imaged in a ChemiDoc MP (Bio-Rad) and analyzed using ImageLab software (Bio-Rad)

5.4. Results and Discussion

5.4.1. Paper E-NAAMP System Heating Analysis

We first investigated the spatially dependent temperature profiles generated within the paper E-NAAMP devices for both W1 (Figure 5.2) and AM142 (Figure 5.3) paper types in order to investigate their capacity to be Joule heated for LAMP. Previous work by Yost et al. has shown, numerically and experimentally, that Joule heating is a viable heating method for a glass-based E-NAAMP device, however the numerical simulation was for one condition: one liquid conductivity and one applied voltage, which generated one temperature profile. To fully investigate paper E-NAAMP's heating ability, we expanded this simulation to include multiple liquid conductivities and multiple applied voltages. We investigated the distribution of the temperature profile within the center of the device and examined whether our experimental heating data

would agree with heating data generated numerically. The Joule heating temperature profiles within the paper reaction well were numerically computed using the finite element package, COMSOL Multiphysics (COMSOL Inc., Burlington, MA). To generate an accurate 3D digital domain, we used micro computed tomography (micro-CT) scans to image the porous paper structure. Micro-CT scans of a small section each paper substrate (Figure 5.2(a) and 5.3(a)) were captured using the SkyScan 1272 bench top Micro-CT scanner from Micro Photonics Inc. (1.5 µm voxel size, 800 ms exposure time). Each 3D imaged was digitized into a finite element domain using CTvox software. The dimensions of the micro-CT scanned paper substrates were 800 µm x 675 µm x 80 µm for W1 and 725 µm x 650 µm x 400 µm for AM142. Using COMSOL, each paper domain was subjected to far-field electric potential boundary conditions in order to mathematically capture the electric field conditions within the porous substrate. The resulting 3D Micro-CT micrographs for W1 and AM 142 paper substrates are shown in Figure 5.2(b) and Figure 5.3(b), respectively. The differential energy balance was solved numerically using COMSOL with a far-field isopotential boundary conditions for both σ_1 and σ_2 (conductivities of PBS solutions) at various voltages, and for both paper types, W1 and AM142. Top-down views of the simulated temperature profiles are shown in Figures 5.2(c) and 5.3(c) and depict a relatively uniform temperature distribution over the microCT scan area.

Each FEM model utilized the electrical properties of electrolytes with ionic conductivities typical of commercially available LAMP mixes. To control ionic conductivity experimentally, we used two different phosphate-buffered saline (PBS) solutions with ionic conductivities of $\sigma_1 = 5.13 \pm 0.01$ mS/cm and $\sigma_2 = 7.58 \pm 0.02$

mS/cm. These PBS conductivities fall within the typical conductivity ranges of commercially available LAMP mixes, as shown in Table 5.1. For each paper type, the PBS solutions were driven into the paper E-NAAMP devices and subjected a varying applied voltage, ranging from 0 – 50 volts peak-to-peak (V_{pp}) at a fixed frequency of 38 MHz and the resulting Joule heated temperature was measured using the bottom-side thermistor. This specific heating frequency was selected based on previous E-NAAMP work showing that the optimum RF amplifier response to induce Joule heating was observed at applied frequencies ~40 MHz. These resulting experimental temperature curves for each electrical conductivity are plotted in Figure 5.2(d) for W1 (circle & square points) and in Figure 5.3(d) for AM142 (circle & square points). Predictably, given the known dependence of temperature on voltage and conductivity[12], the induced temperature scales non-linearly with the applied voltages and the higher ionic conductivity solutions yielded greater temperatures for a given applied volage. Interestingly, we observed that AM142 exhibited more rapid heating than W1, reaching LAMP reaction temperatures (65 ºC) with less applied voltage than W1.

Table 5.1 Conductivities of Commercial LAMP Master Mixes.

Company	LAMP Mix	Concentration	Conductivity (mS/cm)
New England Biolabs	Warmstart® LAMP Kit (DNA & RNA)	1x	7.29 ± 0.03
New England Biolabs	WarmStart® Colorimetric LAMP 2X Master Mix (DNA & RNA)	1x	6.45 ± 0.10
Biosearch Technologies	LavaLAMP DNA Master Mix	1x	3.90 ± 0.03

Finally, the resulting simulated Joule-heating temperatures at various voltages were plotted and compared to the experimental Joule-heating data for both PBS mixtures and paper types, seen in Figures 5.2(d) and 5.3(d). These temperature measurements

were also compared to those predicted by the Joule heating FEM simulations. Experimental data is represented by circular or square points and simulation data is represented by a curve. Both simulation and experimental data show good agreement, with coefficient of determination (R^2) being ≥ 0.993 for all four conditions. For AM142 simulations, the heat transfer coefficient (HTC) for both σ_1 and σ_2 was 450 W-m^2/K. The HTC was 121 W-m^2/K for σ_1 simulated on W1 and150 W-m^2/K for σ_2 simulated on W1. Differences in HTC's for the same paper type can be attributed to paper E-NAAMP devices being single use, thus the heat transfer properties varied between devices due to inherent inconsistencies in device construction. The devices themselves were operated in floating configuration and a buoyancy driven air flow was capable of being generated across the heated paper surface which provided a natural means of convective-induced cooling. As such, our reported HTC's are approximately one order of magnitude larger than previously reported HTC's for simulations of Joule-heated microfluidic devices (10 W-m^2/K).[147–149]

Our numerical and experimental results demonstrate that our high frequency Joule heating technique is a viable heating mechanism for the laminated paper microfluidic channel types. Simulations show even heating within the center of the device, having no excess heating zones due to electric field distribution and experimental and simulated results match with mathematical expectations of Joule heating. To the best of our knowledge, this is the first instance of liquid Joule heating has been simulated in micro-CT imaged porous paper substrates.

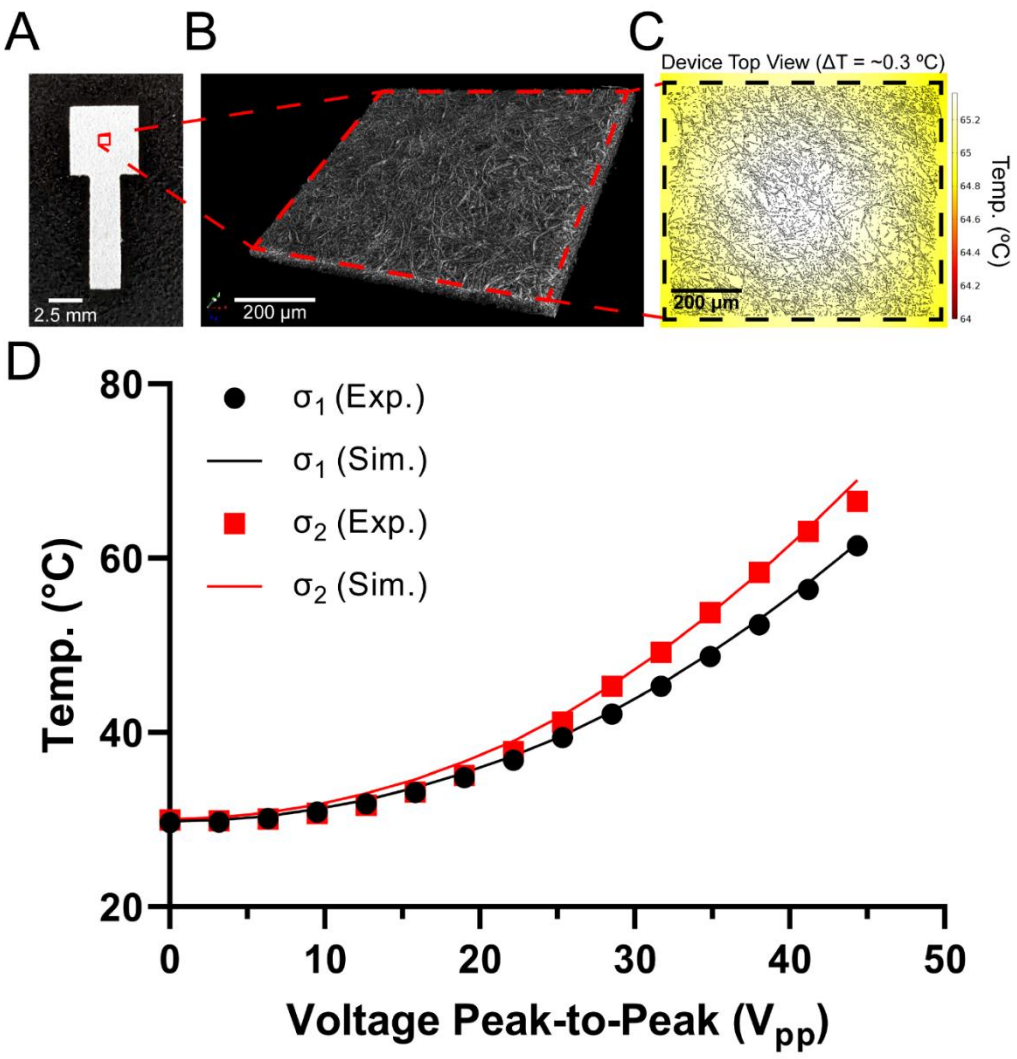

Figure 5.2 Joule heating analysis of Whatman 1. (a) Image of Whatman 1 paper microchannel used in paper E-NAAMP devices. (b) MicroCT scan of an 800 µm x 675 µm x 80 µm piece of Whatman 1, generating a 3D image. (c) Joule heating simulation using COMSOL Multiphysics of a 2D slice of Whatman 1 taken from (b), showing even heating throughout the simulation. (d) Experimental temperature-voltage relationship (points) plotted with simulated temperature-voltage relationship (curve) using finite-element analysis in COMSOL at two different conductivities for Whatman 1 paper. Simulations shows good agreement with experimental results (R^2 (σ_1) = 0.999, R^2 (σ_2) = 0.996). σ_1 = 5.13 ± 0.01 mS/cm, σ_2 = 7.58 ± 0.02 mS/cm.

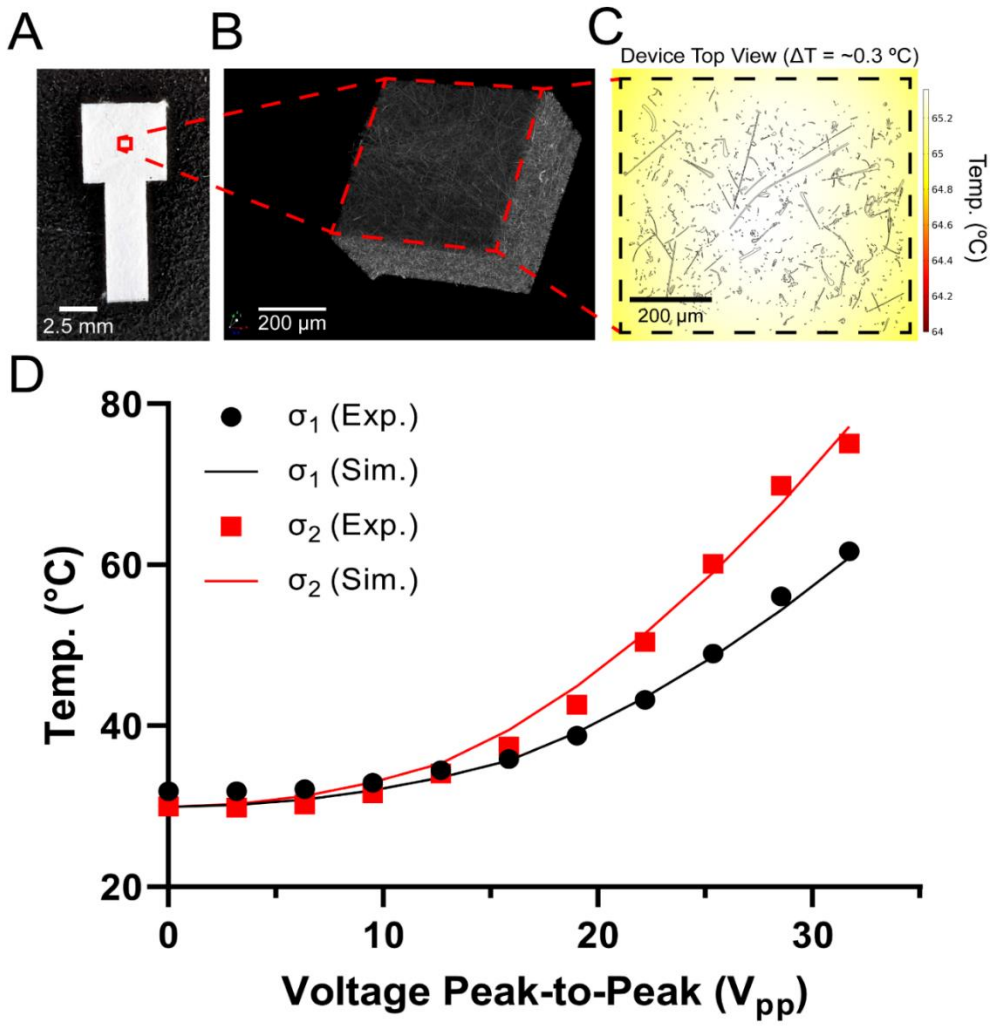

Figure 5.3 Joule heating analysis of Ahlstrom-Munksjö Grade 142. (a) Image of Ahlstrom-Munksjö Grade 142 paper microchannel used in paper E-NAAMP devices. (b) MicroCT scan of a 725 µm x 650 µm x 400 µm piece of Ahlstrom-Munksjö Grade 142, generating a 3D image. (c) Joule heating simulation using COMSOL Multiphysics of a 2D slice of Ahlstrom-Munksjö Grade 142 taken from (b), showing even heating throughout the simulation. (d) Experimental temperature-voltage relationship (points) plotted with simulated temperature-voltage relationship (curve) using finite-element analysis in COMSOL at two different conductivities for Ahlstrom-Munksjö Grade 142 paper. Simulations shows good agreement with experimental results (R^2 (σ_1) = 0.994, R^2 (σ_2) = 0.993). σ_1 = 5.13 ± 0.01 mS/cm, σ_2 = 7.58 ± 0.02 mS/cm.

5.4.2. Bst 2.0 Polymerase and Paper Interaction

With the ability to heat the W1 and AM142 substrates, we next sought to use this heating method for NAA. However, unlike open channel microfluidics, the porous high surface area characteristics of the paper provides significantly more opportunity for

unwanted non-specific adsorption to occur. Non-specific adsorption of proteins and enzymes to surfaces is a common obstacle to overcome in plate-based assays, DNA amplification, and Western blots. This non-specific adsorption can lead to non-functional assays and reduced DNA polymerase activity.[150–152] To prevent non-specific adsorption, a non-reactive carrier protein, typically BSA, is added to the reaction. This carrier protein out-competes enzymes for non-specific binding sites, allowing enzymes to proceed with the reaction. Passivation of NAA microstructures with BSA has been studied before where DNA amplification was performed in the presence of BSA and material typically used in microfluidics, showing that BSA helps to increase DNA yield from amplification.[151,153] Since paper is a highly porous structure with a large surface area-to-volume ratio, we hypothesized that this non-specific polymerase adsorption would occur during paper E-NAAMP and that treating paper with BSA prior to amplification would ensure continued polymerase activity. Previous work using LAMP reactions on paper have used BSA in the reaction mixture, however, the researchers did not comment on reasons for adding BSA to the LAMP reaction.[142,154,155]

To investigate potential polymerase adsorption within the paper, we performed a polymerase paper diffusion assay. We first prepared two different LAMP reactions to amplify λ DNA. One LAMP reaction, Reaction Set A, contained the polymerase, Bst 2.0. However, the second set, Reaction Set B, did not contain the Bst 2.0 polymerase. For the BSA diffusion assay, 2.5 mm^2 squares of both W1 and AM142 paper were laser cut and dipped in various w/v percentages of BSA solution: 0% (water), 0.1%, 0.5%, 1.0%, 2.0%, and 3.0%. Each of these paper substrates was then dried on a hot plate at 55 °C and loaded with polymerase by dipping them into a test tube containing 25 µL of

Reaction Set A for five minutes. The paper pieces were then transferred to another test tube containing 25 µL of Reaction Set B and incubated at 65 °C for 40 minutes in a T100 thermal cycler (Bio-Rad) to run LAMP. Additionally, 25 µL of the unaltered LAMP reaction (no paper or BSA) was incubated as well, as a positive control. All samples were then run on a 2% agarose gel, as previously described (Figure 5.4).

The diffusion assay quantitatively demonstrates the importance of BSA when designing LAMP reactions with W1 and AM142 paper. As shown in Figure 5.4(a) and 5.4(b), when both paper types were not treated with BSA (0% lanes), no DNA amplification occurred. However, with BSA treatment polymerase activity returns for both paper types, indicating that both paper types have an inhibitory effect upon LAMP. Work by Kodzius *et al.* has examined the adsorption and inhibition effect of common materials used in microfluidics on Taq polymerase (used in PCR) and showed that many materials can inhibit PCR activity, but such activity can be restored by adding BSA to the reaction mix. Their work suggests that a similar phenomenon likely occurs with the Bst 2.0 polymerase used in this work.[153] With BSA-treated paper channels, the non-specific adsorption sites would likely be unavailable and allows the Bst 2.0 polymerase to drive the LAMP reaction. As shown in Figure 5.4, both natural (W1) and synthetic (AM142) fiber paper exhibited this inhibitory effect, suggesting that this phenomenon occurs across multiple paper types commonly used in paper microfluidics. This adsorption phenomenon must therefore be considered when designing paper-based microfluidic amplification devices. If proper BSA and polymerase design is not factored into paper NAA devices, this could lead to diagnostic tests with a high degree of false negatives.

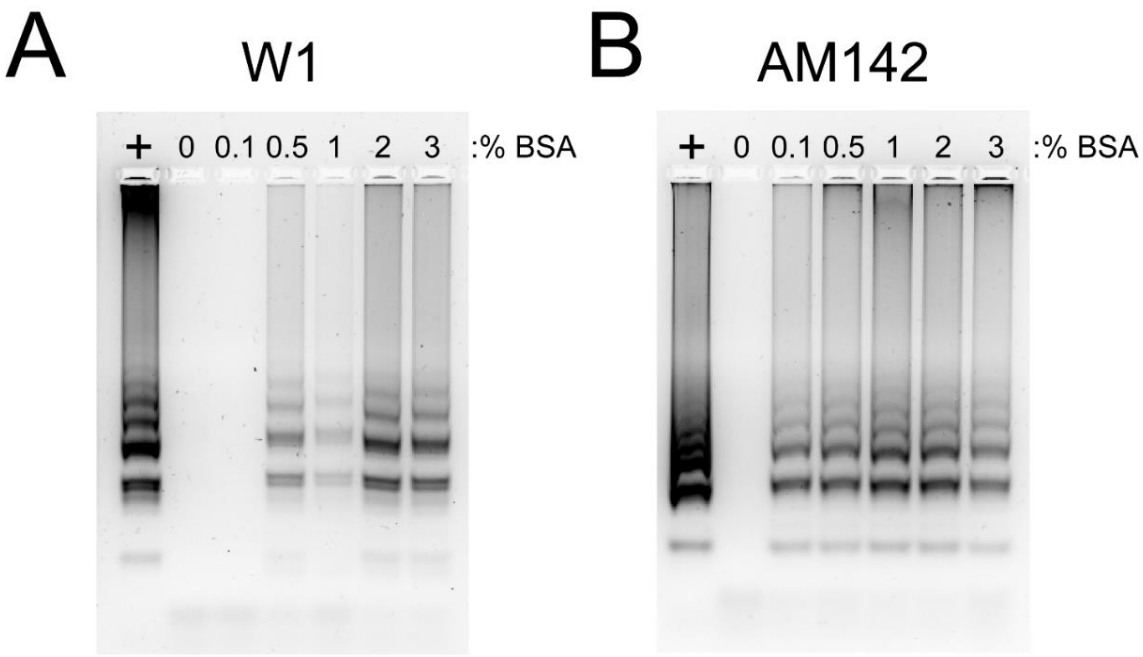

Figure 5.4 LAMP reaction and BSA interaction test on two paper types: (a) Whatman 1. (b) Ahlstrom-Munksjö Grade 142. Paper was treated with a BSA solution, soaked in a LAMP reaction containing Bst 2.0 polymerase, then transferred to a LAMP reaction with no polymerase and incubated at 65 °C for 40 minutes to amplify λ DNA.

5.4.3. E-NAAMP Using Paper Microfluidics

Finally, we used paper E-NAAMP to amplify λ DNA with LAMP. We first treated both paper types (W1 and AM142) with water or a 1% BSA solution in order to assess the importance of BSA with the E-NAAMP method. The water treatment served as the negative control. The devices were dried and fabricated using the µPiP process and filled with LAMP reaction mix. A high frequency 38-MHz voltage was applied across the conductive PDMS electrodes and monitored manually to maintain the target LAMP reaction temperature of 65 °C for 40 minutes. At the conclusion of the LAMP reaction the paper reaction chambers were extracted and analyzed on a 2% agarose gel. As shown in Figure 5.5, and as explained in the previous section, we observe that BSA treatment is necessary for successful E-NAAMP. This represents the first known

instance of DNA amplified using a paper microfluidic device driven by high-frequency Joule heating. Interestingly, we observe that E-NAAMP amplification products for AM142 run in a more streaky fashion on an agarose gel as compared to reactions amplified on a standard thermocycler, such as those seen in Figure 5.4 or W1 in Figure 5.5. The observed smear is not due to BSA because the SYBR Green I gel imaging fluorophore within the agarose gel solely interacts with DNA. Future work will focus on understanding why the E-NAAMP LAMP products appear different on a gel, as LAMP is commonly associated with distinct banding, as seen in Figure 5.4. W1, however, does not exhibit streaking and shows the distinct banding associated with LAMP. We also observe an amplicon level difference between W1 and AM142 that we attribute to inherent inconsistencies in device construction (by hand), leading to variations in performance from device to device. Figure 5.5 shows E-NAAMP's potential as a paper-based NAA method and demonstrates that E-NAAMP is compatible with both natural (W1) and glass synthetic (AM 142) paper types.

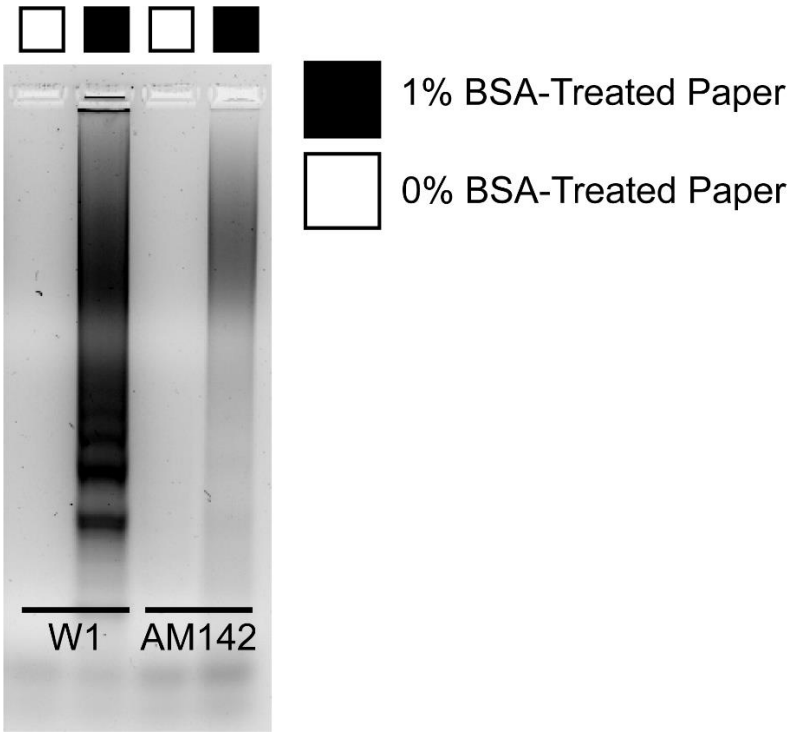

Figure 5.5 Paper E-NAAMP using two paper types, Whatman 1 & Ahlstrom-Munksjö Grade 142. Paper was either treated with a 1% BSA solution or water (0% BSA) prior to fabrication and operation.

5.5. Conclusions

In this work, we demonstrated the ability to utilize µPiP-based channels and porous paper substrates to perform NAA using Joule heating. µPiP is a viable alternative platform to perform E-NAAMP and to utilize a high-frequency voltage to heat NAA chambers using Joule heating. We demonstrated that successful amplification was accomplished using a pair of conductive PDMS-CB electrodes encased within two thin laminating sheets of PDMS. A NAA mix was driven into the paper channel and exposed to a high-frequency 38 MHz voltage to drive isothermal amplification by Joule heating. We experimentally measured and numerically investigated the voltage dependence on Joule heating temperatures that occur during paper E-NAAMP for two different paper types: natural fiber-based W1 and glassy fiber-based AM142. Experimental results were

compared with two-dimensional numerical simulations performed using COMSOL Multiphysics using 3D digital representations of the paper structures captured from three-dimensional micro-CT scans. We observed good agreement between the experimental and numerical Joule heating temperature curves, suggesting that Joule heating is the relevant heating mechanism for E-NAAMP on paper. We next investigated the role that non-specific adsorption plays when performing NAA on paper. We observed that the presence of the carrier protein, BSA was required for successful NAA within paper. Finally, we performed paper E-NAAMP using paper devices fabricated from both the natural W1 and synthetic AM142 paper devices, demonstrating that both NAA is possible in paper using the E-NAAMP method and that BSA treatment of the paper is required. Future work will focus on using a fluorescence or colorimetric-based LAMP mix for paper E-NAAMP, as this eliminates the need for time-consuming gel electrophoresis, which as seen in Figure 5, can sometimes run in a streaky fashion and can be aesthetically unpleasing. Additionally, future work will explore quantifying paper E-NAAMP amplification performance and providing comparisons to similar devices, rather than simply examining reaction success in a binary fashion, as shown in this work. Finally, given glass-based E-NAAMP's success running PCR, we envision paper E-NAAMP being able to run PCR as well, which will also be the subject of future work. This new paper-based NA platform addresses drawbacks of glass-based E-NAAMP by using inexpensive fabrication materials, not requiring clean rooms for fabrication, and producing devices less prone to breakage due to the rubbery nature of PDMS while still not requiring large external heating elements for the NA reactions.

6. CONCLUSIONS AND FUTURE WORK

6.1. Conclusions

In this work, we sought to improve microfluidics diagnostic platforms, particularly in the areas of sample preparation and biomarker detection. Many samples taken can't be immediately analyzed due to sample components that prevent detection (inhibitors, nucleic acid degradation enzymes, etc.).[6,7] These samples must be "cleaned up" and prepared for effective biomarker detection. A popular detection method, nucleic acid amplification, often relies on bulky heaters affixed to the undersides of microfluidic NAA devices, limiting portability and usability, and generating thermal gradients within the amplification reaction.[69,70]

We first used a novel electrokinetic technique, teíchophoresis, to concentrate and separate biomarkers. TPE concentrated avidin-FITC up to 6.6-fold when using a TE, separated BSA-AlexaFluor 555 and ovalbumin-fluorescein, and concentrated DNA up to 21-fold using a TE. Additionally, protein and DNA concentration factors were linear with respect to voltage, indicating that no pH changes occurred during operation as pH changes would have affected biomolecule mobility, producing non-linear voltage responses. Previous works have used batch ITP to concentrate biomarkers up to one million-fold for dyes, 60-fold for DNA, and up to 40-fold for proteins.[44,49,109] While TPE is not as effective at concentrating biomolecules as these other works, it does have the distinct advantage of lower voltage requirements, less fluidic handling due to the lack of an LE, and high sample throughput due to continuous operation.[10]

We then used another novel electrokinetic technique, E-NAAMP, to amplify nucleic acids using high-frequency voltage to generate Joule heating directly within the reaction. The E-NAAMP chip was fabricated in a clean room on a glass slide and used chrome and gold as electrode materials. This chip was then used to amplify DNA using both LAMP and PCR, using a colorimetric pH indicator and gel electrophoresis to confirm amplification. Joule-heated NAA has been accomplished previously, but these works generated gaseous byproducts and induced electroosmotic flow, leaving room for improvement. E-NAAMP generated no gas byproducts or pH changes, making it superior to previous Joule-heated NAA works.[71,127]

However, E-NAAMP is not without its limitations. It is fabricated upon flimsy glass slides, uses expensive materials for electrodes, and requires fabrication in a clean room environment. To improve E-NAAMP, it was adapted onto a new platform, µPiP. µPiP is a paper microfluidics platform that encapsulates paper channels within thin sheets of PDMS, preventing fluid evaporation during operation. Additionally, µPiP uses pressure rather than capillary action to drive fluid flow, allowing for faster flow rates through paper devices. µPiP devices for paper E-NAAMP were constructed with conductive PDMS-CB sheets as electrodes in contact with the paper channel. Two types of paper were analyzed, W1 (cellulose) and AM142 (glass). Experiments also showed that passivation with BSA was necessary for successful LAMP on paper, regardless of paper type. Finally, paper E-NAAMP was performed using LAMP, demonstrating the first instance of Joule-heated, paper-based NAA. While previous works have relied on hot plates and incubators to drive paper NAA, paper E-NAAMP utilizes built-in electrodes to supply heating directly to paper amplification reactions.[82,142,143]

These electrokinetic techniques, TPE and E-NAAMP, have allowed for improvements in the areas of sample preparation and biomarker detection, bringing the goal of an all-in-one diagnostic device closer to reality. The next section discusses further improvements that can be made to TPE and E-NAAMP in pursuit of that goal.

6.2. Future Work

Microfluidic diagnostics has many components, including sample preparation, chemical reactions, and biomarker detection. An eventual goal of this research is to produce an all-in-one diagnostic device where technologies presented in this work (TPE and E-NAAMP) work in series to make a complete and all-in-one workflow. This would involve extracting NAs using TPE, then flowing the concentrated NAs to the E-NAAMP zone to detect DNA biomarker presence. These processes would ideally be accomplished using paper microfluidics, in particular μPiP. This would decrease fabrication time, cost, and complexity. Developing a paper-based FFTPE device such that TPE-prepared NAs could flow to a paper E-NAAMP device, as depicted in Figure 6.1, is feasible since batch ITP has been previously accomplished using paper microfluidic devices and this work demonstrated the ability to perform NAA using paper E-NAAMP.[156–158] However, to eventually integrate these two processes into a single workflow, individual improvements to both traditional TPE and paper E-NAAMP are needed.

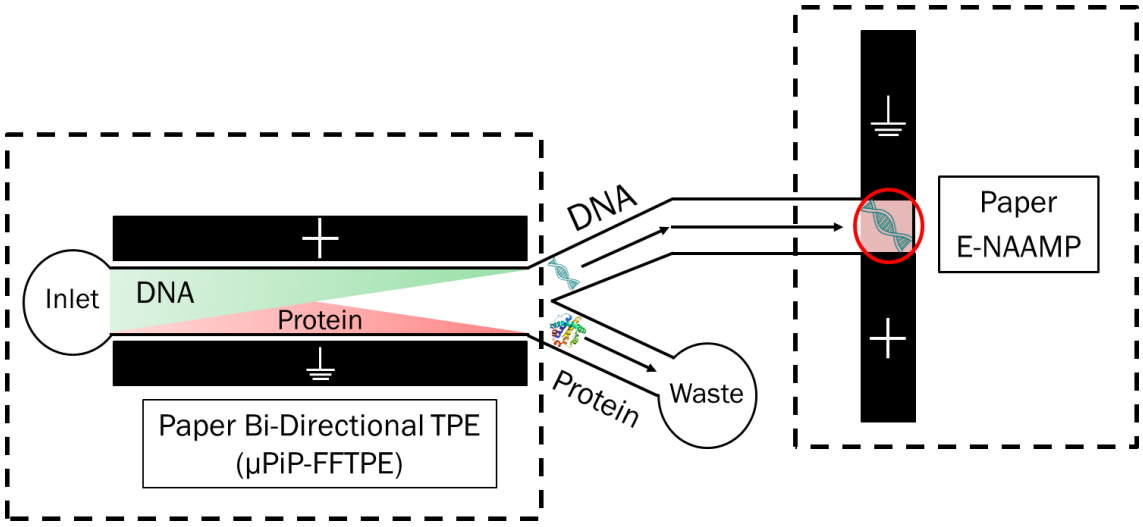

Figure 6.1 Long-term research goal: Bi-directional FFTPE and paper E-NAAMP using µPiP. Samples would be prepared by removing NAA inhibitors with FFTPE on paper. Concentrated NAs would then flow to the paper E-NAAMP zone where amplification would occur on-chip using a colorimetric LAMP mix.

One improvement would be to extract DNA from biological samples with a technique called bi-directional FFTPE. This would also require re-designing the microfluidic chip used in Section 3 to perform effortless sample extraction from the device (fractionation). Separating DNA biomarkers from potential contaminants, such as PCR inhibitors and other nucleic acid and proteome degradation enzymes, enables detection on platforms such as E-NAAMP. Bi-directional FFTPE and other improvements to the TPE system are expanded upon in Section 6.2.1.

The second improvement would be to the analysis techniques of paper E-NAAMP. While paper E-NAAMP successfully amplified DNA, analysis and confirmation currently relies on off-chip techniques, in particular gel electrophoresis. Gel electrophoresis involves breaking open the device, extracting the paper amplification zone, eluting DNA from the paper, and running the samples on an agarose gel, all of which is laborious, tedious, and time-consuming. One improvement that can

be made is to use a colorimetric LAMP mix, like the one used for glass-based E-NAAMP, seen in Section 4.5.2. Using a colorimetric LAMP mix enables on-chip detection of amplification, rather than relying on off-chip gel electrophoresis. Colorimetric paper E-NAAMP and its associated challenges are expanded upon in Section 6.2.2.

6.2.1. Bi-Directional TPE Separation of Protein and DNA

A recent innovation in the ITP field is bi-directional isotachophoresis, where two sets of electrolytes are used to separate analytes in opposite directions by exploiting opposite charge differences between two species. Traditional bi-directional ITP requires two sets of electrolytes, a TE and LE associated with each species to be separated, referred to as TE+, LE+, TE-, and LE. These four electrolytes act to simultaneously stack each desired species in opposite electric field directions. Bi-directional ITP is traditionally accomplished using a batch process, seen in the works of Bahga *et al*. and Qu *et al*., but has yet to be achieved in a continuous process.[52,53] Juan Santiago's group used batch bi-directional ITP to separate DNA (negatively charged) and protein (predominantly positively charged) in human serum. This removed protein NAA inhibitors from nucleic acids, allowing for off-chip amplification and detection of DNA, which was not possible due to PCR inhibitors present in human serum.[53]

Using the new FFTPE system, we hypothesize that bi-directional TPE, similar to bi-directional ITP, can be used to separate DNA and proteins continuously by replacing LE+ and LE- with conductive walls, much like single-species FFTPE, described in Section 3. This would occur by concentrating oppositely charged species against opposite channel walls using only TE's. Proteins, predominately positively charged,

would concentrate against the grounded conductive wall, and DNA, negatively charged, would concentrate against the positive conductive wall, with the two TE's in the middle of the channel.[10]

While on-chip analysis via fluorescence is an effective way to analyze concentration and separation, the ability to route concentrated samples via outlet fractionation would enable both off-chip analysis (qPCR for DNA and polyacrylamide gel electrophoresis (PAGE) for protein) and the stated goal of downstream on-chip analysis. Currently, the device pictured in Figure 3.1 does not produce even flow between the outlets, making sample extraction ineffective. A re-design of the TPE chip's outlet would enable effective fractionation. Effective outlet fractionation would allow for separation degree quantification between the separated species and the original sample.

6.2.2. Colorimetric Paper E-NAAMP

While paper E-NAAMP was achieve, current methods of evaluating paper E-NAAMP success rely on off-chip analysis, in particular agarose gel electrophoresis. This requires a time-consuming and laborious process of breaking open the device, extracting the paper, eluting DNA, and running the DNA sample on an agarose gel. A better method of analysis would be to use the colorimetric LAMP mix used in Section 4.5.2. That way, a simple color switch would be all that is required for reaction success indication. However, previous work has suggested that BSA presence can affect the pH of the low-buffer LAMP reaction mixture, causing a premature color change of phenol red, the pH indicator found in NEB's Colorimetric LAMP Mix.[155] Phenol red starts as pink in LAMP reactions and changes to yellow as the reaction progresses and pH

decreases. BSA's effect on pH is shown in Figure 6.2, where the pH of pre-amplification LAMP reactions decreases with increasing concentration of BSA within the mixture. BSA's effect on pH could prevent visual and on-chip analysis of LAMP success.

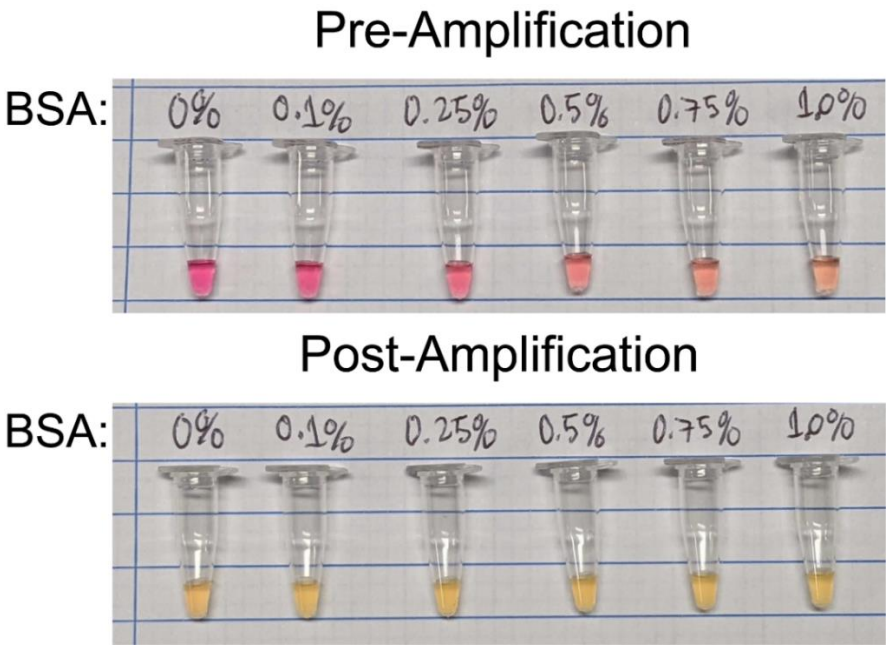

Figure 6.2 Colorimetric LAMP reaction with BSA. Pre-Amplification: pH decreases with increasing BSA concentration. Post-Amplification: Successful LAMP reaction, with final pH unaffected by BSA concentration.

Additionally, paper presence also affects the final pH of the reaction. Fig. 6.3 shows colorimetric LAMP reactions carried out in the presence of 2.5 mm^2 AM142 paper pieces soaked in various w/v% solutions of BSA. First shown in Figure 5.4, without BSA pretreatment, the LAMP was inhibited by paper presence. Fig. 6.3 also shows that when paper is pre-treated with BSA, polymerase activity returns, as expected based on Figure 5.4. However, when analyzing the colorimetric aspect of the reactions in Figure 6.3, the final color does not reach the same yellow color as the positive control (+), despite reaction success, indicating that paper presence affects final reaction pH. Additionally, when comparing the final color of the 0.1% reaction and the 3% reaction,

paper treated with lower percentages of BSA resulted in color that was closer to the pink displayed in the 0% BSA reaction, where little amplification occurred. These results, along with the results shown in Figure 6.2 suggest a complex relationship between paper presence, reaction pH, and BSA concentration. Fully understanding this relationship and engineering a µPiP device not susceptible to this relationship will enable on-chip analysis of LAMP using paper E-NAAMP and subsequent integration with paper-based FFTPE, achieving the goal of developing a paper-based and all-in-one diagnostic device.

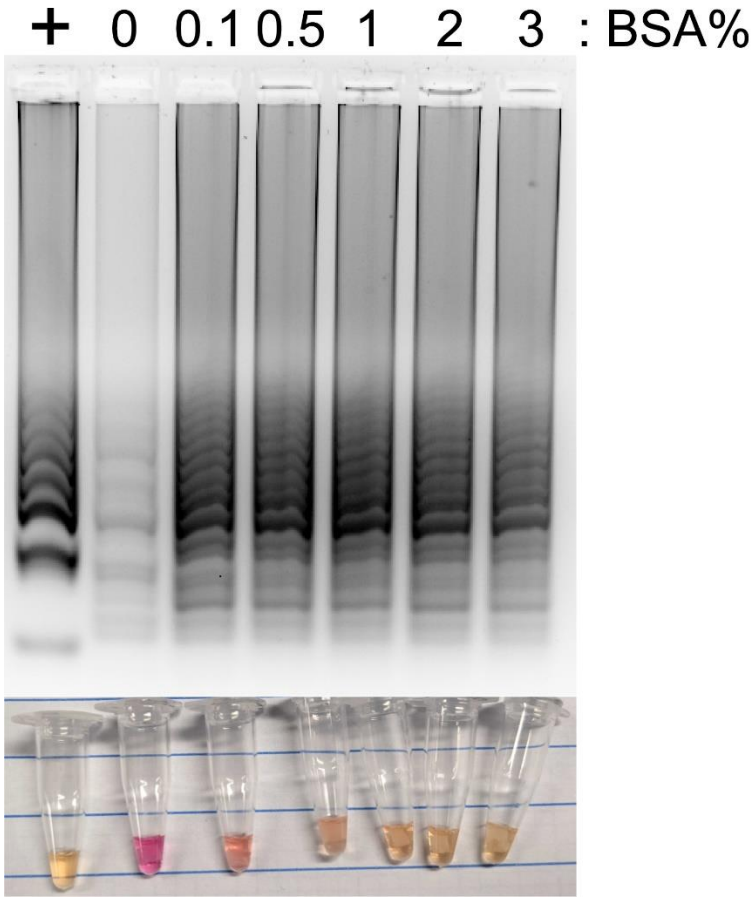

Figure 6.3 Colorimetric LAMP reaction in presence of BSA-soaked AM-142 paper. +: positive control LAMP reaction with no paper present.

REFERENCES

(1) Giri, B.; Pandey, S.; Shrestha, R.; Pokharel, K.; Ligler, F. S.; Neupane, B. B. Review of Analytical Performance of COVID-19 Detection Methods. *Anal. Bioanal. Chem.* **2021**, *413* (1), 35–48. https://doi.org/10.1007/s00216-020-02889-x.

(2) Santos, H.; Liu, D.; Zhang, H. *Microfluidics for Pharmaceutical Applications - 1st Edition*, 1st ed.; Elsevier, 2018.

(3) Huang, Y.; Mather, E. L.; Bell, J. L.; Madou, M. MEMS-Based Sample Preparation for Molecular Diagnostics. *Anal. Bioanal. Chem.* **2002**, *372* (1), 49–65. https://doi.org/10.1007/s00216-001-1191-9.

(4) Vuckovic, D. Current Trends and Challenges in Sample Preparation for Global Metabolomics Using Liquid Chromatography–Mass Spectrometry. *Anal. Bioanal. Chem.* **2012**, *403* (6), 1523–1548. https://doi.org/10.1007/s00216-012-6039-y.

(5) Cui, F.; Rhee, M.; Singh, A.; Tripathi, A. Microfluidic Sample Preparation for Medical Diagnostics. *Annu. Rev. Biomed. Eng.* **2015**, *17* (1), 267–286. https://doi.org/10.1146/annurev-bioeng-071114-040538.

(6) Rådström, P.; Löfström, C.; Lövenklev, M.; Knutsson, R.; Wolffs, P. Strategies for Overcoming PCR Inhibition. *Cold Spring Harb. Protoc.* **2008**, *2008* (3), pdb.top20. https://doi.org/10.1101/pdb.top20.

(7) Feist, P.; Hummon, A. B. Proteomic Challenges: Sample Preparation Techniques for Microgram-Quantity Protein Analysis from Biological Samples. *Int. J. Mol. Sci.* **2015**, *16* (2), 3537–3563. https://doi.org/10.3390/ijms16023537.

(8) Castellanos-Serra, L.; Paz-Lago, D. Inhibition of Unwanted Proteolysis during Sample Preparation: Evaluation of Its Efficiency in Challenge Experiments. *ELECTROPHORESIS* **2002**, *23* (11), 1745–1753. https://doi.org/10.1002/1522-2683(200206)23:11<1745::AID-ELPS1745>3.0.CO;2-A.

(9) Park, S.; Zhang, Y.; Lin, S.; Wang, T.-H.; Yang, S. Advances in Microfluidic PCR for Point-of-Care Infectious Disease Diagnostics. *Biotechnol. Adv.* **2011**, *29* (6), 830–839. https://doi.org/10.1016/j.biotechadv.2011.06.017.

(10) Doria, S.; Gagnon, Z. Continuous Molecular Concentration and Separation Using Pulsed-Field Conductive-Wall Single-Buffer Teíchophoresis. *Anal. Chem.* **2022**, *94* (39), 13481–13488. https://doi.org/10.1021/acs.analchem.2c02608.

(11) Doria, S.; Yost, J.; Gagnon, Z. Free-Flow Biomolecular Concentration and Separation of Proteins and Nucleic Acids Using Teíchophoresis. *Talanta* **2023**, *255*, 124198. https://doi.org/10.1016/j.talanta.2022.124198.

(12) Yost, J.; Gagnon, Z. Faradaic-Free Electrokinetic Nucleic Acid Amplification (E-NAAMP) Using Localized on-Chip High Frequency Joule Heating. *Biomicrofluidics* **2022**, *16* (1), 014101. https://doi.org/10.1063/5.0072198.

(13) Nazibul Islam, M.; W. Yost, J.; R. Gagnon, Z. Microfluidic Pressure in Paper (MPiP): Rapid Prototyping and Low-Cost Liquid Handling for on-Chip Diagnostics. *Analyst* **2022**, *147* (4), 587–596. https://doi.org/10.1039/D1AN01676H.

(14) Duffy, D. C.; McDonald, J. C.; Schueller, O. J. A.; Whitesides, G. M. Rapid Prototyping of Microfluidic Systems in Poly(Dimethylsiloxane). *Anal. Chem.* **1998**, *70* (23), 4974–4984. https://doi.org/10.1021/ac980656z.

(15) Matuła, K.; Rivello, F.; Huck, W. T. S. Single-Cell Analysis Using Droplet Microfluidics. *Adv. Biosyst.* **2020**, *4* (1), 1900188. https://doi.org/10.1002/adbi.201900188.
(16) Vyawahare, S.; Griffiths, A. D.; Merten, C. A. Miniaturization and Parallelization of Biological and Chemical Assays in Microfluidic Devices. *Chem. Biol.* **2010**, *17* (10), 1052–1065. https://doi.org/10.1016/j.chembiol.2010.09.007.
(17) Bhattacharjee, N.; Urrios, A.; Kang, S.; Folch, A. The Upcoming 3D-Printing Revolution in Microfluidics. *Lab. Chip* **2016**, *16* (10), 1720–1742. https://doi.org/10.1039/C6LC00163G.
(18) Goral, V. N.; Hsieh, Y.-C.; Petzold, O. N.; Faris, R. A.; Yuen, P. K. Hot Embossing of Plastic Microfluidic Devices Using Poly(Dimethylsiloxane) Molds. *J. Micromechanics Microengineering* **2010**, *21* (1), 017002. https://doi.org/10.1088/0960-1317/21/1/017002.
(19) Romoli, L.; Tantussi, G.; Dini, G. Experimental Approach to the Laser Machining of PMMA Substrates for the Fabrication of Microfluidic Devices. *Opt. Lasers Eng.* **2011**, *49* (3), 419–427. https://doi.org/10.1016/j.optlaseng.2010.11.013.
(20) Sinkala, E.; Sollier-Christen, E.; Renier, C.; Rosàs-Canyelles, E.; Che, J.; Heirich, K.; Duncombe, T. A.; Vlassakis, J.; Yamauchi, K. A.; Huang, H.; Jeffrey, S. S.; Herr, A. E. Profiling Protein Expression in Circulating Tumour Cells Using Microfluidic Western Blotting. *Nat. Commun.* **2017**, *8* (1), 14622. https://doi.org/10.1038/ncomms14622.
(21) Zhang, C.; Xu, J.; Ma, W.; Zheng, W. PCR Microfluidic Devices for DNA Amplification. *Biotechnol. Adv.* **2006**, *24* (3), 243–284. https://doi.org/10.1016/j.biotechadv.2005.10.002.
(22) Sandlin, Z. D.; Shou, M.; Shackman, J. G.; Kennedy, R. T. Microfluidic Electrophoresis Chip Coupled to Microdialysis for in Vivo Monitoring of Amino Acid Neurotransmitters. *Anal. Chem.* **2005**, *77* (23), 7702–7708. https://doi.org/10.1021/ac051044z.
(23) J. Meagher, R.; K. Light, Y.; K. Singh, A. Rapid, Continuous Purification of Proteins in a Microfluidic Device Using Genetically-Engineered Partition Tags. *Lab. Chip* **2008**, *8* (4), 527–532. https://doi.org/10.1039/B716462A.
(24) Lagally, E. T.; Simpson, P. C.; Mathies, R. A. Monolithic Integrated Microfluidic DNA Amplification and Capillary Electrophoresis Analysis System. *Sens. Actuators B Chem.* **2000**, *63* (3), 138–146. https://doi.org/10.1016/S0925-4005(00)00350-6.
(25) Janasek, D.; Schilling, M.; Franzke, J.; Manz, A. Isotachophoresis in Free-Flow Using a Miniaturized Device. *Anal. Chem.* **2006**, *78* (11), 3815–3819. https://doi.org/10.1021/ac060063l.
(26) Everaerts, F. M.; Beckers, J. L.; Verheggen, T. P. E. M. *Isotachophoresis: Theory, Instrumentation and Applications*; Elsevier, 2011.
(27) *gel electrophoresis | Learn Science at Scitable*. https://www.nature.com/scitable/definition/gel-electrophoresis-286/ (accessed 2020-02-08).
(28) Dorfman, K. D.; King, S. B.; Olson, D. W.; Thomas, J. D. P.; Tree, D. R. Beyond Gel Electrophoresis: Microfluidic Separations, Fluorescence Burst Analysis, and

DNA Stretching. *Chem. Rev.* **2013**, *113* (4), 2584–2667. https://doi.org/10.1021/cr3002142.
(29) Monnig, C. A.; Kennedy, R. T. Capillary Electrophoresis. *Anal. Chem.* **1994**, *66* (12), 280–314. https://doi.org/10.1021/ac00084a013.
(30) Bazant, M. Z. Induced-Charge Electrokinetic Phenomena. 75.
(31) Ai, Y.; Park, S.; Zhu, J.; Xuan, X.; Beskok, A.; Qian, S. DC Electrokinetic Particle Transport in an L-Shaped Microchannel. *Langmuir* **2010**, *26* (4), 2937–2944. https://doi.org/10.1021/la902711x.
(32) D. Velev, O.; Gangwal, S.; N. Petsev, D. Particle-Localized AC and DC Manipulation and Electrokinetics. *Annu. Rep. Sect. C Phys. Chem.* **2009**, *105* (0), 213–246. https://doi.org/10.1039/B803015B.
(33) Green, N. G.; Ramos, A.; Morgan, H. Ac Electrokinetics: A Survey of Sub-Micrometre Particle Dynamics. *J. Phys. Appl. Phys.* **2000**, *33* (6), 632–641. https://doi.org/10.1088/0022-3727/33/6/308.
(34) Hughes, M. P. AC Electrokinetics: Applications for Nanotechnology. *Nanotechnology* **2000**, *11* (2), 124–132. https://doi.org/10.1088/0957-4484/11/2/314.
(35) Ramos, A.; Morgan, H.; Green, N. G.; Castellanos, A. Ac Electrokinetics: A Review of Forces in Microelectrode Structures. *J. Phys. Appl. Phys.* **1998**, *31* (18), 2338–2353. https://doi.org/10.1088/0022-3727/31/18/021.
(36) Xuan, X. Joule Heating in Electrokinetic Flow. *ELECTROPHORESIS* **2008**, *29* (1), 33–43. https://doi.org/10.1002/elps.200700302.
(37) Cetin, B.; Li, D. Effect of Joule Heating on Electrokinetic Transport. *ELECTROPHORESIS* **2008**, *29* (5), 994–1005. https://doi.org/10.1002/elps.200700601.
(38) Rush, R. S.; Cohen, A. S.; Karger, B. L. Influence of Column Temperature on the Electrophoretic Behavior of Myoglobin and .Alpha.-Lactalbumin in High-Performance Capillary Electrophoresis. *Anal. Chem.* **1991**, *63* (14), 1346–1350. https://doi.org/10.1021/ac00014a002.
(39) Morgan, H.; Green, N. G. *AC Electrokinetics: Colloids and Nanoparticles*; Microtechnologies and microsystems series; Research Studies Press: Baldock, 2003.
(40) Křivánková, L.; Pantůčková, P.; Boček, P. Isotachophoresis in Zone Electrophoresis. *J. Chromatogr. A* **1999**, *838* (1), 55–70. https://doi.org/10.1016/S0021-9673(99)00169-7.
(41) Smejkal, P.; Bottenus, D.; Breadmore, M. C.; Guijt, R. M.; Ivory, C. F.; Foret, F.; Macka, M. Microfluidic Isotachophoresis: A Review. *ELECTROPHORESIS* **2013**, *34* (11), 1493–1509. https://doi.org/10.1002/elps.201300021.
(42) Khurana, T. K.; Santiago, J. G. Sample Zone Dynamics in Peak Mode Isotachophoresis. *Anal. Chem.* **2008**, *80* (16), 6300–6307. https://doi.org/10.1021/ac800792g.
(43) V. Kaigala, G.; Bercovici, M.; Behnam, M.; Elliott, D.; G. Santiago, J.; J. Backhouse, C. Miniaturized System for Isotachophoresis Assays. *Lab. Chip* **2010**, *10* (17), 2242–2250. https://doi.org/10.1039/C004120C.

(44) Jung, B.; Bharadwaj, R.; Santiago, J. G. On-Chip Millionfold Sample Stacking Using Transient Isotachophoresis. *Anal. Chem.* **2006**, *78* (7), 2319–2327. https://doi.org/10.1021/ac051659w.
(45) Garcia-Schwarz, G.; Rogacs, A.; Bahga, S. S.; Santiago, J. G. On-Chip Isotachophoresis for Separation of Ions and Purification of Nucleic Acids. *J. Vis. Exp. JoVE* **2012**, No. 61, e3890. https://doi.org/10.3791/3890.
(46) Persat, A.; Marshall, L. A.; Santiago, J. G. Purification of Nucleic Acids from Whole Blood Using Isotachophoresis. *Anal. Chem.* **2009**, *81* (22), 9507–9511. https://doi.org/10.1021/ac901965v.
(47) Kondratova, V. N.; Serd'uk, O. I.; Shelepov, V. P.; Lichtenstein, A. V. Concentration and Isolation of DNA from Biological Fluids by Agarose Gel Isotachophoresis. *BioTechniques* **2005**, *39* (5), 695–699. https://doi.org/10.2144/000112020.
(48) Acevedo, F. Isotachophoresis of Proteins. *J. Chromatogr. A* **1989**, *470* (2), 407–414. https://doi.org/10.1016/S0021-9673(01)83569-X.
(49) Cui, H.; Dutta, P.; Ivory, C. F. Isotachophoresis of Proteins in a Networked Microfluidic Chip: Experiment and 2-D Simulation. *ELECTROPHORESIS* **2007**, *28* (7), 1138–1145. https://doi.org/10.1002/elps.200600525.
(50) Acevedo, F. Use of Discrete Spacers for the Separation of Proteins by Gel Isotachophoresis. *J. Chromatogr. A* **1991**, *545* (2), 391–396. https://doi.org/10.1016/S0021-9673(01)88731-8.
(51) Schoch, R. B.; Ronaghi, M.; Santiago, J. G. Rapid and Selective Extraction, Isolation, Preconcentration, and Quantitation of Small RNAs from Cell Lysate Using on-Chip Isotachophoresis. *Lab. Chip* **2009**, *9* (15), 2145–2152. https://doi.org/10.1039/b903542g.
(52) Bahga, S. S.; Chambers, R. D.; Santiago, J. G. Coupled Isotachophoretic Preconcentration and Electrophoretic Separation Using Bidirectional Isotachophoresis. *Anal. Chem.* **2011**, *83* (16), 6154–6162. https://doi.org/10.1021/ac200268f.
(53) Qu, Y.; Marshall, L. A.; Santiago, J. G. Simultaneous Purification and Fractionation of Nucleic Acids and Proteins from Complex Samples Using Bidirectional Isotachophoresis. *Anal. Chem.* **2014**, *86* (15), 7264–7268. https://doi.org/10.1021/ac501299a.
(54) Turgeon, R. T.; Bowser, M. T. Micro Free-Flow Electrophoresis: Theory and Applications. *Anal. Bioanal. Chem.* **2009**, *394* (1), 187–198. https://doi.org/10.1007/s00216-009-2656-5.
(55) Fu, X.; Mavrogiannis, N.; Ibo, M.; Crivellari, F.; Gagnon, Z. R. Microfluidic Free-Flow Zone Electrophoresis and Isotachophoresis Using Carbon Black Nano-Composite PDMS Sidewall Membranes. *ELECTROPHORESIS* **2017**, *38* (2), 327–334. https://doi.org/10.1002/elps.201600104.
(56) Prest, J. E.; Baldock, S. J.; Fielden, P. R.; Goddard, N. J.; Goodacre, R.; O'Connor, R.; Treves Brown, B. J. Miniaturised Free Flow Isotachophoresis of Bacteria Using an Injection Moulded Separation Device. *J. Chromatogr. B* **2012**, *903*, 53–59. https://doi.org/10.1016/j.jchromb.2012.06.040.
(57) Park, J. K.; Campos, C. D. M.; Neužil, P.; Abelmann, L.; Guijt, R. M.; Manz, A. Direct Coupling of a Free-Flow Isotachophoresis (FFITP) Device with

Electrospray Ionization Mass Spectrometry (ESI-MS). *Lab. Chip* **2015**, *15* (17), 3495–3502. https://doi.org/10.1039/C5LC00523J.
(58) Joule, J. P. *The Scientific Papers of James Prescott Joule*; Cambridge University Press, 2011.
(59) Sastry, S. K.; Barach, J. T. Ohmic and Inductive Heating. *J. Food Sci.* **2000**, *65* (s8), 42–46. https://doi.org/10.1111/j.1750-3841.2000.tb00617.x.
(60) Li, L.; Chew, Z. J. 11 - Microactuators: Design and Technology. In *Smart Sensors and Mems*; Nihtianov, S., Luque, A., Eds.; Woodhead Publishing, 2014; pp 305–348. https://doi.org/10.1533/9780857099297.2.305.
(61) Imai, T.; Uemura, K.; Ishida, N.; Yoshizaki, S.; Noguchi, A. Ohmic Heating of Japanese White Radish Rhaphanus Sativus L. *Int. J. Food Sci. Technol.* **1995**, *30* (4), 461–472. https://doi.org/10.1111/j.1365-2621.1995.tb01393.x.
(62) Wei, J.; Zhu, H.; Wu, D.; Wei, B. Carbon Nanotube Filaments in Household Light Bulbs. *Appl. Phys. Lett.* **2004**, *84* (24), 4869–4871. https://doi.org/10.1063/1.1762697.
(63) Xuan, X.; Li, D. Joule Heating in Electrokinetic Flow: Theoretical Models. In *Encyclopedia of Microfluidics and Nanofluidics*; Li, D., Ed.; Springer US: Boston, MA, 2008; pp 896–905. https://doi.org/10.1007/978-0-387-48998-8_760.
(64) Mullis, K.; Faloona, F.; Scharf, S.; Saiki, R.; Horn, G.; Erlich, H. Specific Enzymatic Amplification of DNA In Vitro: The Polymerase Chain Reaction. *Cold Spring Harb. Symp. Quant. Biol.* **1986**, *51*, 263–273. https://doi.org/10.1101/SQB.1986.051.01.032.
(65) Higuchi, R.; Fockler, C.; Dollinger, G.; Watson, R. Kinetic PCR Analysis: Real-Time Monitoring of DNA Amplification Reactions. *Biotechnol. Nat. Publ. Co.* **1993**, *11* (9), 1026–1030.
(66) Nagamine, K.; Hase, T.; Notomi, T. Accelerated Reaction by Loop-Mediated Isothermal Amplification Using Loop Primers. *Mol. Cell. Probes* **2002**, *16* (3), 223–229.
(67) Notomi, T.; Okayama, H.; Masubuchi, H.; Yonekawa, T.; Watanabe, K.; Amino, N.; Hase, T. Loop-Mediated Isothermal Amplification of DNA. *Nucleic Acids Res.* **2000**, *28* (12), e63.
(68) Chen, J.; Wabuyele, M.; Chen, H.; Patterson, D.; Hupert, M.; Shadpour, H.; Nikitopoulos, D.; Soper, S. A. Electrokinetically Synchronized Polymerase Chain Reaction Microchip Fabricated in Polycarbonate. *Anal. Chem.* **2005**, *77* (2), 658–666. https://doi.org/10.1021/ac048758e.
(69) D. Ahrberg, C.; Robert Ilic, B.; Manz, A.; Neužil, P. Handheld Real-Time PCR Device. *Lab. Chip* **2016**, *16* (3), 586–592. https://doi.org/10.1039/C5LC01415H.
(70) Kopp, M. U.; Mello, A. J. de; Manz, A. Chemical Amplification: Continuous-Flow PCR on a Chip. *Science* **1998**, *280* (5366), 1046–1048. https://doi.org/10.1126/science.280.5366.1046.
(71) Hu, G.; Xiang, Q.; Fu, R.; Xu, B.; Venditti, R.; Li, D. Electrokinetically Controlled Real-Time Polymerase Chain Reaction in Microchannel Using Joule Heating Effect. *Anal. Chim. Acta* **2006**, *557* (1), 146–151. https://doi.org/10.1016/j.aca.2005.10.021.

(72) Martinez, A. W.; Phillips, S. T.; Butte, M. J.; Whitesides, G. M. Patterned Paper as a Platform for Inexpensive, Low-Volume, Portable Bioassays. *Angew. Chem. Int. Ed Engl.* **2007**, *46* (8), 1318–1320. https://doi.org/10.1002/anie.200603817.
(73) von Lode, P. Point-of-Care Immunotesting: Approaching the Analytical Performance of Central Laboratory Methods. *Clin. Biochem.* **2005**, *38* (7), 591–606. https://doi.org/10.1016/j.clinbiochem.2005.03.008.
(74) Magro, L.; Escadafal, C.; Garneret, P.; Jacquelin, B.; Kwasiborski, A.; Manuguerra, J.-C.; Monti, F.; Sakuntabhai, A.; Vanhomwegen, J.; Lafaye, P.; Tabeling, P. Paper Microfluidics for Nucleic Acid Amplification Testing (NAAT) of Infectious Diseases. *Lab. Chip* **2017**, *17* (14), 2347–2371. https://doi.org/10.1039/C7LC00013H.
(75) Martinez, A. W.; Phillips, S. T.; Whitesides, G. M.; Carrilho, E. Diagnostics for the Developing World: Microfluidic Paper-Based Analytical Devices. *Anal. Chem.* **2010**, *82* (1), 3–10. https://doi.org/10.1021/ac9013989.
(76) Coste, A. T.; Jaton, K.; Papadimitriou-Olivgeris, M.; Greub, G.; Croxatto, A. Comparison of SARS-CoV-2 Serological Tests with Different Antigen Targets. *J. Clin. Virol.* **2021**, *134*, 104690. https://doi.org/10.1016/j.jcv.2020.104690.
(77) Washburn, E. W. The Dynamics of Capillary Flow. *Phys. Rev.* **1921**, *17* (3), 273–283. https://doi.org/10.1103/PhysRev.17.273.
(78) Liu, Z.; Hu, J.; Zhao, Y.; Qu, Z.; Xu, F. Experimental and Numerical Studies on Liquid Wicking into Filter Papers for Paper-Based Diagnostics. *Appl. Therm. Eng.* **2015**, *88*, 280–287. https://doi.org/10.1016/j.applthermaleng.2014.09.057.
(79) Fries, N. *Capillary transport processes in porous materials - experiment and model*, 1. Aufl.; Cuvillier: Göttingen, 2010.
(80) Jahanshahi-Anbuhi, S.; Henry, A.; Leung, V.; Sicard, C.; Pennings, K.; Pelton, R.; D. Brennan, J.; M. Filipe, C. D. Paper-Based Microfluidics with an Erodible Polymeric Bridge Giving Controlled Release and Timed Flow Shutoff. *Lab. Chip* **2014**, *14* (1), 229–236. https://doi.org/10.1039/C3LC50762A.
(81) Gan, W.; Zhuang, B.; Zhang, P.; Han, J.; Li, C.-X.; Liu, P. A Filter Paper-Based Microdevice for Low-Cost, Rapid, and Automated DNA Extraction and Amplification from Diverse Sample Types. *Lab. Chip* **2014**, *14* (19), 3719–3728. https://doi.org/10.1039/C4LC00686K.
(82) Rohrman, B. A.; Richards-Kortum, R. R. A Paper and Plastic Device for Performing Recombinase Polymerase Amplification of HIV DNA. *Lab. Chip* **2012**, *12* (17), 3082–3088. https://doi.org/10.1039/C2LC40423K.
(83) Obaldia, N. Determinants of Low Socio-Economic Status and Risk of Plasmodium Vivax Malaria Infection in Panama (2009-2012): A Case-Control Study. *Malar. J.* **2015**, *14*, 14. https://doi.org/10.1186/s12936-014-0529-7.
(84) Shetty, P.; Ghosh, D.; Singh, M.; Tripathi, A.; Paul, D. Rapid Amplification of Mycobacterium Tuberculosis DNA on a Paper Substrate. *RSC Adv.* **2016**, *6* (61), 56205–56212. https://doi.org/10.1039/C6RA07529K.
(85) Liu, C.; Geva, E.; Mauk, M.; Qiu, X.; Abrams, W. R.; Malamud, D.; Curtis, K.; Owen, S. M.; Bau, H. H. An Isothermal Amplification Reactor with an Integrated Isolation Membrane for Point-of-Care Detection of Infectious Diseases. *Analyst* **2011**, *136* (10), 2069–2076. https://doi.org/10.1039/C1AN00007A.

(86) Choi, J. R.; Hu, J.; Tang, R.; Gong, Y.; Feng, S.; Ren, H.; Wen, T.; Li, X.; Abas, W. A. B. W.; Pingguan-Murphy, B.; Xu, F. An Integrated Paper-Based Sample-to-Answer Biosensor for Nucleic Acid Testing at the Point of Care. *Lab. Chip* **2016**, *16* (3), 611–621. https://doi.org/10.1039/C5LC01388G.
(87) Linnes, J. C.; Rodriguez, N. M.; Liu, L.; Klapperich, C. M. Polyethersulfone Improves Isothermal Nucleic Acid Amplification Compared to Current Paper-Based Diagnostics. *Biomed. Microdevices* **2016**, *18* (2), 30. https://doi.org/10.1007/s10544-016-0057-z.
(88) Pollock, N. R.; Rolland, J. P.; Kumar, S.; Beattie, P. D.; Jain, S.; Noubary, F.; Wong, V. L.; Pohlmann, R. A.; Ryan, U. S.; Whitesides, G. M. A Paper-Based Multiplexed Transaminase Test for Low-Cost, Point-of-Care Liver Function Testing. *Sci. Transl. Med.* **2012**, *4* (152), 152ra129. https://doi.org/10.1126/scitranslmed.3003981.
(89) Prest, J. E.; Beardah, M. S.; Baldock, S. J.; Doyle, S. P.; Fielden, P. R.; Goddard, N. J.; Brown, B. J. T. Determination of the Potassium Content of Explosive Residues Using Miniaturised Isotachophoresis. *Electrophoresis* **2010**, *31* (22), 3775–3782. https://doi.org/10.1002/elps.201000263.
(90) Wang, J.; Chatrathi, M. P.; Collins, G. E. Simultaneous Microchip Enzymatic Measurements of Blood Lactate and Glucose. *Anal. Chim. Acta* **2007**, *585* (1), 11–16. https://doi.org/10.1016/j.aca.2006.12.001.
(91) Wheeler, A. R.; Throndset, W. R.; Whelan, R. J.; Leach, A. M.; Zare, R. N.; Liao, Y. H.; Farrell, K.; Manger, I. D.; Daridon, A. Microfluidic Device for Single-Cell Analysis. *Anal. Chem.* **2003**, *75* (14), 3581–3586. https://doi.org/10.1021/ac0340758.
(92) Vitorino, R.; Guedes, S.; da Costa, J. P.; Kašička, V. Microfluidics for Peptidomics, Proteomics, and Cell Analysis. *Nanomaterials* **2021**, *11* (5), 1118. https://doi.org/10.3390/nano11051118.
(93) Wilding, P.; Shoffner, M. A.; Kricka, L. J. PCR in a Silicon Microstructure. *Clin. Chem.* **1994**, *40* (9), 1815–1818. https://doi.org/10.1093/clinchem/40.9.1815.
(94) Ibrahim, M. S.; Lofts, R. S.; Jahrling, P. B.; Henchal, E. A.; Weedn, V. W.; Northrup, M. A.; Belgrader, P. Real-Time Microchip PCR for Detecting Single-Base Differences in Viral and Human DNA. *Anal. Chem.* **1998**, *70* (9), 2013–2017. https://doi.org/10.1021/ac971091u.
(95) Yakovleva, J.; Davidsson, R.; Bengtsson, M.; Laurell, T.; Emnéus, J. Microfluidic Enzyme Immunosensors with Immobilised Protein A and G Using Chemiluminescence Detection. *Biosens. Bioelectron.* **2003**, *19* (1), 21–34. https://doi.org/10.1016/s0956-5663(03)00126-x.
(96) Fernández-Baldo, M. A.; Ortega, F. G.; Pereira, S. V.; Bertolino, F. A.; Serrano, M. J.; Lorente, J. A.; Raba, J.; Messina, G. A. Nanostructured Platform Integrated into a Microfluidic Immunosensor Coupled to Laser-Induced Fluorescence for the Epithelial Cancer Biomarker Determination. *Microchem. J.* **2016**, *128*, 18–25. https://doi.org/10.1016/j.microc.2016.03.012.
(97) Dixon, C.; Lamanna, J.; Wheeler, A. R. Direct Loading of Blood for Plasma Separation and Diagnostic Assays on a Digital Microfluidic Device. *Lab. Chip* **2020**, *20* (10), 1845–1855. https://doi.org/10.1039/D0LC00302F.

(98) Tian, Y.; Zhou, Y.; Elliott, S.; Aebersold, R.; Zhang, H. Solid-Phase Extraction of N-Linked Glycopeptides. *Nat. Protoc.* **2007**, *2* (2), 334–339. https://doi.org/10.1038/nprot.2007.42.
(99) Jorgenson, J. W.; Lukacs, K. D. Capillary Zone Electrophoresis. *Science* **1983**, *222* (4621), 266–272. https://doi.org/10.1126/science.6623076.
(100) Sullivan, B. P.; Bender, A. T.; Ngyuen, D. N.; Zhang, J. Y.; Posner, J. D. Nucleic Acid Sample Preparation from Whole Blood in a Paper Microfluidic Device Using Isotachophoresis. *J. Chromatogr. B* **2021**, *1163*, 122494. https://doi.org/10.1016/j.jchromb.2020.122494.
(101) Gascoyne, P.; Mahidol, C.; Ruchirawat, M.; Satayavivad, J.; Watcharasit, P.; Becker, F. F. Microsample Preparation by Dielectrophoresis: Isolation of Malaria. *Lab. Chip* **2002**, *2* (2), 70–75. https://doi.org/10.1039/b110990c.
(102) Papadimitriou, V. A.; Segerink, L. I.; Eijkel, J. C. T. Free Flow Ion Concentration Polarization Focusing (FF-ICPF). *Anal. Chem.* **2020**, *92* (7), 4866–4874. https://doi.org/10.1021/acs.analchem.9b04526.
(103) Oukacine, F.; Garrelly, L.; Romestand, B.; Goodall, D. M.; Zou, T.; Cottet, H. Focusing and Mobilization of Bacteria in Capillary Electrophoresis. *Anal. Chem.* **2011**, *83* (5), 1571–1578. https://doi.org/10.1021/ac1023815.
(104) Takehara, H.; Sato, S.; Ichiki, T. All-Polymer-Based Micro Free-Flow Electrophoresis (MFFE) Device with Cellulose Permeable Membranes. *Appl. Phys. Express* **2019**, *12* (10), 107001. https://doi.org/10.7567/1882-0786/ab3d64.
(105) Ashrafizadeh, S. N.; Seifollahi, Z.; Ganjizade, A.; Sadeghi, A. Electrophoresis of Spherical Soft Particles in Electrolyte Solutions: A Review. *ELECTROPHORESIS* **2020**, *41* (1–2), 81–103. https://doi.org/10.1002/elps.201900236.
(106) Fang, X.; Wang, W.; Yang, L.; Chandrasekaran, K.; Kristian, T.; Balgley, B. M.; Lee, C. S. Application of Capillary Isotachophoresis-Based Multidimensional Separations Coupled with Electrospray Ionization-Tandem Mass Spectrometry for Characterization of Mouse Brain Mitochondrial Proteome. *Electrophoresis* **2008**, *29* (10), 2215–2223. https://doi.org/10.1002/elps.200700609.
(107) Danger, G.; Ross, D. Chiral Separation with Gradient Elution Isotachophoresis for Future in Situ Extraterrestrial Analysis. *Electrophoresis* **2008**, *29* (19), 4036–4044. https://doi.org/10.1002/elps.200700950.
(108) Kubacák, P.; Mikus, P.; Valásková, I.; Havránek, E. Chiral Separation of Alkylamine Antihistamines in Pharmaceuticals by Capillary Isotachophoresis with Charged Cyclodextrin. *Drug Dev. Ind. Pharm.* **2007**, *33* (11), 1199–1204. https://doi.org/10.1080/03639040701377565.
(109) Wang, J.; Zhang, Y.; Okamoto, Y.; Kaji, N.; Tokeshi, M.; Baba, Y. Online Transient Isotachophoresis Concentration by the Pseudo-Terminating Electrolyte Buffer for the Separation of DNA–Aptamer and Its Thrombin Complex in Poly(Methyl Methacrylate) Microchip. *Analyst* **2011**, *136* (6), 1142–1147. https://doi.org/10.1039/C0AN00434K.
(110) Bercovici, M.; Han, C. M.; Liao, J. C.; Santiago, J. G. Rapid Hybridization of Nucleic Acids Using Isotachophoresis. *Proc. Natl. Acad. Sci.* **2012**, *109* (28), 11127–11132. https://doi.org/10.1073/pnas.1205004109.

(111) Zhao, W.; Yang, R. Pulsed Electric Field Induced Aggregation of Food Proteins: Ovalbumin and Bovine Serum Albumin. *Food Bioprocess Technol.* **2012**, *5* (5), 1706–1714. https://doi.org/10.1007/s11947-010-0464-8.
(112) Shire, S. J.; Shahrokh, Z.; Liu, J. Challenges in the Development of High Protein Concentration Formulations. *J. Pharm. Sci.* **2004**, *93* (6), 1390–1402. https://doi.org/10.1002/jps.20079.
(113) Konermann, L.; Silva, E. A.; Sogbein, O. F. Electrochemically Induced PH Changes Resulting in Protein Unfolding in the Ion Source of an Electrospray Mass Spectrometer. *Anal. Chem.* **2001**, *73* (20), 4836–4844. https://doi.org/10.1021/ac010545r.
(114) Bockris, J.; Reddy, A. *Modern Electrochemistry*; Plenum Press: New York, 1970; Vol. 1.
(115) Lukacs, G. L.; Haggie, P.; Seksek, O.; Lechardeur, D.; Freedman, N.; Verkman, A. S. Size-Dependent DNA Mobility in Cytoplasm and Nucleus. *J. Biol. Chem.* **2000**, *275* (3), 1625–1629. https://doi.org/10.1074/jbc.275.3.1625.
(116) Panchuk-Voloshina, N.; Haugland, R. P.; Bishop-Stewart, J.; Bhalgat, M. K.; Millard, P. J.; Mao, F.; Leung, W. Y.; Haugland, R. P. Alexa Dyes, a Series of New Fluorescent Dyes That Yield Exceptionally Bright, Photostable Conjugates. *J. Histochem. Cytochem. Off. J. Histochem. Soc.* **1999**, *47* (9), 1179–1188. https://doi.org/10.1177/002215549904700910.
(117) Bender, A. T.; Borysiak, M. D.; Levenson, A. M.; Lillis, L.; Boyle, D. S.; Posner, J. D. Semiquantitative Nucleic Acid Test with Simultaneous Isotachophoretic Extraction and Amplification. *Anal. Chem.* **2018**, *90* (12), 7221–7229. https://doi.org/10.1021/acs.analchem.8b00185.
(118) Toma, C.; Lu, Y.; Higa, N.; Nakasone, N.; Chinen, I.; Baschkier, A.; Rivas, M.; Iwanaga, M. Multiplex PCR Assay for Identification of Human Diarrheagenic Escherichia Coli. *J. Clin. Microbiol.* **2003**, *41* (6), 2669–2671. https://doi.org/10.1128/JCM.41.6.2669-2671.2003.
(119) Jonas, D.; Speck, M.; Daschner, F. D.; Grundmann, H. Rapid PCR-Based Identification of Methicillin-Resistant Staphylococcus Aureus from Screening Swabs. *J. Clin. Microbiol.* **2002**, *40* (5), 1821–1823. https://doi.org/10.1128/JCM.40.5.1821-1823.2002.
(120) Spackman, E.; Senne, D. A.; Bulaga, L. L.; Myers, T. J.; Perdue, M. L.; Garber, L. P.; Lohman, K.; Daum, L. T.; Suarez, D. L. Development of Real-Time RT-PCR for the Detection of Avian Influenza Virus. *Avian Dis.* **2003**, *47* (s3), 1079–1082. https://doi.org/10.1637/0005-2086-47.s3.1079.
(121) Queipo-Ortuño, M. I.; Tena, F.; Colmenero, J. D.; Morata, P. Comparison of Seven Commercial DNA Extraction Kits for the Recovery of Brucella DNA from Spiked Human Serum Samples Using Real-Time PCR. *Eur. J. Clin. Microbiol. Infect. Dis.* **2008**, *27* (2), 109–114. https://doi.org/10.1007/s10096-007-0409-y.
(122) Bulterys, P. L.; Garamani, N.; Stevens, B.; Sahoo, M. K.; Huang, C.; Hogan, C. A.; Zehnder, J.; Pinsky, B. A. Comparison of a Laboratory-Developed Test Targeting the Envelope Gene with Three Nucleic Acid Amplification Tests for Detection of SARS-CoV-2. *J. Clin. Virol.* **2020**, *129*, 104427. https://doi.org/10.1016/j.jcv.2020.104427.

(123) Hur, K.-H.; Park, K.; Lim, Y.; Jeong, Y. S.; Sung, H.; Kim, M.-N. Evaluation of Four Commercial Kits for SARS-CoV-2 Real-Time Reverse-Transcription Polymerase Chain Reaction Approved by Emergency-Use-Authorization in Korea. *Front. Med.* **2020**, *7*, 521. https://doi.org/10.3389/fmed.2020.00521.
(124) Vanuytsel, K.; Mithal, A.; Giadone, R. M.; Yeung, A. K.; Matte, T. M.; Dowrey, T. W.; Werder, R. B.; Miller, G. J.; Miller, N. S.; Andry, C. D.; Murphy, G. J. Rapid Implementation of a SARS-CoV-2 Diagnostic Quantitative Real-Time PCR Test with Emergency Use Authorization at a Large Academic Safety Net Hospital. *Med* **2020**, *1* (1), 152-157.e3. https://doi.org/10.1016/j.medj.2020.05.001.
(125) Ravi, N.; Cortade, D. L.; Ng, E.; Wang, S. X. Diagnostics for SARS-CoV-2 Detection: A Comprehensive Review of the FDA-EUA COVID-19 Testing Landscape. *Biosens. Bioelectron.* **2020**, *165*, 112454. https://doi.org/10.1016/j.bios.2020.112454.
(126) Commissioner, O. of the. *Coronavirus (COVID-19) Update: FDA Authorizes First COVID-19 Test for Self-Testing at Home*. FDA. https://www.fda.gov/news-events/press-announcements/coronavirus-covid-19-update-fda-authorizes-first-covid-19-test-self-testing-home (accessed 2021-09-03).
(127) Heap, D. M.; Herrmann, M. G.; Wittwer, C. T. PCR Amplification Using Electrolytic Resistance for Heating and Temperature Monitoring. *BioTechniques* **2000**, *29* (5), 1006–1012. https://doi.org/10.2144/00295st01.
(128) Sastry, S. K.; Barach, J. T. Ohmic and Inductive Heating. *J. Food Sci.* **2000**, *65* (s8), 42–46. https://doi.org/10.1111/j.1750-3841.2000.tb00617.x.
(129) Bowser, M. CAPILLARY ELECTROPHORESIS | Overview. In *Encyclopedia of Analytical Science (Second Edition)*; Worsfold, P., Townshend, A., Poole, C., Eds.; Elsevier: Oxford, 2005; pp 334–343. https://doi.org/10.1016/B0-12-369397-7/00135-7.
(130) Kim, S.-S.; Kang, D.-H. Comparison of PH Effects on Ohmic Heating and Conventional Heating for Inactivation of Escherichia Coli O157:H7, Salmonella Enterica Serovar Typhimurium and Listeria Monocytogenes in Orange Juice. *LWT - Food Sci. Technol.* **2015**, *64* (2), 860–866. https://doi.org/10.1016/j.lwt.2015.06.056.
(131) Kates, B.; Ren, C. L. Study of Joule Heating Effects on Temperature Gradient in Diverging Microchannels for Isoelectric Focusing Applications. *ELECTROPHORESIS* **2006**, *27* (10), 1967–1976. https://doi.org/10.1002/elps.200500784.
(132) Komine, Y.; Inokuchi, H. Precise Mapping of the RnpB Gene Encoding the RNA Component of RNase P in Escherichia Coli K-12. *J. Bacteriol.* **1991**, *173* (5), 1813–1816. https://doi.org/10.1128/jb.173.5.1813-1816.1991.
(133) Scott, A. T.; Layne, T. R.; O'Connell, K. C.; Tanner, N. A.; Landers, J. P. Comparative Evaluation and Quantitative Analysis of Loop-Mediated Isothermal Amplification Indicators. *Anal. Chem.* **2020**, *92* (19), 13343–13353. https://doi.org/10.1021/acs.analchem.0c02666.
(134) Layne, T.; Jackson, K.; Scott, A.; Tanner, N. A.; Piland, A.; Haverstick, D. M.; Landers, J. P. Optimization of Novel Loop-Mediated Isothermal Amplification with Colorimetric Image Analysis for Forensic Body Fluid Identification. *J. Forensic Sci.* **2021**, *66* (3), 1033–1041. https://doi.org/10.1111/1556-4029.14682.

(135) *Frequency Response Analysis of Amplifiers and Filters*. Basic Electronics Tutorials. https://www.electronics-tutorials.ws/amplifier/frequency-response.html (accessed 2020-02-08).
(136) Ahmed, R.; Ali, N.; Khan, S. U.; Tlili, I. Numerical Simulations for Mixed Convective Hydromagnetic Peristaltic Flow in a Curved Channel with Joule Heating Features. *AIP Adv.* **2020**, *10* (7), 075303. https://doi.org/10.1063/5.0010964.
(137) Fischbach, J.; Xander, N. C.; Frohme, M.; Glökler, J. F. Shining a Light on LAMP Assays' A Comparison of LAMP Visualization Methods Including the Novel Use of Berberine. *BioTechniques* **2015**, *58* (4), 189–194. https://doi.org/10.2144/000114275.
(138) Daskou, M.; Tsakogiannis, D.; Dimitriou, T. G.; Amoutzias, G. D.; Mossialos, D.; Kottaridi, C.; Gartzonika, C.; Markoulatos, P. WarmStart Colorimetric LAMP for the Specific and Rapid Detection of HPV16 and HPV18 DNA. *J. Virol. Methods* **2019**, *270*, 87–94. https://doi.org/10.1016/j.jviromet.2019.04.023.
(139) Ou, C.-Y.; Kwok, S.; Mitchell, S. W.; Mack, D. H.; Sninsky, J. J.; Krebs, J. W.; Feorino, P.; Warfield, D.; Schochetman, G. DNA Amplification for Direct Detection of HIV-1 in DNA of Peripheral Blood Mononuclear Cells. *Science* **1988**, *239* (4837), 295–297. https://doi.org/10.1126/science.3336784.
(140) Nakanishi, H.; Kido, A.; Ohmori, T.; Takada, A.; Hara, M.; Adachi, N.; Saito, K. A Novel Method for the Identification of Saliva by Detecting Oral Streptococci Using PCR. *Forensic Sci. Int.* **2009**, *183* (1), 20–23. https://doi.org/10.1016/j.forsciint.2008.10.003.
(141) Martel, N.; Gomes, S. A.; Chemin, I.; Trépo, C.; Kay, A. Improved Rolling Circle Amplification (RCA) of Hepatitis B Virus (HBV) Relaxed-Circular Serum DNA (RC-DNA). *J. Virol. Methods* **2013**, *193* (2), 653–659. https://doi.org/10.1016/j.jviromet.2013.07.045.
(142) Davidson, J. L.; Wang, J.; Maruthamuthu, M. K.; Dextre, A.; Pascual-Garrigos, A.; Mohan, S.; Putikam, S. V. S.; Osman, F. O. I.; McChesney, D.; Seville, J.; Verma, M. S. A Paper-Based Colorimetric Molecular Test for SARS-CoV-2 in Saliva. *Biosens. Bioelectron. X* **2021**, *9*, 100076. https://doi.org/10.1016/j.biosx.2021.100076.
(143) Liu, M.; Zhao, Y.; Monshat, H.; Tang, Z.; Wu, Z.; Zhang, Q.; Lu, M. An IoT-Enabled Paper Sensor Platform for Real-Time Analysis of Isothermal Nucleic Acid Amplification Tests. *Biosens. Bioelectron.* **2020**, *169*, 112651. https://doi.org/10.1016/j.bios.2020.112651.
(144) Song, J.; Mauk, M. G.; Hackett, B. A.; Cherry, S.; Bau, H. H.; Liu, C. Instrument-Free Point-of-Care Molecular Detection of Zika Virus. *Anal. Chem.* **2016**, *88* (14), 7289–7294. https://doi.org/10.1021/acs.analchem.6b01632.
(145) Wang, C.-H.; Lien, K.-Y.; Wu, J.-J.; Lee, G.-B. A Magnetic Bead-Based Assay for the Rapid Detection of Methicillin-Resistant Staphylococcus Aureus by Using a Microfluidic System with Integrated Loop-Mediated Isothermal Amplification. *Lab. Chip* **2011**, *11* (8), 1521–1531. https://doi.org/10.1039/C0LC00430H.
(146) Sayad, A. A.; Ibrahim, F.; Uddin, S. M.; Pei, K. X.; Mohktar, M. S.; Madou, M.; Thong, K. L. A Microfluidic Lab-on-a-Disc Integrated Loop Mediated Isothermal

Amplification for Foodborne Pathogen Detection. *Sens. Actuators B Chem.* **2016**, *227*, 600–609. https://doi.org/10.1016/j.snb.2015.10.116.
(147) Erickson, D.; Sinton, D.; Li, D. Joule Heating and Heat Transfer in Poly(Dimethylsiloxane) Microfluidic Systems. *Lab. Chip* **2003**, *3* (3), 141–149. https://doi.org/10.1039/B306158B.
(148) Tang, G. Y.; Yan, D. G.; Yang, C.; Gong, H. Q.; Chai, C. J.; Lam, Y. C. Joule Heating and Its Effects on Electroosmotic Flow in Microfluidic Channels. *J. Phys. Conf. Ser.* **2006**, *34*, 925–930. https://doi.org/10.1088/1742-6596/34/1/153.
(149) Tang, G.; Yan, D.; Yang, C.; Gong, H.; Chai, J. C.; Lam, Y. C. Assessment of Joule Heating and Its Effects on Electroosmotic Flow and Electrophoretic Transport of Solutes in Microfluidic Channels. *ELECTROPHORESIS* **2006**, *27* (3), 628–639. https://doi.org/10.1002/elps.200500681.
(150) Lasseter, T. L.; Clare, B. H.; Abbott, N. L.; Hamers, R. J. Covalently Modified Silicon and Diamond Surfaces: Resistance to Nonspecific Protein Adsorption and Optimization for Biosensing. *J. Am. Chem. Soc.* **2004**, *126* (33), 10220–10221. https://doi.org/10.1021/ja047642x.
(151) Taylor, T. B.; Winn-Deen, E. S.; Picozza, E.; Woudenberg, T. M.; Albin, M. Optimization of the Performance of the Polymerase Chain Reaction in Silicon-Based Microstructures. *Nucleic Acids Res.* **1997**, *25* (15), 3164–3168. https://doi.org/10.1093/nar/25.15.3164.
(152) Hnasko, T. S.; Hnasko, R. M. The Western Blot. In *ELISA: Methods and Protocols*; Hnasko, R., Ed.; Methods in Molecular Biology; Springer: New York, NY, 2015; pp 87–96. https://doi.org/10.1007/978-1-4939-2742-5_9.
(153) Kodzius, R.; Xiao, K.; Wu, J.; Yi, X.; Gong, X.; Foulds, I. G.; Wen, W. Inhibitory Effect of Common Microfluidic Materials on PCR Outcome. *Sens. Actuators B Chem.* **2012**, *161* (1), 349–358. https://doi.org/10.1016/j.snb.2011.10.044.
(154) Seok, Y.; Joung, H.-A.; Byun, J.-Y.; Jeon, H.-S.; Shin, S. J.; Kim, S.; Shin, Y.-B.; Han, H. S.; Kim, M.-G. A Paper-Based Device for Performing Loop-Mediated Isothermal Amplification with Real-Time Simultaneous Detection of Multiple DNA Targets. *Theranostics* **2017**, *7* (8), 2220–2230. https://doi.org/10.7150/thno.18675.
(155) Wang, J.; Dextre, A.; Pascual-Garrigos, A.; Davidson, J. L.; Maruthamuthu, M. K.; McChesney, D.; Seville, J.; Verma, M. S. Fabrication of a Paper-Based Colorimetric Molecular Test for SARS-CoV-2. *MethodsX* **2021**, *8*, 101586. https://doi.org/10.1016/j.mex.2021.101586.
(156) Moghadam, B. Y.; Connelly, K. T.; Posner, J. D. Isotachophoretic Preconcenetration on Paper-Based Microfluidic Devices. *Anal. Chem.* **2014**, *86* (12), 5829–5837. https://doi.org/10.1021/ac500780w.
(157) Rosenfeld, T.; Bercovici, M. Amplification-Free Detection of DNA in a Paper-Based Microfluidic Device Using Electroosmotically Balanced Isotachophoresis. *Lab. Chip* **2018**, *18* (6), 861–868. https://doi.org/10.1039/C7LC01250K.
(158) Li, X.; Luo, L.; Crooks, R. M. Low-Voltage Paper Isotachophoresis Device for DNA Focusing. *Lab. Chip* **2015**, *15* (20), 4090–4098. https://doi.org/10.1039/c5lc00875a.

APPENDIX A

SUPPLEMENTARY INFORMATION TO SECTION 3

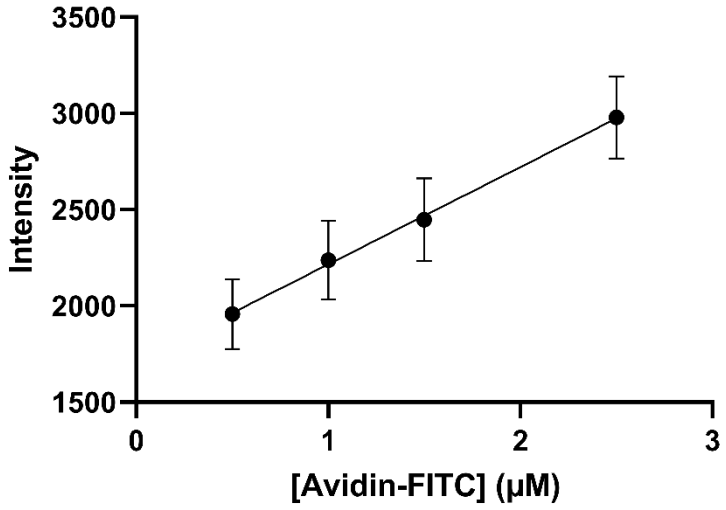

Figure A1 Calibration curve generated for avidin-FITC. Calibration equation: Intensity = 505.5*[Avidin-FITC] + 1710, R^2 = 0.9983.

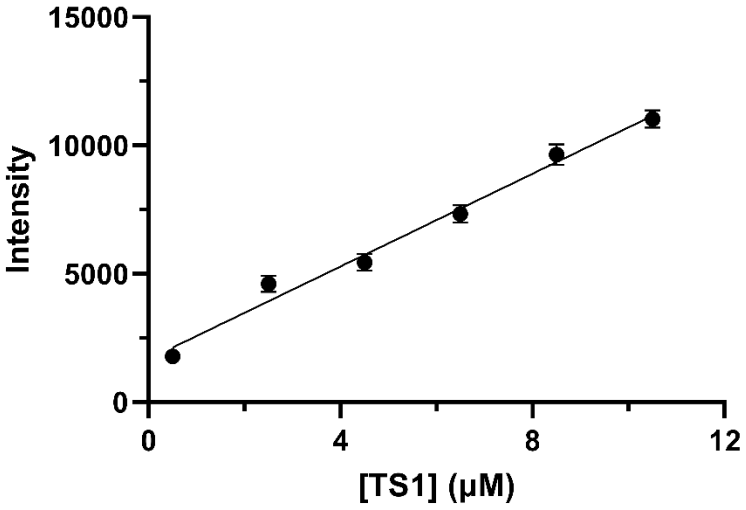

Figure A2 Calibration curve generated for Test Sequence 1 (TS1, 90 bp). Calibration equation: Intensity = 903.3*[TS1] + 1672, R^2 = 0.9862.

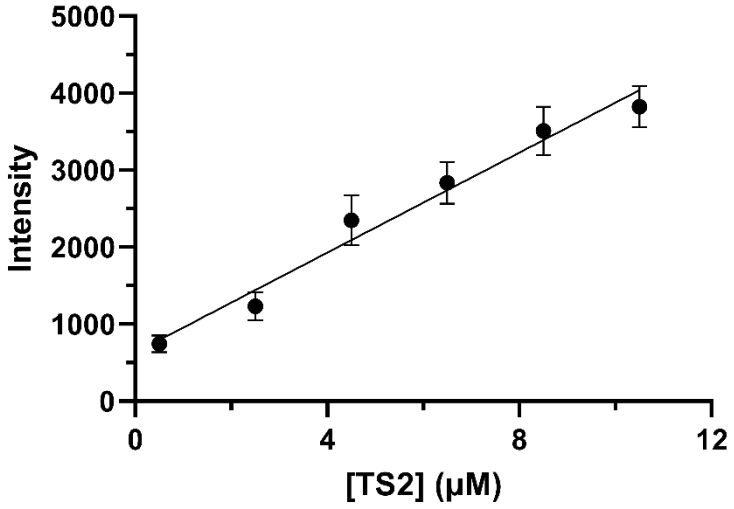

Figure A3 Calibration curve generated for Test Sequence 2 (TS2, 45 bp). Calibration equation: Intensity = 324.6*[TS2] + 630.3, R^2 = 0.9759